DEVELOPMENT OF MICROCOMPARTMENTALIZATION USING MACROMOLECULES AND LIQUID-LIQUID INTERFACES

by

Taisuke Kojima

A dissertation submitted in partial fulfillment
of the requirements for the degree of
Doctor of Philosophy
(Macromolecular Science and Engineering)
in The University of Michigan
2016

Doctoral Committee:
- Professor Shuichi Takayama, Chair
- Professor Joerg Lahann
- Professor Nicholas A. Kotov
- Professor Richard Robertson
- Associate Professor Anish Tuteja

To those who have taught me joy of life and science.

ACKNOWLEDGEMENTS

I would like to acknowledge my advisor, Professor Shuichi Takayama, for your patience and generosity to allow me to try whatever I have wanted through my Ph.D. course. Without your support, I could not survive as a researcher as well as a foreign graduate student in a place where I have never experienced and imagined before.

I would like to appreciate the rest of the committee members, Dr. Joerg Lahann, Dr. Nicholas A. Kotov, Dr. Richard Robertson, Dr. Anish Tuteja, for your suggestions and inputs. Each project described herein could not be completed without you.

I would like to thank former and current members of Takayama lab. Especially, I would like to mention Arlyne Simon and Priyan Weerappuli who have continuously supported my Ph.D. life. You are my best friends ever.

I would like to recognize my Swedish collaborators: Dr. Jonas Tegenfeldt who supported my research internship in Lund and Dr. Per-Åke Albertsson who shared your research history as the living god of ATPSs. It was my dream to conduct research in Sweden since I worked with Sweden-originated biosensors in my bachelor and master degree.

I would like to give my deep appreciation to Lili Tang, Li-ting Chang, Tomoko Savina, and Mayurachat Ning Gulari. I cannot thank enough to you all for your sincere support as spiritual moms.

I would like to express my sincere gratitude to my parents, Masako and Iwao Kojima. Your dedication to me is incredible. With your love, I can survive wherever I go.

I would like to sincerely appreciate my dear, Marisa Chandavimol, who dared to come all the way to cold Michigan and supported me through your dedication.

Finally, I would like to express my deep love to the wild animals in Michigan, especially deer, geese, gophers, skanks, squirrels, and turkeys around the campus. Over three generations, they could heel my bitter feelings whenever I get depressed. Without them, I could not survive in Michigan winter over 4 years.

Table of Contents

Dedication ii

Acknowledgements iii

List of Figures ix

List of Schemes xii

Abstract xiii

Chapters

1. **Introduction: Construction of micro-scale chemical and biological assay platforms through microfabrication and microcompartmentalization** 1
    - 1.1. The Miniaturization of The Reactors 1
    - 1.2. PDMS-Templated Surface Modification: Top-Down Approach to Microreactors 2
    - 1.3. Microcompartmentalizaiton *via* Self-Assembly: Bottom-Up Approach to Microbioreactors 4
    - 1.4. Liquid-in-Liquid Separation in Aqueous Two-Phase Systems and Complex Coacervation 5

1.5. Microcompartmentalizaiton at The Liquid-Liquid Interfaces by Combined Top-Down and Bottom-Up Techniques.....7

1.6. Dissertation Overview.....9

1.7. References.....10

2. **Patchy Surfaces Stabilize Dextran-Polyethylene Glycol Aqueous Two-Phase System Liquid Patterns**.....14

2.1. Introduction.....15

2.2. Materials and Methods.....16

2.3. Results and Discussion.....20

2.4. Conclusions.....25

2.5. References.....44

3. **Surface-Templated Hydrogel Patterns Prompt Matrix-Dependent Migration of Breast Cancer Cells towards Chemokine-Secreting Cells**.....47

3.1. Introduction.....48

3.2. Materials and Methods.....50

3.3. Results.....55

3.4. Discussion.....61

3.5. Conclusions.....64

3.6. References 77

4. **Microscale Determination of Aqueous Two Phase System Binodals by Droplet Dehydration in Oil** 82

4.1. Introduction 83

4.2. Materials and Methods 85

4.3. Results and Discussion 88

4.4. Conclusions 90

4.5. References 108

5. **Shrinking Microdroplets Assists Metamorphoses of The Nanoparticle Assemblies** 110

5.1. Introduction 111

5.2. Materials and Methods 112

5.3. Results and Discussion 117

5.4. Conclusions 122

5.5. References 139

6. **Spatio-temporally Regulated Enzyme Reactions in Membrane-Free Compartments Formed in An Aqueous Three Phase System** 142

6.1. Introduction 144

6.2. Materials and Methods 145

6.3. Results and Discussion 150

6.4. Conclusions 156

6.5. References 168

7. Conclusions and Future Directions 171

7.1. Conclusions 171

7.2. Future Directions 176

List of Figures

Figure 2.1. Fluorescent Measurement of Chemically Modified PDMS Surfaces....................30
Figure 2.2. XPS Analyses of Chemically Modified PDMS Surfaces 31
Figure 2.3. Contact Angle Measurements of Surfaces at Water-Air Interface 32
Figure 2.4. Contact Angle Measurements of Surfaces at DEX-PEG Interface........................33
Figure 2.5. Sliding and Hysteresis Measurements of Surfaces at DEX-PEG Interface...........34
Figure 2.6. DEX Solution “M” Patterns in 3.2% DEX – 2.5% PEG System 35
Figure 2.7. DEX Solution Lines Formed on Surface-Modified Square Patches......................36
Figure 2.8. Arbitrary DEX Solution Patterns in 3.2% DEX – 2.5% PEG System..................37
Figure 2.9. Fluorescent Measurement of Chemically Deactivated PDMS Surfaces 38
Figure 2.10. Contact Angle Measurements: Young’s Equation..39
Figure 2.11. DEX Solution “U” Patterns in 3.2% DEX – 2.5% PEG System 40
Figure 2.12. Patchy Surface Designs..41
Figure 2.13. Surface Adhesion and Gap Effects on DEX Solution Line Stability.....................42
Figure 2.14. Pinning and Spreading of Arbitrary DEX Solution Patterns 43
Figure 3.1. Patterning of Hydrogels on A Cell-Repellent Surface...65
Figure 3.2. Surface Characterization of PAA-Coated PDMS 66
Figure 3.3. Migration Assay of CXCR4+ Cells in 3D Gel Matrix 67
Figure 3.4. Computational Modeling of CXCL12-β Gradients 68
Figure 3.5. Binding Assay of CXCL12 Isoforms in Different Gel Matrices 69
Figure 3.6. Migratory Comparison of CXCL12 Isoforms in The Presence of Matrigel..........70
Figure 3.7. HBME Cells in The Patterned Hydrogel Droplets 71
Figure 3.8. Surface Topography of Intact and Oxidized PAA-Coated PDMS 72

Figure 3.9. Soluble Factors to Inhibit Migration in The Patterned Hydrogel System 73
Figure 3.10. Migration Assay of CXCR4-CXCL12 with Large Spacing 74
Figure 3.11. Varied Simulation Parameters for The CXCL12 Diffusion Profiles 75
Figure 3.12. Multiplex Gel Patterning in Air 76
Figure 4.1. Shapes of Droplets of PBS Solution in Soybean Oil 94
Figure 4.2. Time-Lapse Droplet Shrinking of a PBS Soltuion 95
Figure 4.3. Phase Separation at The Binodal Point of 10K DEX – 8K PEG System 96
Figure 4.4. Binodal Points in DEX-PEG System Determined by Dehydration 97
Figure 4.5. Binodal Points in DEX-PVA System and PEG-PVA System 98
Figure 4.6. Binodal Points in BSA-PEG System 99
Figure 4.7. Binodal Points in DEX-PEG System Determined by Dilution...........................100
Figure 4.8. Time-Lapse Droplet Images in 10K DEX – 8K PEG System 101
Figure 4.9. The Uncertainty of Binodal Points in 10K DEX – 8K PEG System 102
Figure 4.10. Binodal Points for a 500K DEX – 35K PEG System 103
Figure 4.11. Fitted Binodal Curves in DEX-PVA System and PEG-PVA System 104
Figure 4.12. Fitted Binodal Curves in BSA-PEG System 105
Figure 4.13. Magnified Phase Contrast Images of Droplets Before and At Binodal Point 106
Figure 4.14. Phase Separation at Binodal Point in 66K BSA – 35K PEG System 107
Figure 5.1. Time-Lapse Droplet Shrinking of CdTe Suspension..124
Figure 5.2. SEM Images of CdTe Assemblies 125
Figure 5.3. AFM Images of The CdTe Assemblies Collected at Day-3 126
Figure 5.4. TEM Images of The CdTe Assemblies Collected at Day-3 127
Figure 5.5. EDX Images of The CdTe Assemblies Collected at Day-3...............................128
Figure 5.6. Confocal Microscopy Images of The CdTe Assemblies Collected at Day-3 129
Figure 5.7. SEM Images of CdTe Assemblies at Day3 with The Oil Constituents 130
Figure 5.8. SEM Images of CdTe Assemblies in The Presence of Salt and Light................131
Figure 5.9. SEM Images of The CdTe Assemblies by the 100-Fold High Concentration.....132

Figure 5.10. EDX Spectra of The CdTe Assemblies Collected at Day-3 133
Figure 5.11. Fluorescent Spectra of The CdTe Assemblies Collected at Day-3......................134
Figure 5.12. A Computation Model of Droplet Dehydation in Soybean Oil 135
Figure 5.13. A Computation Model of Droplet Dehydation in Hexadecane 136
Figure 5.14. SEM Images of The NPs Droplets Irradiated at Different Time Points 137
Figure 5.15. Reconfigured 3D Z-Stack Images of The CdTe Droplets 138
Figure 6.1. Patterning of ATP-PDDA Coacervates in 10%DEX – 10% PEG System 158
Figure 6.2. Ionic Strength-Driven Degradation of ATP-PDDA Coacervates........................159
Figure 6.3. GOx-HRP-Mediated Cascade Reaction...160
Figure 6.4. Cascade Reaction Behavior Upon Droplet Isolation and Coalescence 161
Figure 6.5. Dextranase-Mediated DEX Degradation Assay 162
Figure 6.6. UV/VIS Spectra of ATP-PDDA Coacertvate Suspension..................................163
Figure 6.7. Wetting Behavior of ATP-PDDA Coacervates 164
Figure 6.8. Multi-Patterning of ATP-PDDA Coacervates Containing Food Colorings 165
Figure 6.9. pH and Ionic Strength Effect on ATP-PDDA Coacervates 166
Figure 6.10. Time-lapse GOx Partitioning into ATP-PDDA Coacervates 167

List of Schemes

Scheme 2.1. Chemical Modification of PDMS 27

Scheme 2.2. Two-Face Chemical Modification of PDMS 28

Scheme 2.3. Microchannel-Guided Surface Modification of PDMS 29

Scheme 4.1. Determination of ATPS Binodal Curves by Dilution and Concentration....................92

Scheme 4.2. Droplet Shrinking in Oil on A Dish Surface and FC40 Oil Surface....................93

ABSTRACT

Development of Microcompartmentalization Using Macromolecules and Liquid-Liquid Interfaces

by

Taisuke Kojima

Compartmentalization combined with regulated exchange and release of biomaterials is the key biological function. At the subcellular level, organelles sequester enzymes and substrates for storage while processing and releasing on demand. At the organism level, appropriate cellular compartmentalization gives rise to tissue organization and higher order function. Man-made bioreaction compartmentalization typically relies on micro-reactors constructed with glass, silicon, hard plastic, or amiphiphilic molecular walls. Reactors with such physical barriers, in return for excellent compartmentalization, lack amenability to molecular and cellular release and exchange as seen in the body. This thesis describes the engineering of multi-compartment bioreactors that utilize stable reagent partitioning within immiscible aqueous solutions. The all aqueous compartmentalization scheme, when combined with a micropatterned surface that pins the liquid-liquid interfaces, enable versatile direct printing of arbitrary multi-compartment bioreactor networks. Additionally, the lack of physical barriers at the liquid-liquid interface between the different aqueous compartments allows use of phase-altering chemicals to trigger rapid and selective mixing of materials between compartments in ways not possible with conventional miroreactors. Specific examples demonstrated include a compartmentalized cascade reaction that utilizes glucose and oxygen as nutrients to catalzye the production of different colored dyes within microcompartments and the localization-enhanced degradation of the microcompartments with a polysaccharide-degrading enzyme. In a separate strategy, a shrinking microreactor platform was created using oil dehydration. These shrinking bioreactors were utilized for micro-scale ATPS phase diagram determination and also adopted for micro-scale self-assembly of CdTe nanoparticles. Finally, surface-templated hydrogel micropatterning was used to compartmentalize cancer cells as well as limit diffusion of chemoattractants. This platform revealed the importance of extracellular matrix-mediated capture and localization of chemoattractants in triggering cancer cell migration that lead to a breakdown of cellular compartmentalization, tissue dis-organization and cancer metastasis. In addition to the specific demonstrations and biological insights obtained, the described macromolecular phase-separation microreactor platforms are versatile in configuration possibilities, particularly when combined with microfabrication technologies, and amenable to further explore materials science and biomedical engineering applications.

Chapter 1

Introduction: Construction of micro-scale chemical and biological assay platforms through microfabrication and microcompartmentalization

1.1 The miniaturization of the reactors

The scale of reactions determines the amount of products and the cost of materials and processes. It is important to determine the reaction scale based on needs. At the industrial level, batch reactors and continuous reactors are exploited to mass produce chemicals for commercial purposes[1] in which the type of the reactors is carefully selected based on the thermodynamics and kinetics of the chemical reactions involved.[2] At the laboratory level, smaller scale reactors such as flasks are commonly used to perform chemical reactions for research purposes. However, when one has to challenge chemical or biological questions with small quantity of materials, the reactor scale must be further miniaturized.

Meanwhile it is often challenging to build up scalable reaction platforms because reaction conditions vary depending on the scale of the reactor.[3] Owing to the development of microtechnologies associated with microelectromechanical systems (MEMS)[4], microscale reactors (microreactors) made of rigid materials such as silicon, quartz, metals, polymers, ceramics, and glass have also become available.[5, 6] Despite their size, microreactors can be highly scaled through repeating unit processes and numbering-up multiple microreactors in parallel. Importantly, this type of scale up can be performed without further optimization of reaction conditions.[7-9] Interestingly, when the reactor size becomes smaller than a millimeter, emergent properties arise: for example, rapid heat exchange and diffusion-based mixing.[10, 11] These properties enable fast and efficient synthesis, process, separation, analysis, and detection, and lead to the rapid development of micro total analysis systems (μTAS).[12-14] The associated technologies often overlap with the field of biomedical MEMS (Bio-MEMS) and lab-on-a-chip (LOC).[15]

Microreactors can perform biological reactions as well as chemical reactions that require only small quantities of reagents compared to their larger counterparts.[16] The microreactor platform is especially appealing to the pharmaceutical and biomedical industries where the reduction in time and cost for fast evaluation and implementation of new production protocols is critical.[17] Since biological reactions are usually performed under mild conditions, soft materials such as polymers, gels, organic compounds have commonly been adopted in the microfabrication (soft lithography) of microreactors because of easy-handling, low cost, and biocompatibility.[18] Among such soft materials, polydimethylsiloxane (PDMS) has been most widely used.[19] Since PDMS is transparent, gas permeable, and, biocompatible, PDMS platform makes it convenient to perform biological assays that use microscopes.[20] Since some of the works presented in this thesis also utilizes PDMS as a means of microreactor construction, PDMS-based microfabrication processes are described in the next section.

1.2 PDMS-templated surface modification: top-down approach to microreactors

PDMS-based soft lithography creates embossed or bas-relief microstructures by means of mold, stamp, and mask.[21] Briefly, the master can be made as follows. SU-8, a negative photoresist polymer is spin coated on a Si wafer and is polymerized through UV exposure with a photo mask containing designed patterns. The unexposed SU-8 resist is developed and the designed microstructures are left behind on the wafer surface. PDMS masks with the inverse micropatterns are replicated from the master for the subsequent procedures. PDMS molds can create microchannels when bound to another substrate. A flow system using the microchannels (also known as microfluidics) is the most common platform among PDMS-based microreactors. PDMS stamps can transfer materials to a substrate with the specific geometry that can be utilized to study effects of the surface geometry upon cell proliferation.[22]

In this thesis, PDMS masks are exploited for surface modification of substrates where the detailed protocols are described in the related chapters. Surface modification can introduce surface energy heterogeneity, wet the specific geometries and locations, and thereby provide surface scaffolds to construct the reactor arrays.[23] In fact, surface modification has been exploited to pattern milli-to-femto liter solutions to run high-throughput biological assays on various surfaces.[24] In general, there are two types of surface modification: chemical and physical.[25] Chemical modification involves surface oxidation by plasma oxidation, gamma / UV irradiation in order to alter wettability of defined surface regions. Physical modification introduces surface microstructures such as micropillars and microwells in order to sustain aqueous solutions.

PDMS-based soft lithography enables both chemical and physical modifications for biological assays on a PDMS-coated surface.[26] PDMS-based microreactors provide a versatile opportunity to explore and interrogate biological processes and a few examples are demonstrated in this thesis. This approach, which is referred to as a "top-down" approach, is one where microreactors are produces by scaling down large scale reaction platforms. This approach is presented, furthermore, in contrast to the "bottom-up" approach, where microreactors are constructed by the assembly of small-scale parts such as molecules.

1.3 Microcompartmentalization *via* self-assembly: bottom-up approach to microbioreactors

The top-down microfabrication relies on light- and machine-assisted technology where the fabrication scale is diffraction-limited and instrumental precision-dependent. On the other hand, bottom-up technologies can build up microreactors from the molecular level *via* self-assembly. Self-assembly is a spontaneous phenomenon where the molecular balance between attraction and repulsion dictates the resulting process.[27] Self-assembly can be categorized into four types[28]: static, dynamic, templated, and biological. This work handles mainly static self-assembly where the system at global and local equilibrium dissipates no energy. Such examples are amphiphilic vesicle assembly, protein assembly, and colloidal particle assembly. Among biological systems, the eukaryotic cells (diameter: 10 - 100 μm), embody various biomolecules in their micro-scale compartments (diameter: 1 - 10 μm) such as nucleus and organelles.[29] The cells use such self-assembled microcompartments to control spatiotemporal metabolic and replicating processes where the compartmentalized substances are processed at the desired timing and location. Hence the cells can be considered as multi-functional microreactors.

The superstructures formed *via* molecular self-assembly can serve as cell-mimetic reactors that perform chemical and biological reactions.[30] Those reactors can be categorized into two types: membrane-bound[31] or membrane-free[32] constructs. Membrane-bound architectures such as liposome[33] and polymersome[34] have water-filled lumen segregated by a semipermeable barrier and separate inside from outside. They have structural similarity with the living cells made of lipid bilayer membranes that enable selective flux of substances. Although the physically closed microenvironment enables long term encapsulation of substances, it often requires chemical gradient formation or membrane transporter to incorporate energy and materials into their structures.[35] In contrast, membrane-free constructs such as water-oil system[36] are more primitive and flexible for energy and materials uptake. Recently, aqueous two-phase systems and complex coacervation in water-water systems[37] have been demonstrated as emerging membrane-free constructs and discovered in the living cell compartments.[38] Those systems are described in the next section.

1.4 Liquid-in-liquid separation in aqueous two-phase systems and complex coacervation

An aqueous two-phase system (ATPS) comprises two different polymers, a polymer and a kosmotropic salt, or a chaotropic salt and a kosmotropic salt in solution, and phase separates when those constituents are mixed at appropriate concentrations at a particular temperature.[39] Although those constituents are hydrophilic in general, a slight difference in hydrophobicity among them becomes prominent at sufficiently high concentrations and, consequently, causes liquid-liquid phase separation where the individual phases are enriched with one of the two components. This phenomenon was first discovered by Martius Beijerinck in 1896 when he observed immiscibility of aqueous solutions of agar against starch and gelatin.[40] A field of ATPS research was expanded to a separation technique by Per-Åke Albertsson in 1956.[41]

Meanwhile, there is another liquid-liquid phase separation when oppositely charged polyelectrolytes at sufficiently high concentrations form polyion complex in solution.[42] Similar to ATPSs, the two-phase comprises polyion complex-rich and -depleted phases. This phenomenon is referred to as complex coacervation. Coacervation iteself was first proposed by H.G. Bungenberg de Jong[43] in 1929 while it was widely propagated by Alexander Oparin and J.B.S. Haldane[44] in 1936. Although the underlying mechanisms of phase formation are different between ATPSs and complex coacervation, given the resulting liquid-liquid phase separation, this thesis considers complex coaervation as a part of ATPSs.

Theoretical approaches to understand the underlying mechanisms of neutral polymer ATPSs have been developed using theoretical[45] and computational[46] models where enthalpic and entropic contributions of each component in the systems are considered. However, they are not sufficiently precise to predict phase diagrams of the systems without empirical data. Hence empirical approaches are often required to determine critical concentrations based on the various parameters: polymer molecular weights, salt concentrations, temperature, and pH. Specifically in ATPSs, the resulting phase diagram is a binodal curve, which delineates the concentrations of each polymer /salt in solution and determines the formation of a single or two-phase system.

ATPSs have two unique characteristics: low interfacial tension and molecular partitioning.[47] First, interfacial tension of the systems is in the range of 1 - 50 μN/m, 1000 - 10000 magnitude lower than that of air-water or oil-water systems (10 - 70 mN/m). The low interfacial tension is especially beneficial for preservation of active biological materials because the high interfacial tension at air-water or oil-water interfaces can denature their native structures and lose their functions. Second, molecules present in those systems can selectively be partitioned into one phase over the other phase based on the following properties: molecular composition, molecular weight, size, surface charge, hydrophobicity, chirality, etc. The molecular partitioning can be tailored by those physicochemical properties of the phase components.

Based on the above two characteristics, ATPSs have been utilized for separation and purification of biological materials. Researchers have shown various biomolecular separation (recovery) from a mixture of contaminants.[48] Although ATPS-based separation techniques have been developed since 1970s, other separation technologies have advanced and competed with the ATPS-based techniques, which offsets relative advantages of ATPS-separation. However, recently, new biomedical applications using ATPSs have been explored and demonstrated. For example, ATPSs enable site-specific reagent delivery on patterned cells[49], crosstalk-free multiplex enzyme-linked immuno sorbent assay[50, 51], rapid preparation of cell membrane sheets[52] while complex coacervation grants the direct delivery of reagents to single cells[53] and micro-scale organ development[54]. Since ATPS separation techniques often deal with laboratory scale sample volume, it is desired to miniaturize the experimental systems for practical and economical purposes. The miniaturized ATPS-based platforms would have great potential for biomedical applications.

1.5 Microcompartmentalization at the liquid-liquid interfaces by combined top-down and bottom-up techniques.

While the number of publication using PDMS-based bioassay platforms in engineering field, the number of publication using the platforms in biological field have been significantly low and stagnant.[55] One of the reasons is that the fabrication and operation of the platforms involves expensive and tedious processes. A simple yet versatile platform to interrogate biological questions that conventional systems fail to address is in great demand.

PDMS-based soft lithography together with liquid-liquid systems has the potentials to create unique reaction platforms that are not simple scale-down of bulk reaction systems. Fore example, surface-patterned microreactors may suffer denaturation of biological molecules and evaporation of solvents at an air-liquid interface. Those drawbacks may lead to inaccurate and misleading outputs from the biological reactions. One potential synergy is that the designed geometries on PDMS surface fabricated by soft lithography can provide micro-scale scaffolds at the liquid-liquid interfaces.

As is the case with chemical reactions, the conventional microreactors may also lack the flexibility and require laborious fabrication and deep expertise. If microreactors are succinctly constructed at liquid-liquid interfaces, it can circumvent such drawbacks and provide robust and unique platforms for biological assays. The microreactors at the liquid-liquid interfaces enable rapid and selective mass exchange and diffusion with small quantity of reagents, provide robust and reliable reaction platforms, and open new doors to explore functional material processes and biological assays that conventional approaches fail to achieve. In this thesis, combined top-down and bottom-up microcompartmentalization is explored and implemented in order to create novel microreactors at liquid-liquid interfaces with easy operation. This thesis sheds light on the ATPS-based biomedical applications and provides platforms to the interdisciplinary fields such as chemistry, material science, and biology.

1.6 Dissertation Overview

This work is divided into seven individual chapters where unique microcompartmentalization at liquid-liquid interfaces is demonstrated by combined top-down and bottom-up technologies. Chapter 2 describes surface micropatterning of ATPSs on chemically modified-PDMS surfaces and underlying principles of liquid-in-liquid patterning. Chapter 3 demonstrates autonomous chemogradients formation and resulting cancer cell migration using a gel-in-gel micropatterning technique. Chapter 4 develops a shrinking microreactor platform using oil dehydration for ATPS binodal determination and Chapter 5 exploits the technology for unique self-assembly of CdTe nanoparticles. Chapter 6 establishes a hybrid system of an ATPS and complex coacervation for membrane-free microreactors and performs bioreactions. Chapter 7 summarizes the work presented in this thesis and provides future direction of the research.

1.7 References

1. Froment, G. F.; Bischoff, K. B.; De Wilde, J., *Chemical Reactor Analysis and Design*. Wiley New York: 1990.

2. Hill, C. G.; Root, T. W., *Introduction to Chemical Engineering Kinetics and Reactor Design*. John Wiley & Sons: 2014.

3. Laird, T., Industrial Process Scale-Up. *Org. Process Res. Dev.* **2014,** *18*, 560-560.

4. Moreau, W. M., *Semiconductor Lithography: Principals and Materials*. Plenum Press: 1988.

5. Watts, P.; Wiles, C., Recent Advances in Synthetic Micro Reaction Technology. *Chem. Commun.* **2007**, 443-467.

6. Ehrfeld, W.; Hessel, V.; Haverkamp, V., *Microreactors*. Wiley Online Library: 2000.

7. Roberge, D. M.; Gottsponer, M.; Eyholzer, M.; Kockmann, N., Industrial Design, Scale-up, and Use of Microreactors. *Chim. Oggi. - Chem. Today* **2009,** *7*, 8-11.

8. Petschacher, C.; Eitzlmayr, A.; Besenhard, M.; Wagner, J.; Barthelmes, J.; Bernkop-Schnürch, A.; Khinast, J. G.; Zimmer, A., Thinking Continuously: A Microreactor for The Production and Scale-Up of Biodegradable, Self-Assembled Nanoparticles. *Polym. Chem.* **2013,** *4*, 2342-2352.

9. Kockmann, N.; Gottsponer, M.; Roberge, D. M., Scale-up Concept of Single-Channel Microreactors from Process Development to Industrial Production. *Chem. Eng. J.* **2011,** *167*, 718-726.

10. Burns, J.; Ramshaw, C., Development of a microreactor for chemical production. *Chem. Eng. Res. Des.* **1999,** *77*, 206-211.

11. Squires, T. M.; Quake, S. R., Microfluidics: Fluid Physics at The Nanoliter Scale. *Rev. Mod. Phys.* **2005,** *77*, 977.

12. Reyes, D. R.; Iossifidis, D.; Auroux, P.-A.; Manz, A., Micro Total Analysis Systems. 1. Introduction, Theory, and Technology. *Anal. Chem.* **2002,** *74*, 2623-2636.

13. Auroux, P.-A.; Iossifidis, D.; Reyes, D. R.; Manz, A., Micro Total Analysis Systems. 2. Analytical Standard Operations and Applications. *Anal. Chem.* **2002,** *74*, 2637-2652.

14. Arora, A.; Simone, G.; Salieb-Beugelaar, G. B.; Kim, J. T.; Manz, A., Latest Developments in Micro Total Analysis Systems. *Anal. Chem.* **2010,** *82*, 4830-4847.

15. Saliterman, S., *Fundamentals of BioMEMS and Medical Microdevices*. SPIE Press: 2006; Vol. 153.

16. Šalić, A.; Tušek, A.; Zelić, B., Application of Microreactors in Medicine and Biomedicine. *J. Appl. Biomed.* **2012,** *10*, 137-153.

17. Watts, P., Microreactors for Drug Discovery: The Importance of Integrating Chemical Synthesis with Real-Time Analytical Detection. *Anal. Bioanal. Chem.* **2005,** *382*, 865-867.

18. Xia, Y.; Whitesides, G. M., Soft Lithography. *Annu. Rev. Mater. Sci.* **1998,** *28*, 153-184.

19. McDonald, J. C.; Whitesides, G. M., Poly (dimethylsiloxane) as A Material for Fabricating Microfluidic Devices. *Acc. Chem. Res.* **2002,** *35*, 491-499.

20. Qin, D.; Xia, Y.; Rogers, J. A.; Jackman, R. J.; Zhao, X.-M.; Whitesides, G. M., Microsystem Technology in Chemistry and Life Science. *Top. Curr. Chem.* **1998,** *194*, 1-20.

21. Weibel, D. B.; DiLuzio, W. R.; Whitesides, G. M., Microfabrication Meets Microbiology. *Nat. Rev. Microbiol.* **2007,** *5*, 209-218.

22. Chen, C. S.; Mrksich, M.; Huang, S.; Whitesides, G. M.; Ingber, D. E., Geometric Control of Cell Life and Death. *Science* **1997,** *276*, 1425-1428.

23. Ueda, E.; Levkin, P. A., Emerging Applications of Superhydrophilic ‐ Superhydrophobic Micropatterns. *Adv. Mater.* **2013,** *25*, 1234-1247.

24. Chiu, D. T.; Lorenz, R. M., Chemistry and Biology in Femtoliter and Picoliter Volume Droplets. *Acc. Chem. Res.* **2009,** *42*, 649-658.

25. Adamson, A. W.; Gast, A. P., *Physical Chemistry of Surfaces*. 6th ed.; John Wiley & Sons, Inc.: 1997.

26. Whitesides, G. M.; Ostuni, E.; Takayama, S.; Jiang, X.; Ingber, D. E., Soft Lithography in Biology and Biochemistry. *Annu. Rev. Biomed. Eng.* **2001,** *3*, 335-373.

27. Whitesides, G. M.; Boncheva, M., Beyond Molecules: Self-assembly of Mesoscopic and Macroscopic Components. *Proc. Natl. Acad. Sci.* **2002,** *99*, 4769-4774.

28. Whitesides, G. M.; Grzybowski, B., Self-Assembly at All Scales. *Science* **2002,** *295*, 2418-2421.

29. Phillips, R.; Kondev, J.; Theriot, J.; Garcia, H., *Physical Biology of The Cell*. 2nd ed.; Garland Science: 2012.

30. Walde, P.; Umakoshi, H.; Stano, P.; Mavelli, F., Emergent Properties Arising from The Assembly of Amphiphiles. Artificial Vesicle Membranes as Reaction Promoters and Regulators. *Chem. Commun.* **2014,** *50*, 10177-10197.

31. Karlsson, M.; Davidson, M.; Karlsson, R.; Karlsson, A.; Bergenholtz, J.; Konkoli, Z.; Jesorka, A.; Lobovkina, T.; Hurtig, J.; Voinova, M., Biomimetic Nanoscale Reactors and Networks. *Annu. Rev. Phys. Chem.* **2004,** *55*, 613-649.

32. Li, M.; Huang, X.; Tang, T. D.; Mann, S., Synthetic Cellularity Based on Non-Lipid Micro-Compartments and Protocell Models. *Curr. Opin. Chem. Biol.* **2014,** *22*, 1-11.

33. Luisi, P. L.; Walde, P.; Oberholzer, T., Lipid Vesicles as Possible Intermediates in The Origin of Life. *Curr. Opin. Colloid Interface Sci.* **1999,** *4*, 33-39.

34. Kamat, N. P.; Katz, J. S.; Hammer, D. A., Engineering Polymersome Protocells. *J. Phys. Chem. Lett.* **2011,** *2*, 1612-1623.

35. Deamer, D. W.; Dworkin, J. P., Chemistry and Physics of Primitive Membranes. *Top. Curr. Chem.* **2005,** *259*, 1-27.

36. Yamada, A.; Barbaud, F.; Cinque, L.; Wang, L.; Zeng, Q.; Chen, Y.; Baigl, D., Oil Microsealing: A Robust Micro‐compartmentalization Method for On‐Chip Chemical and Biological Assays. *Small* **2010,** *6*, 2169-2175.

37. Aumiller Jr, W. M.; Davis, B. W.; Keating, C. D., Phase Separation as A possible Means of Nuclear Compartmentalization. *Int. Rev. Cell. Mol. Biol.* **2013**, 109-149.

38. Brangwynne, C. P., Phase Transitions and Size Scaling of Membrane-Less Organelles. *J. Cell. Biol.* **2013,** *203*, 875-881.

39. Albertsson, P.-Å., *Partition of Cell Particles and Macromolecules*. 3rd ed.; Wiley New York: 1986.

40. Beijerinck, M., Parasiten und Infektionskrankenheiten *Zentralbl. Bakteriol.* **1896,** *2*, 697-699.

41. Albertsson, P.-Å., Chromatography and Partition of Cells and Cell Fragments. *Nature* **1956,** *177*, 771-774.

42. Van der Gucht, J.; Spruijt, E.; Lemmers, M.; Stuart, M. A. C., Polyelectrolyte Complexes: Bulk Phases and Colloidal Systems. *J. Colloid Interface Sci.* **2011,** *361*, 407-422.

43. Bungenberg de Jong, H.; Kruyt, H., Coacervation (Partial Miscibility in Colloid Systems). *Proc. Sect. Sci. Kon. Akad. Wetensch. Amsterdam.* **1929,** *32*, 849-856.

44. Lazcano, A., Historical Development of Origins Research. *Cold Spring Harb. Perspect. Biol.* **2010,** *2*, a002089.

45. Cabezas, H., Theory of Phase Formation in Aqueous Two-Phase Systems. *J Chromatogr. B Biomed. Sci. Appl.* **1996,** *680*, 3-30.

46. Burgess, D., Practical Analysis of Complex Coacervate Systems. *J. Colloid Interface Sci.* **1990,** *140*, 227-238.

47. Hatti-Kaul, R., *Aqueous Two-Phase Systems: Methods and Protocols*. Humana Press: 2000.

48. Raja, S.; Murty, V. R.; Thivaharan, V.; Rajasekar, V.; Ramesh, V., Aqueous Two Phase Systems for The Recovery of Biomolecules–A Review. *Sci. Technol.* **2011,** *1*, 7-16.

49. Tavana, H.; Jovic, A.; Mosadegh, B.; Lee, Q.; Liu, X.; Luker, K.; Luker, G.; Weiss, S.; Takayama, S., Nanolitre Liquid Patterning in Aqueous Environments for Spatially Defined Reagent Delivery to Mammalian Cells. *Nat. Mater.* **2009,** *8*, 736-741.

50. Frampton, J. P.; White, J. B.; Simon, A. B.; Tsuei, M.; Paczesny, S.; Takayama, S., Aqueous Two-Phase System Patterning of Detection Antibody Solutions for Cross-Reaction-Free Multiplex ELISA. *Sci. Rep.* **2014,** *4*.

51. White, J. B. Aqueous Two-Phase Systems for Next-Generation Biotechnological Assays. University of Michigan, 2013.

52. Frampton, J. P.; Leung, B. M.; Bingham, E. L.; Lesher‐Perez, S. C.; Wang, J. D.; Sarhan, H. T.; El‐Sayed, M. E.; Feinberg, S. E.; Takayama, S., Rapid Self‐Assembly of Macroscale Tissue Constructs at Biphasic Aqueous Interfaces. *Adv. Funct. Mater.* **2015,** *25*, 1694-1699.

53. Armstrong, J. P.; Olof, S. N.; Jakimowicz, M. D.; Hollander, A. P.; Mann, S.; Davis, S. A.; Miles, M. J.; Patil, A. J.; Perriman, A. W., Cell Paintballing Using Optically Targeted Coacervate Microdroplets. *Chem. Sci.* **2015,** *6*, 6106-6111.

54. Matthew, H. W.; Salley, S. O.; Peterson, W. D.; Klein, M. D., Complex Coacervate Microcapsules for Mammalian Cell Culture and Artificial Organ Development. *Biotechnol. Progr.* **1993,** *9*, 510-519.

55. Sackmann, E. K.; Fulton, A. L.; Beebe, D. J., The Present and Future Role of Microfluidics in Biomedical Research. *Nature* **2014,** *507*, 181-189.

Chapter 2

Patchy Surfaces Stabilize Dextran−Polyethylene Glycol Aqueous Two-Phase System Liquid Patterns

This chapter interrogates surface chemistry effects to stably pattern aqueous two-phase system (ATPS) droplets on chemically modified poly(dimethylsiloxane) (PDMS). Polyethylene glycol (PEG) and dextran (DEX) are used as phase-forming polymers for the ATPS. PDMS surface modifications studied include primary amine groups, carboxylic acid groups, and neutral polymer surfaces. The PDMS surfaces were characterized by fluorescent measurement, water and DEX contact angle measurements, and X-ray photoelectron spectroscopy (XPS) analysis to confirm surface properties. While homogeneous surfaces of different functional groups affect DEX droplet pinning somewhat, the most stable patterns were realized using surfaces with chemical heterogeneity. Arbitrary DEX solution patterning was achieved on a chemically patchy surface.

2.1 Introduction

An aqueous two-phase system (ATPS) is composed of two immiscible aqueous polymer solutions, which forms two distinct aqueous phases. It has been widely developed as a molecular separation technique[1, 2], and recently, it has emerged as a useful tool for separating cells[3], biomolecules[4-6], and nanoparticles.[7] Among various phase-forming polymers, dextran (DEX) and polyethylene glycol (PEG) are biocompatible polymers that can form stable ATPS over a wide range of temperatures.[1] As such, ATPSs formed with the two polymers have been widely utilized for biomedical applications.[8-13]

An interesting and useful aspect of microscale DEX phase solution patterning over cell monolayers immersed in a PEG phase, for purposes such as localized gene delivery, is that despite immiscibility and presence of interfacial tension, the microscale patterns of DEX solution become pinned into arbitrary shapes rather than balling up into a circular shape.[14, 15] The DEX solution patterns had sub-millimeter resolution and showed long term stability.

Initial attempts to utilize non-cellular surfaces such as micro-topographical features to maintain DEX solution patterns failed[9] and the requirements for stably maintaining DEX solution patterns on a solid substrate submerged in the PEG phase has been unclear to date. Development of a technique to retain DEX solution patterns on a non-cellular surface in the PEG phase would be important both for advancing fundamental understanding of these systems as well as for expanding ATPS patterning applications beyond cell surfaces.

Here we hypothesize that chemical heterogeneity as may occur on a cell monolayer surface and associated surface-DEX solution interactions are essential to sustain DEX solution patterns within a PEG phase solution. We chemically modify PDMS surfaces and compare DEX solution pattern stability on the modified surface.

The PDMS surfaces were oxidized to anchor (3-aminopropyl)triethoxysilane (APTES) and further covalently modified with PEG, carboxymethyl dextran (CM-DEX), and diethylaminoethyl dextran (DEAE-DEX) by amine coupling through the well-known 1-ethyl-3-[3-dimethylaminopropyl]carbodiimide hydrochloride (EDC) and N-hydroxysuccinimide (NHS) coupling chemistry[16, 17] at room temperature. We characterized the surfaces by fluorescent measurement, contact angle measurement, and XPS spectroscopy and compared DEX solution pattern stability on the surfaces in a PEG phase. We also validated if gaps on the modified surface could influence DEX solution pattern stability and explored arbitrary DEX solution patterning on a chemically patchy surface.

2.2 Materials and Methods

Materials

All chemicals and reagents were purchased from commercial sources: PDMS precursor (sylgard 184) and curing agent were from Dow Corning; SU-8 2025 and SU-8 developers were from MicroChem; dimethyl sulfoxide anhydrous (DMSO), APTES, EDC, NHS, ethanol amine, Mw 35,000 PEG, Mw 500,000 DEX, and Mw 20,000 CM-DEX were from Sigma-Aldrich; Mw 500,000 DEAE-DEX was from AMRESCO; Mw 5000 PEG-NHS and Mw 5000 FITC-PEG-NHS were from Nanocs; Mw 500,000 FITC-DEAE-DEX and Mw 20,000 FITC-CM-DEX were from TdB; phosphate-buffered saline (PBS) buffer solution (pH 7.4) was from GE Health Care.

PDMS Fabrication

10:1 (w/w) degassed mixture of PDMS and a curing agent was poured on a plastic dish and cured at 60 °C for at least 4 hours in the oven. A PDMS slab was peeled off from the dish. A clean glass microscope slide was spin-coated with the same mixture and cured under the same condition.

Microfabrication

Masters for partial modification were made by spin coating SU-8 onto a silicon wafer. SU-8-coated wafers were then soft-baked (first step: 3 min, 65 °C; second step: 6 min, 95 °C), exposed, post-baked (first step: 1 min, 65 °C; second step: 6 min, 95 °C), and developed to obtain 50 µm thickness. After silanization, degassed PDMS was poured and cured on the masters. The PDMS replica was peeled off from the master and physically bonded to a PDMS slab to form a microchannel for partial chemical modification.

Surface Modification

The PDMS surface was coated with polymers through covalent bonding (Scheme 2.1). Oxidation and APTES-derivitization of PDMS were carried out by the previously reported method (Scheme 2.1A and 2.1B).[18] PEG, CM-DEX, and DEAE-DEX were covalently bound to the PDMS surface by EDC/NHS coupling chemistry. PEG-NHS (30 mg, 6 mmol) or CM-DEX (30mg, 29 µmol) dissolved in 1:1 mixture of 100 mg/mL EDC/NHS was incubated for 20 min to activate and applied on the primary amine-terminated APTES surface for 1 hour followed by extensive wash in water (Scheme 2.1C and 2.1D). For DEAE-DEX modification, the primary amine-terminated surface was carboxylated by applying 1 mg/mL succinic anhydride in dry DMSO for 10 min (Scheme 2.1E).[19] The converted carboxyl surface was activated by the mixture of EDC/NHS for 20 min and washed in water.[20] DEAE-DEX (30mg, 43 μmol) dissolved in 100 mM NaOH water was incubated on the surface for 1 hour followed by extensive wash in water (Scheme 2.1F). All modified surfaces were used in a day and discarded after use. For partial modification, the same protocol was conducted within a microchannel.

Surface Characterizations

Equilibrated PEG and DEX solutions were prepared as described elsewhere.[14, 15] A chemically modified PDMS slab was punched out with a 6 mm-diameter biopsy punch (Miltex) and attached on the bottom of a hand-made glass container (3cm x 3cm x 1.5cm). The container was used for contact angle and sliding angle measurements of sessile DEX droplet in the PEG phase (Figure 2.10).

Contact Angle Measurement

Water contact angles in air (Figure 2.10A) and DEX solution contact angles in PEG phase solutions (PEG-DEX w/w concentration: 2.5% - 3.2%, 2.5% - 15%, and 15% - 3.2%) (Figure 2.10B) were measured on bare PDMS, APTES-modified PDMS, PEG-modified PDMS, CM-DEX-modified PDMS, and DEAE-DEX-modified PDMS by the sessile drop technique (2 μL of water in air or 0.1 μL of DEX in 2mL PEG solution) using a goniometer and analyzed with ImageJ. Three sets of measurements were averaged.

Sliding Angle Measurement

A glass container with a chemically modified PDMS at the bottom was filled with 2 mL PEG solution and 0.1 μL of DEX in 3.2% DEX - 15% PEG system was dropped on the modified surface. The container was attached to the goniometer and tilted until the DEX droplet started sliding. Images were taken at that point and advancing, receding, and sliding angles were analyzed by ImageJ. Three sets of measurements were averaged.

XPS Analysis

A chemically modified PDMS membrane was peeled off from a glass slide and the membrane surface was measured by XPS (Kratos Axis Ultra XPS) with aluminum X-ray radiation source 15 kV and pass energy of 160 eV. Acquired XPS data were analyzed by CasaXPS.

Fluorescence Measurements of Surface Modifications

Bare PDMS surfaces were partially covered by taping before oxidation (Scheme 2.2). 1 mg of FITC-PEG-NHS, FITC-CM-DEX, and FITC-DEAE-DEX were covalently bound to the surface by the aforementioned method. Fluorescence was measured using a fluorescence microscope (Nikon Eclipse TE 2000-U) and analyzed by NIS-elements software.

Analysis of ATPS droplets formed on surfaces patterned in shapes of alphabet letters

PDMS surface was modified in the shape of letters “U” and “M” using microchannels of the corresponding shapes (Scheme 2.3A). The region outside the letters is a native PDMS surface. A few μL of DEX (~ 5 μL) in 3.2% DEX - 2.5% PEG system was dispensed onto the surface modified region (Scheme 2.3B) and images taken under a stereomicroscope (Nikon C-DSD115). The same process was repeated with 0.01 mg/mL FITC-DEX and imaged by fluorescence microscopy.

Analysis of formation of continuous ATPS droplet patterns on discontinuously patterned surfaces

Five PDMS square regions (1.5 mm x 1.5 mm) with inter-square edge-to-edge distances of 100 μm, 300 μm, 500 μm, or 1 mm were prepared with either DEAE-DEX or CM-DEX modification (Figure 2.12B). A few μL of DEX solution (~ 5 μL) was dispensed along the patterns using a 3.2% DEX - 2.5% PEG system. Images were taken with a stereomicroscope.

Analysis of formation of arbitrary ATPS droplet patterns on a discontinuously patterned surface

Arrays of PDMS square regions (1.0 mm x 1.0 mm) with inter-square edge-to-edge distances of 100 μm, 300 μm, 500 μm, or 1 mm were prepared with CM-DEX modification (Figure 2.12C). A few μL of DEX solution (~ 7 μL) containing 0.01 mg/mL FITC-DEX was dispensed onto the same surface along the arbitrary shapes of letters "L" and "U" using a 3.2% DEX - 2.5% PEG system. Images were taken by fluorescence microscopy.

2.3 Results and Discussion

Modification of surfaces was confirmed by visualizing that only the chemically-modified left side shows fluorescence (Figure 2.1 and Scheme 2.2). We observed almost no fluorescence when

100 mM ethanolamine (a deactivating agent[21]) was mixed with the EDC/NHS solutions during the activation process, consistent with the notion that the fluorescence-inducing surface modifications occur by amine coupling (Figure 2.9).

The chemically-modified surfaces were also analyzed by XPS for C1s, N1s and O1s peaks as shown in Figure 2.2. The trends for the peaks of APTES-modified surface agreed well with previously reported results.[18] Briefly, the quantity of carbon atoms (C) decreased because oxidation of bare PDMS surface replaced the methyl groups with hydroxyl groups. Meanwhile, the quantities of nitrogen atom (N) and oxygen atom (O) increased as a result of the APTES derivitization. C1s, N1s and O1s spectra for PEG, DEAE-DEX, and CM-DEX modified surfaces showed shoulder peaks and differing binding energy shifts, according to changes in the polymer backbone and side chains. These results indicate that the PDMS surface was successfully modified.

Figure 2.3 shows results of water contact angle measurements. The measured contact angles on bare PDMS[22], APTES-modified[18] and PEG-modified PDMS[23] agreed well with previously reported values. Young's equation defines the general expression of contact angle (Figure 2.10A) and illustrates that the contact angle decreases as the surface becomes hydrophilic. The results revealed that the surface became more hydrophilic from bare PDMS, to APTES-modified, PEG-modified, DEAE-DEX-modified, and CM-DEX-modified PDMS in that order. DEX solution contact angle measurements performed in PEG phase solutions revealed similar trends as shown in Figure 2.4.

The DEX solution contact angles measured in PEG solutions also follow Young's equation (Figure 2.10B). As either PEG or DEX concentrations in the phase forming solutions increased, the DEX solution contact angles on the modified surfaces fluctuated due to changes in the surface affinity difference (Figure 2.12A; γ_{1S} - γ_{2S}) whereas CM-DEX-modified PDMS surface showed the highest affinity to the DEX phase in all cases. These results are consistent with the fact that the DEX phase is more hydrophilic than the PEG phase, and therefore DEX contact angles on the modified surfaces follow the trends observed in water contact angle measurements.

These trends were further confirmed by sliding angle measurements as shown in Figure 2.5. CM-DEX-modified PDMS surfaces demonstrated the highest hysteresis and the largest sliding angles among the five types of surfaces. A linear correlation was observed between the hysteresis and sliding angle, reflecting the surface affinity. As a result, surface affinity to the DEX phase increased from bare PDMS to APTES-modified, PEG-modified, DEAE-DEX-modified, and CM-DEX-modified PDMS in that order.

We analyzed DEX solution pattern stability on chemically modified PDMS surfaces when submerged in PEG phase solution (Figure 2.6 and Figure 2.11). First, we attempted DEX solution patterning on uniformly chemically modified surfaces and observed patterns of DEX round up within 1 min. We next created PDMS surfaces where only select regions were modified with PEG, DEAE-DEX or CM-DEX (Scheme 2.3) and found that DEX solution patterns in PEG solution could be retained for hours on the CM-DEX surface while DEX solution patterns on the other surfaces rounded up or significantly deviated from its original pattern within 1 min (Figure 2.6A-C and Figure 2.11A-C). We reveal that use of a heterogeneously patterned surface together with low interfacial tension PEG-DEX solutions is the key to maintain stable DEX solution patterning. Thermodynamically speaking, the heterogeneously modified surface gives rise to surface energy barriers that pin the contact line of the DEX solution.[24] It has been theoretically[25, 26] and empirically[27] demonstrated that a solid surface with chemical gradients drives the motion of a water droplet from hydrophobic surface to more hydrophilic sections due to different surface energy states. We hypothesize that the DEX solution pattern stability arises from the difference in affinity of the DEX solution for each surface (Figure 2.12A). Greater the DEX affinity difference between surfaces, higher the surface energy barriers become.

To clearly visualize the patterns, we utilized fluorescent DEX solution on DEAE-DEX-modified and CM-DEX-modified heterogeneous PDMS surfaces (Figure 2.6D and 6E). The patterns on the CM-DEX-modified surface were sharp and stable while those on the DEAE-DEX modified surface were stable but blurred (Figure 2.11D and 11E). As described previously, DEX molecules demonstrated stronger affinity to the CM-DEX-modified surface than the DEAE-DEX-modified surface. Consequently, there should be a higher surface energy barrier between bare PDMS and CM-DEX-modified PDMS than with DEAE-DEX-modified PDMS. The result is consistent with the aforementioned hypothesis.

Heterogeneous surfaces with defects or patchy surface patterning are known to influence contact line pinning.[28] To analyze such effects on ATPS solution patterning, we investigated how discontinuous or patchy surface patterns influence DEX solution pattern stability within PEG phase solutions (Figure 2. 12B and 12C). Figure 2.7 shows a DEX solution line created on surfaces modified with discontinuous DEAE-DEX or CM-DEX surface patterns on a background of native PDMS. The area fraction of defects (f_d) is correlated to the distance between the surface modified regions. As f_d increases (that is, the gap between patchy patterns increases), the DEX solution lines became unstable, resulting in partial collapse of the line pattern. Interestingly, to prevent a DEX solution line pattern from breaking up into droplets, the distance between modified surface patches needed to be smaller for the higher affinity CM-DEX modified surfaces (critical f_d = 0.096) compared to patchy patterns of DEAE-DEX (critical f_d = 0.25). We assume that strong adhesion of a DEX solution on CM-DEX-modified surfaces may tear off the DEX solution line easily in comparison with DEAE-DEX-modified surfaces (Figure 2.13A and 13B). As f_d increases, the affinity imbalance between different regions of the DEX solution line exerts a larger effect, resulting in instability and breakup of the solution line pattern (Figure 2.13C and 13D).

When the CM-DEX-modified patches were arrayed in a grid with appropriate spacing between patches, the same grid pattern could be used to create arbitrary DEX droplet patterns on it (Figure 2.12C). The CM-DEX-modified grids with 100 μm inter-patch edge-to-edge distances (f_d = 0.14) successfully pinned the DEX phase solution in shapes of the letters "L" and "U" and stably maintained the patterns (Figure 2.8A and 8B). In contrast, the droplet patterns created on grids with inter-patch distances over 300 μm (f_d = 0.35 - 0.69) could not maintain droplet shapes and gradually collapsed (Figure 2.8C-F). The results consistent with the line pattern measurements suggest that ATPS solution pinning rely on the area fraction of defects. The contact line of the DEX phase solution moderately spread after dispensing onto the surface until the forwarding contact line became pinned by surface discontinuity (Figure 2.14). Similar phenomena of spreading and pinning have been observed upon patterning DEX solutions over cell monolayers. This phenomena similar to wetting transition from the Cassie-Baxter state to the Wentzel state at an air-liquid interface[29] implies that the similar wetting transition mechanism can be valid at a liquid-liquid interface.

2.4 Conclusions

Aqueous two phase system droplets on most surfaces, including topographically patterned but chemically homogeneous surfaces,[9] form rounded circular structures to minimize the surface energy. Previously we demonstrated, however, that substrates coated with biological cells have the ability to pin the contact lines enabling formation of ATPS droplets in arbitrary patterns.[9,10]

Inspired by the chemical heterogeneity of cell surfaces which display various functional groups such as glycoproteins, globular proteins, and phospholipid heads,[30] we developed non-cellular topographically flat surfaces that also have a degree of chemical heterogeneity across length scales of several hundreds of micrometers to millimeters.

While none of the surfaces that were homogenously modified, despite differences in affinity for the DEX solution phase, could stabilize DEX solution patterns formed within a PEG phase solution, a variety of patterned and discontinuous patchy surfaces could. Surfaces patterned in the shape of letters were able to maintain DEX solution droplets in such shapes indefinitely although with different sharpness of the features depending on affinity of that surface to the DEX solutions.

More importantly, surfaces patterned with an array of small patches of modified surfaces were able to maintain DEX solution droplets in the shape of a line that stably bridge multiple patches as long as the distance between patches were below a critical distance. Such surface patchiness successfully achieved arbitrary DEX solution patterns on the same underlying substrate similar to how a surface with an array of cells is able to stably maintain DEX solution patterns.

Our technique enables precise distance and dimension control of DEX solution patterns, with potential applications to cell migration[13], bacterial colonial communication[10] and other biomedical studies using DEX-PEG ATPS. Moreover, our technique can expand to other ATPS such as PEG-salt systems and sheds light on the fundamental mechanism of contact line pinning at liquid-liquid interfaces.

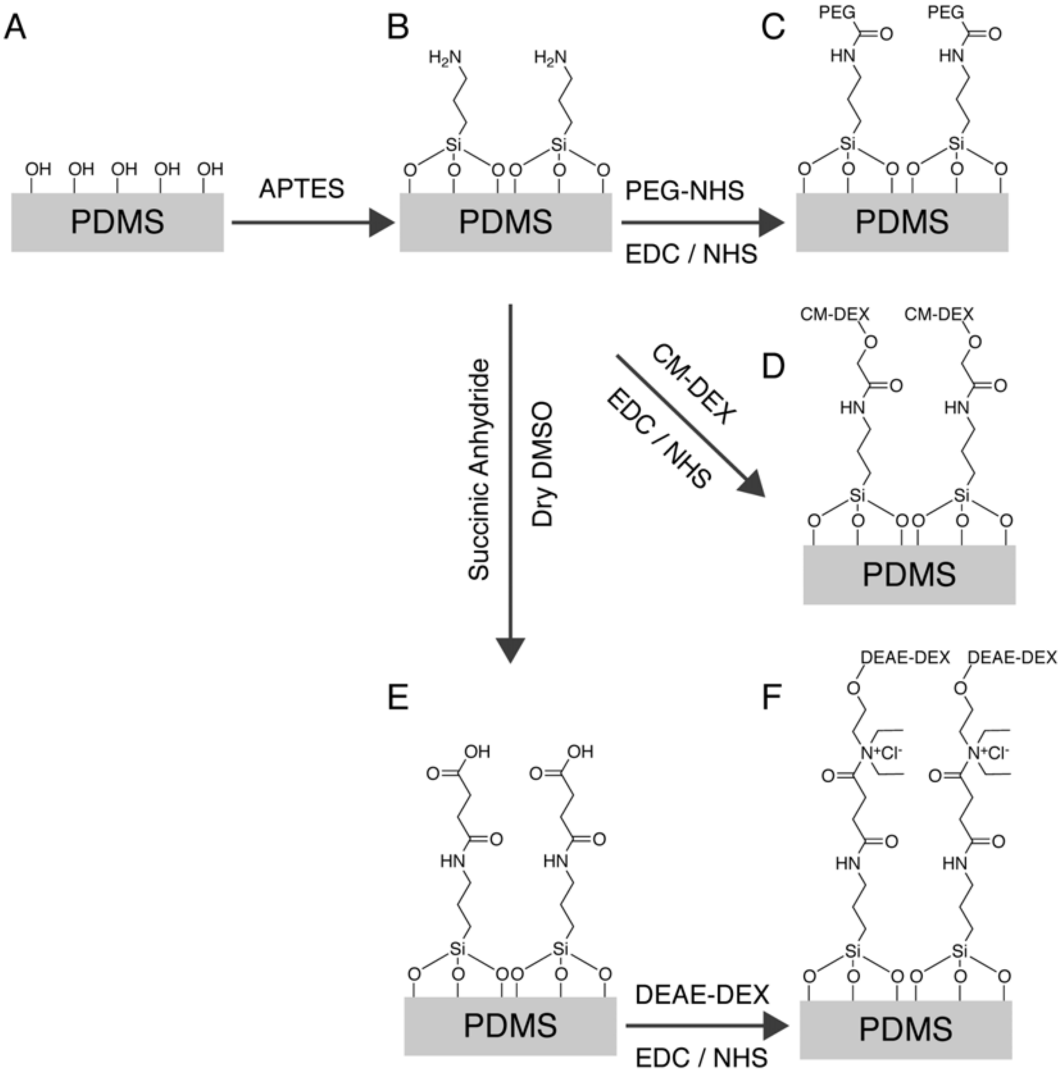

Scheme 2.1. A) O_2 plasma treatment of PDMS, B) primary amine-derivitization of plasma-treated PDMS with APTES, C) PEG-derivitization of APTES-modified PDMS through amine coupling, D) CM-DEX-derivitization of APTES-modified PDMS through amine coupling, E) carboxylation of APTES-aminated PDMS with succinic anhydride, and F) DEAE-DEX-derivitization of carboxylated PDMS through amine coupling.

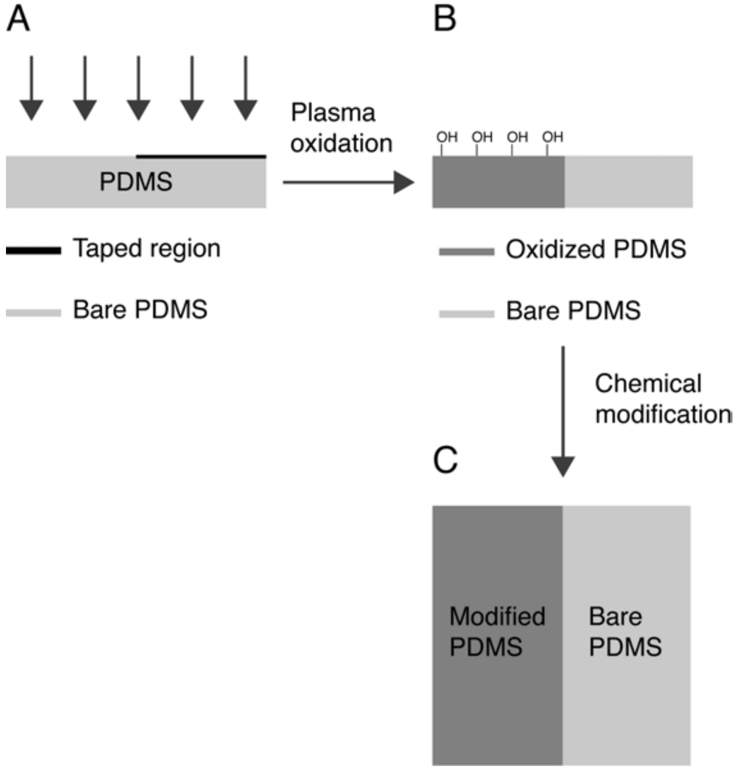

Scheme 2.2. A) Plasma treatment on the PDMS surface where the half right side is covered by taping, B) oxidized PDMS and bare PDMS surfaces, and C) chemical modification on the surfaces.

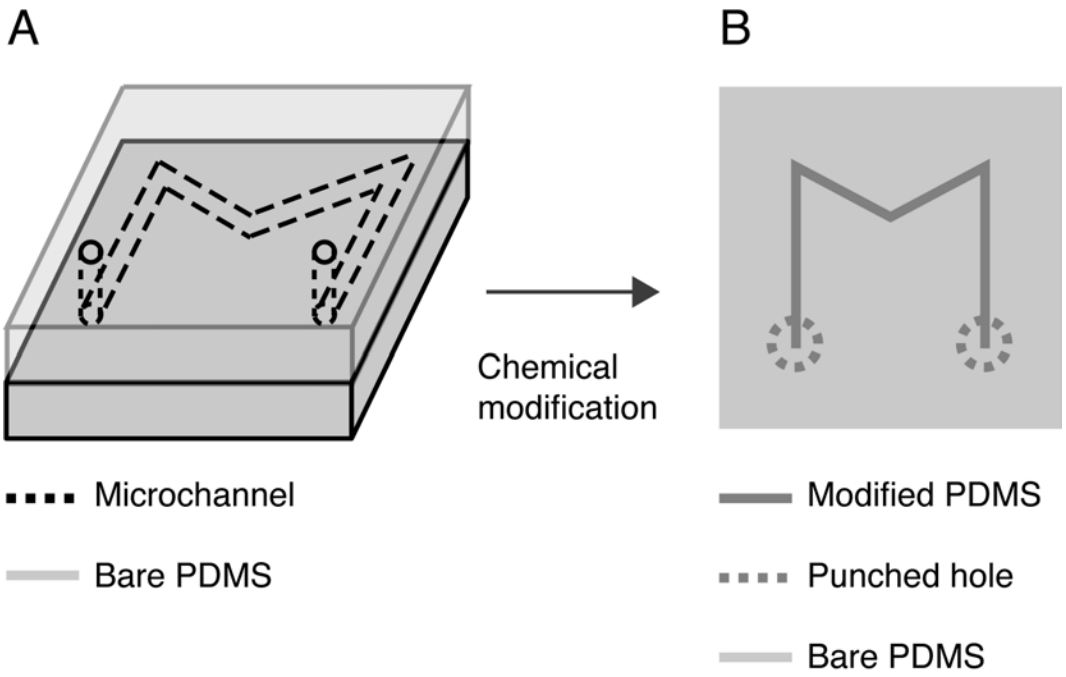

Scheme 2.3. A) Surface modification of PDMS within a microchannel and B) heterogeneous surface patterned by letter M.

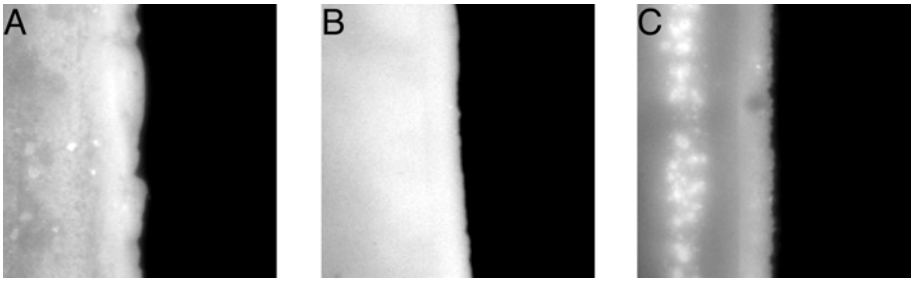

Figure 2.1. Fluorescence measurement of chemically modified PDMS surfaces: A) FITC-PEG-modified PDMS, B) FITC-DEAE-DEX-modified PDMS and C) FITC-CM-DEX-modified PDMS prepared according to Scheme 2.1 and 2.2.

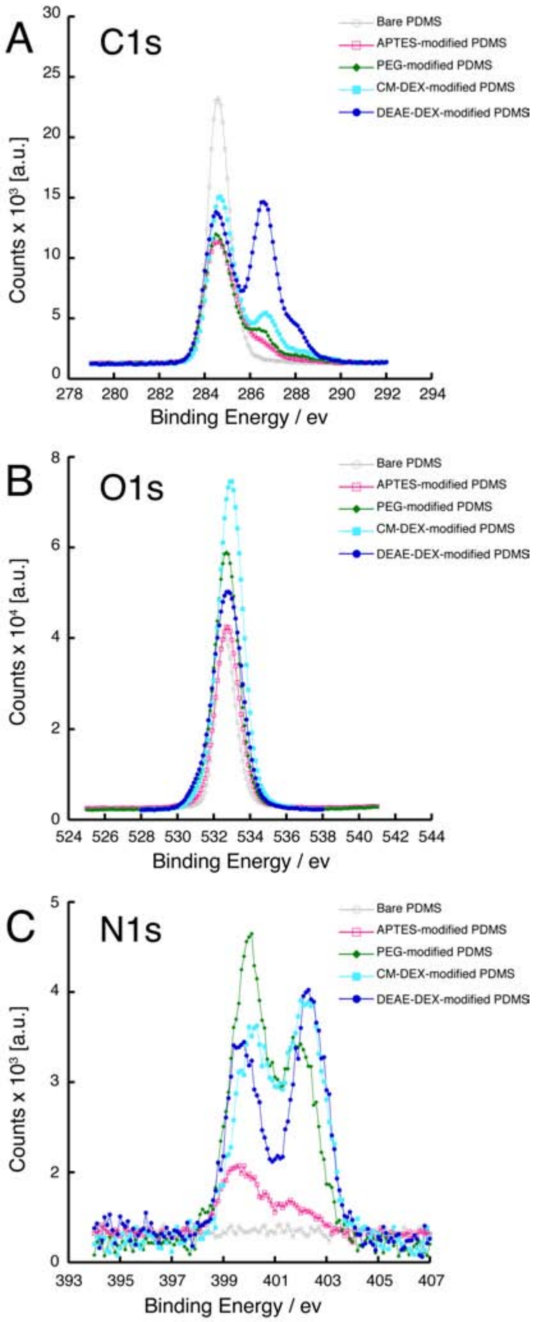

Figure 2.2. XPS analyses of chemically modified PDMS surfaces: A) C1s peaks, B) N1s peaks, and C) O1s peaks measured on the surfaces of bare PDMS (gray open circle), APTES-modified PDMS (magenta open square), PEG-modified PDMS (green closed rhombus), CM-DEX-modified PDMS (sky blue closed square), and DEAE-DEX-modified PDMS (blue closed circle).

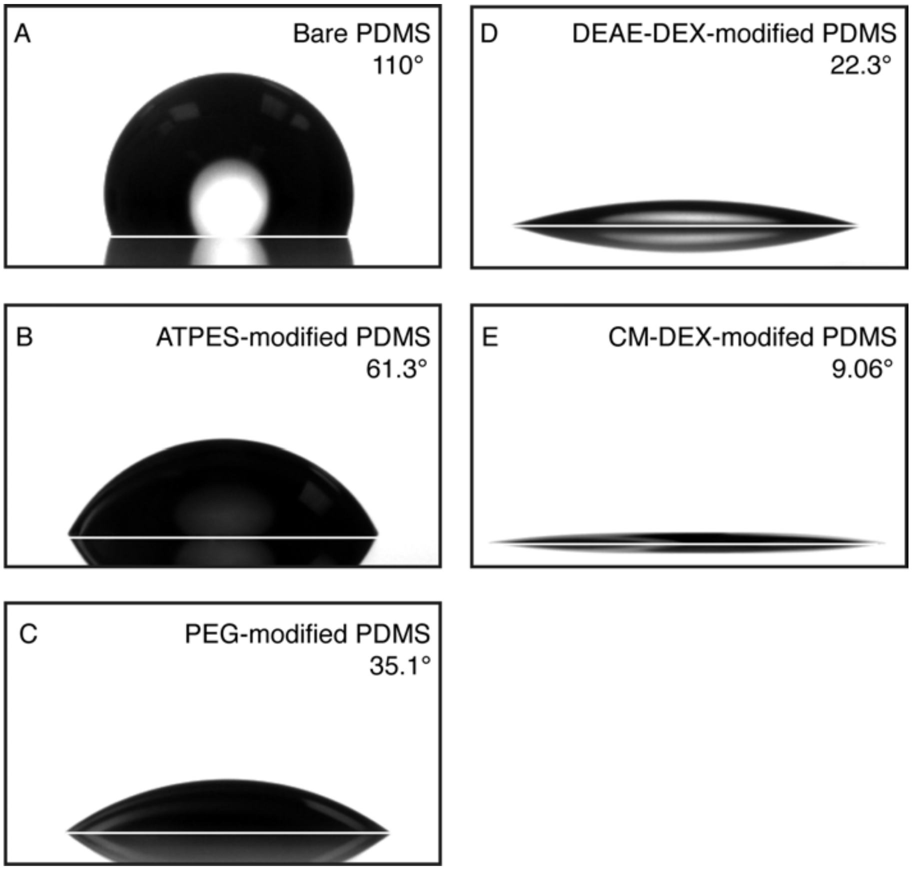

Figure 2.3. Contact angle measurements of sessile water droplet in air on different surfaces: A) bare PDMS, B) APTES-modified PDMS, C) PEG-modified PDMS, D) DEAE-DEX-modified PDMS, and E) CM-DEX-modified PDMS.

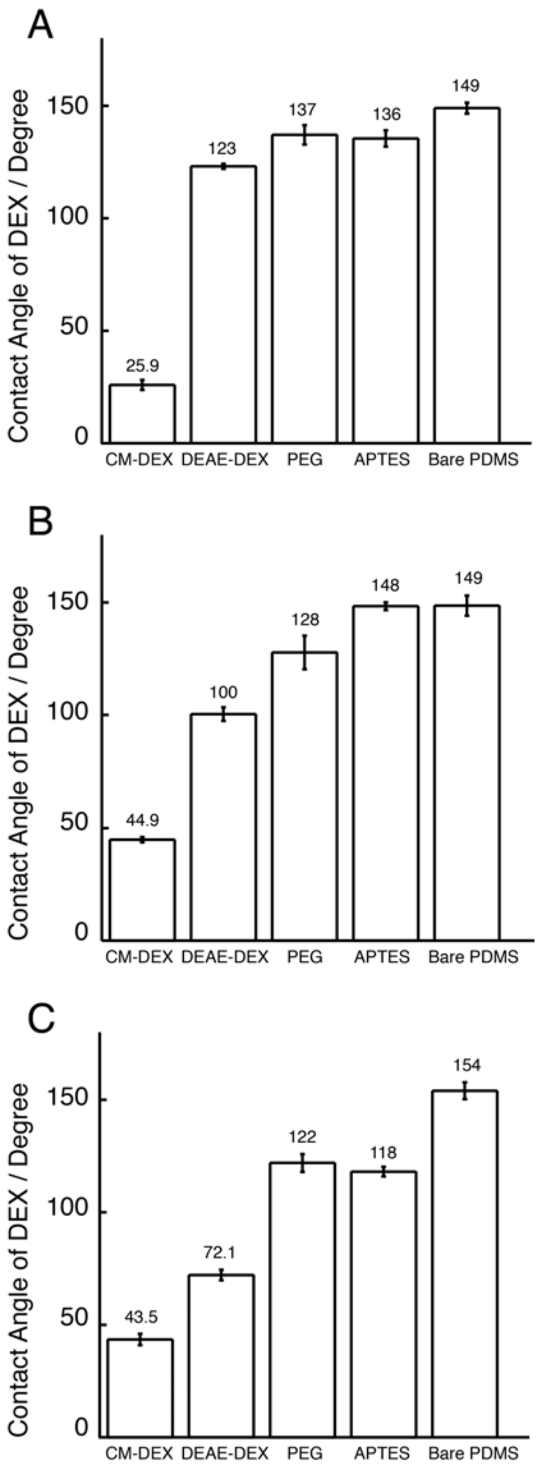

Figure 2.4. Contact angle measurements of sessile DEX droplet in the PEG phase on bare PDMS, APTES-modified PDMS, PEG-modified PDMS, DEAE-DEX-modified PDMS, and CM-DEX-modified PDMS in differing DEX-PEG systems: A) 3.2% DEX – 2.5% PEG, B) 3.2% DEX – 15% PEG, and C) 15% DEX – 2.5% PEG.

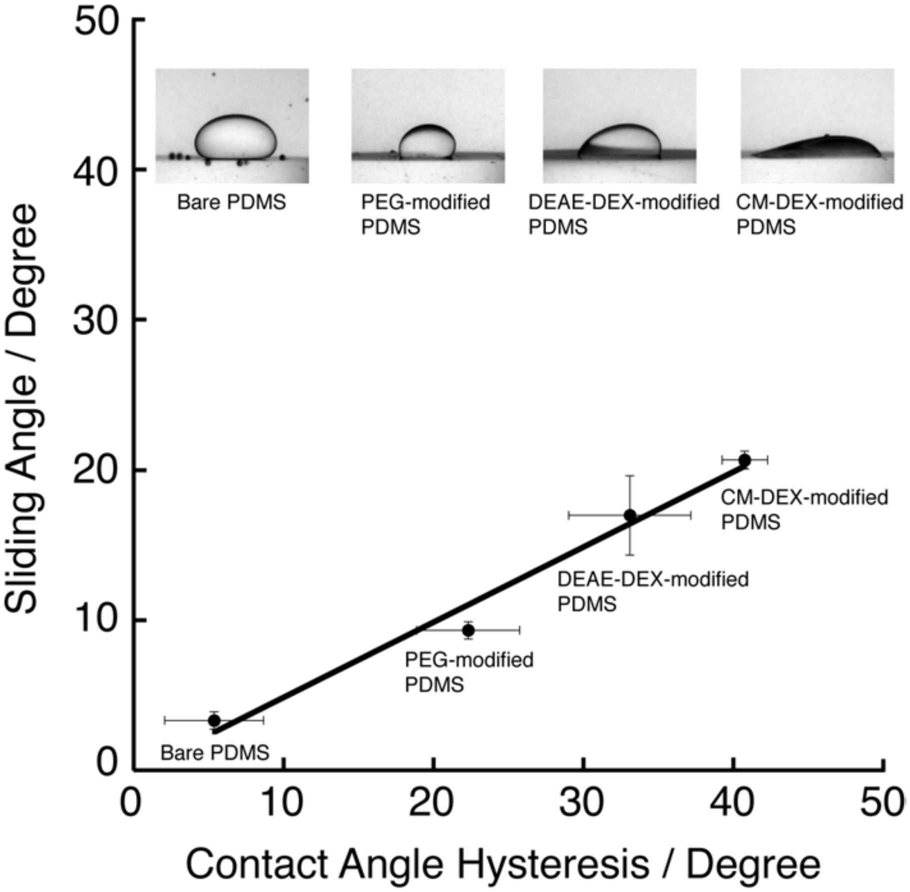

Figure 2.5. Sliding angle and hysteresis measurements of sessile DEX droplet in the PEG phase on surfaces. Sliding angle as a function of contact angle hysteresis on bare PDMS, APTES-modified PDMS, PEG-modified PDMS, DEAE-DEX-modified PDMS, and CM-DEX-modified PDMS in 3.2% w/w DEX – 15% w/w PEG system.

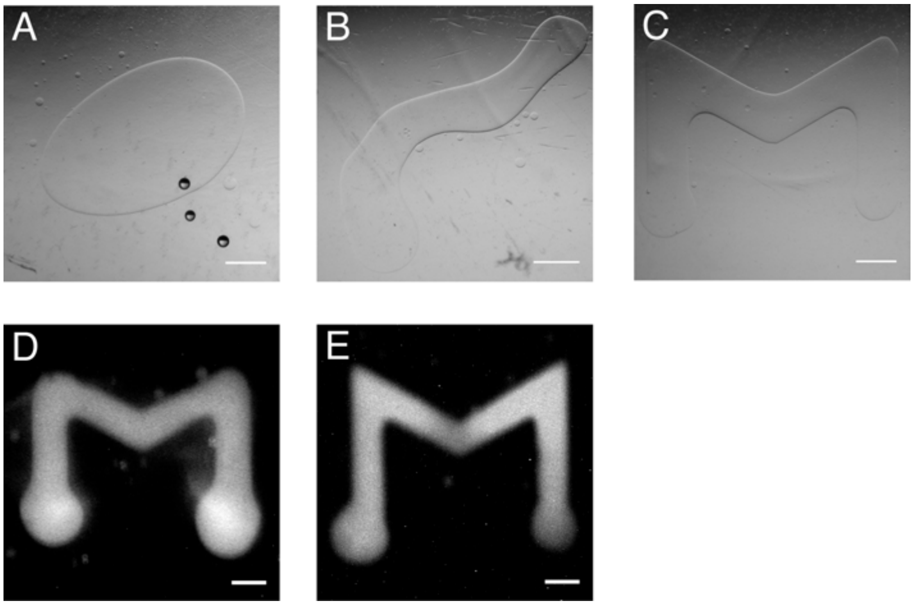

Figure 2.6. DEX solution patterns in 3.2% w/w DEX – 2.5% w/w PEG system. The phase contrast images of letter “M” on A) bare PDMS, B) PEG-modified PDMS, and C) DEAE-DEX-modified PDMS, and the fluorescent images of letter M on D) DEAE-DEX-modified PDMS and E) CM-DEX-modified PDMS. The patterned surfaces were prepared according to Scheme 2.1 and 2.3. Scale bar 1 mm.

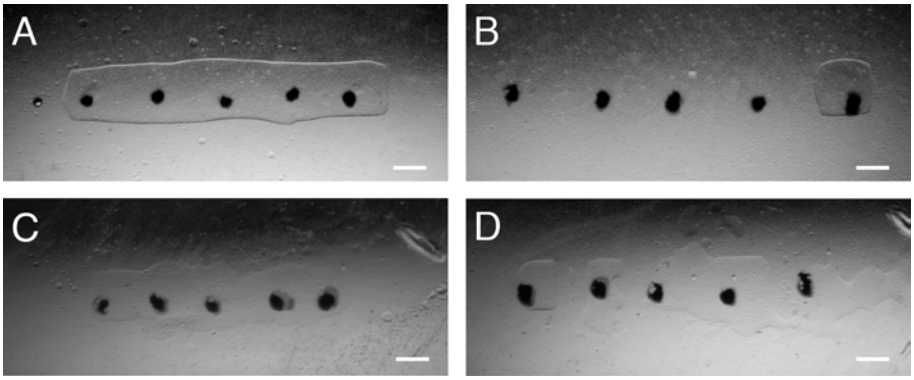

Figure 2.7. DEX phase solution lines formed on surface-modified square patches (1.5 millimeter long edges) with different inter-patch spacing analyzed with a 3.2% w/w DEX – 2.5% w/w PEG system. The DEX phase solution lines were drawn on DEAE-DEX-modified patches formed on a background of native PDMS with inter-patch edge-to-edge distances of A) 500 µm (the area fraction of defects: $f_d = 0.21$) and B) 1 mm ($f_d = 0.35$). Similarly, DEX phase solution lines were formed on CM-DEX-modified patches where inter-patch distances were C) 200 µm ($f_d = 0.096$) and D) 300 µm ($f_d = 0.14$). Black dots are markings used to locate surface modified patches and correlate to the rough positions, although they do not represent the actual chemically modified patch shape. Scale bar 1mm.

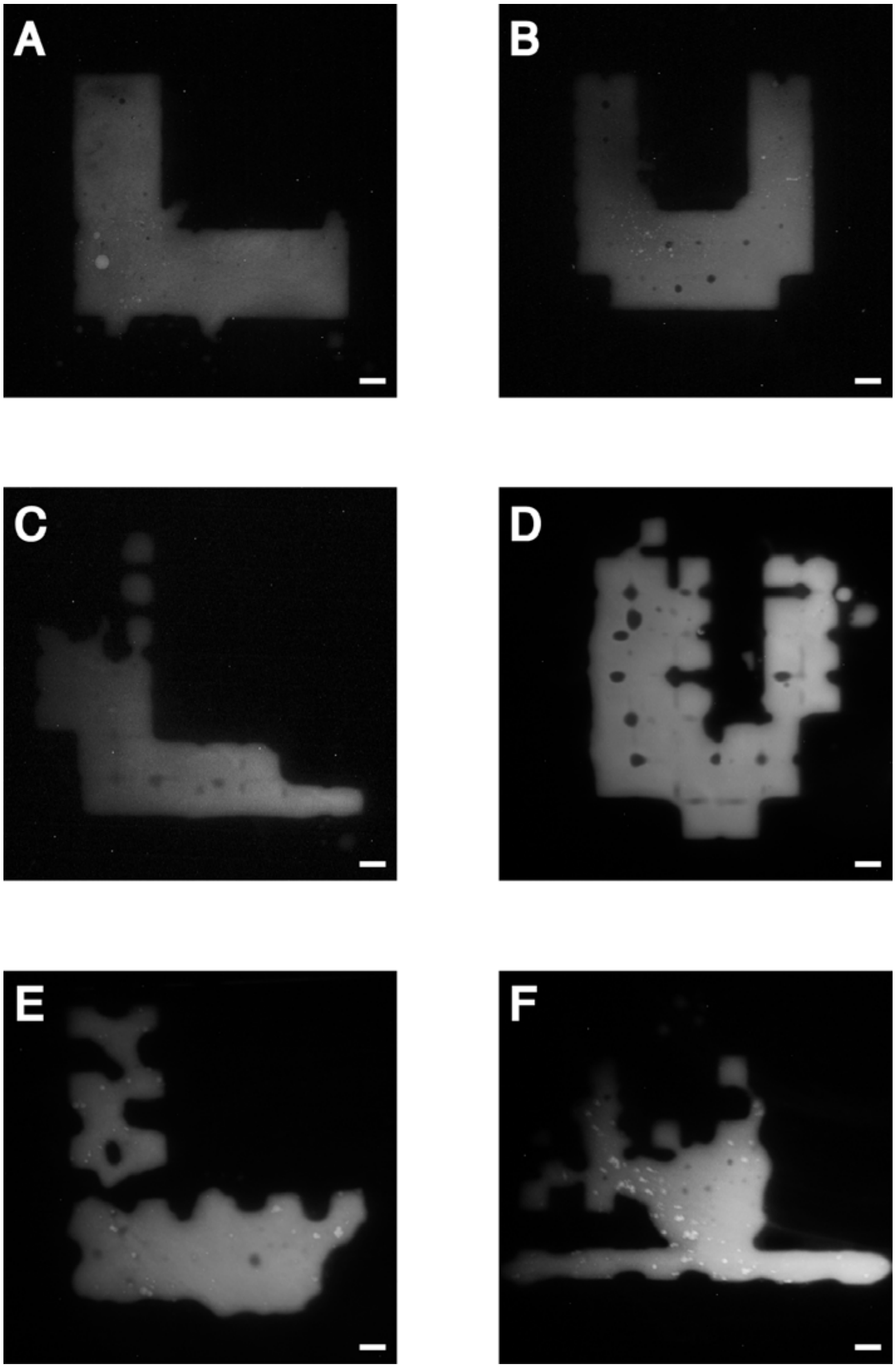

Figure 2.8. Arbitrary DEX phase solution patterns in a 3.2% w/w DEX – 2.5% w/w PEG system formed on surface-modified with square grids (1.0 millimeter long edges) that have different inter-patch spacing. The fluorescent DEX phase solution patterns of the letters “L” and “U” were drawn on CM-DEX-modified grids formed on a background of native PDMS with inter-patch edge-to-edge distances of A-B) 100 μm ($f_d = 0.14$), C-D) 300 μm ($f_d = 0.35$), and E-F) 1 mm ($f_d = 0.69$). Scale bar 1mm.

Figure 2.9. Fluorescent measurement: A) FITC-PEG-modified PDMS, B) FITC-DEAE-DEX-modified PDMS, and C) FITC-CM-DEX-modified PDMS

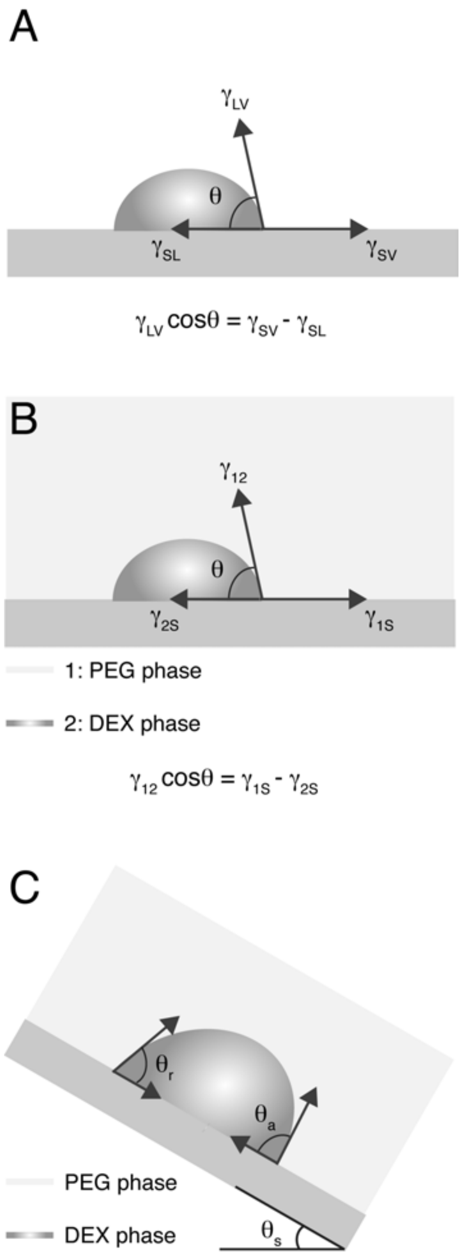

Figure 2.10. Contact angle measurements: A) Contact angle measurement of sessile water droplet in air and B) contact angle measurement of sessile DEX droplet in PEG solution. γ_{LV}, γ_{SL} and γ_{SV} are the interfacial tension at the liquid-vapor, solid-liquid, and solid-vapor interfaces, respectively. Similarly, γ_{12}, γ_{1S}, and γ_{2S} are the interfacial tension at the PEG-DEX, PEG-solid, and DEX-solid interfaces, respectively. C) Contact angle hysteresis measurement. θ_A, θ_B, and θ_S represent advancing angle, receding angle and sliding angle, respectively. Contact angle hysteresis is expressed as (θ_A - θ_B).

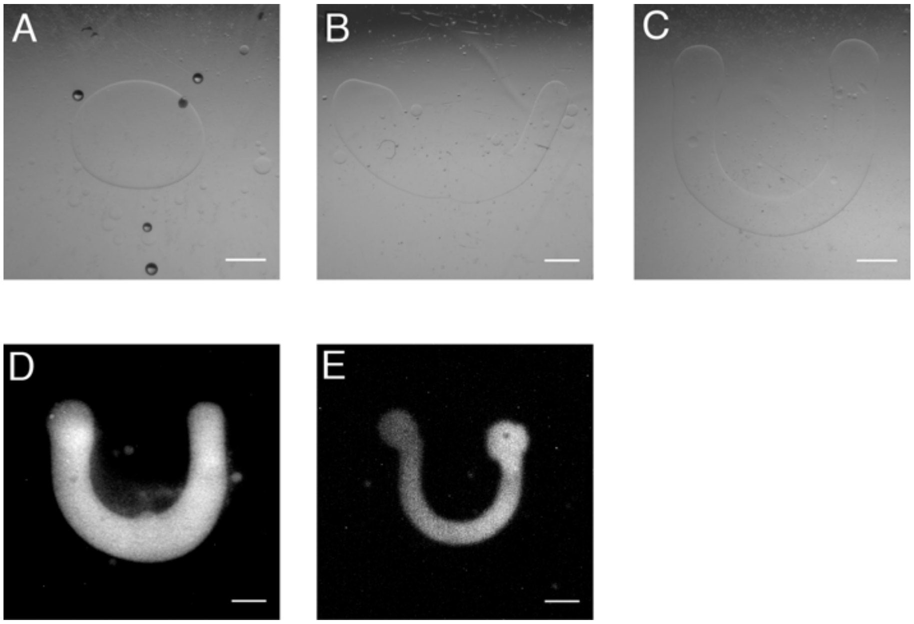

Figure 2.11. DEX patterns in 3.2% w/w DEX – 2.5% w/w PEG system. The phase contrast images of letter M on A) bare PDMS, B) PEG-modified PDMS, and C) DEAE-DEX-modified PDMS, and the fluorescent images of letter M on D) DEAE-DEX-modified PDMS and E) CM-DEX-modified PDMS. The patterned surfaces were prepared according to Scheme 2.1 and 2.3. Scale bar 1 mm.

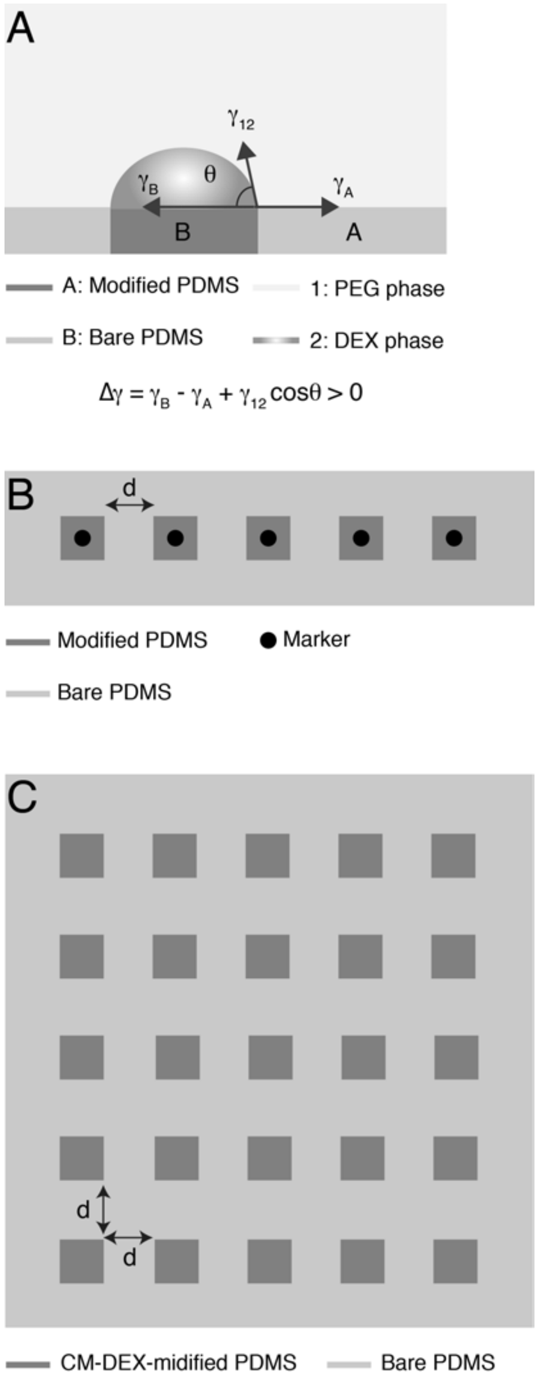

Figure 2.12. Patchy surfaces used: A) DEX phase on discontinuously modified PDMS surface in the PEG phase. γ_{12} is the interfacial tension at the PEG-DEX and $\Delta\gamma$ is the surface energy barrier between modified PDMS surface and bare PDMS. B) An array of modified patches on a background of native PDMS. C) Arrays of CM-DEX-modified patches on a background of native PDMS. d represents the inter-patch edge-to-edge distance.

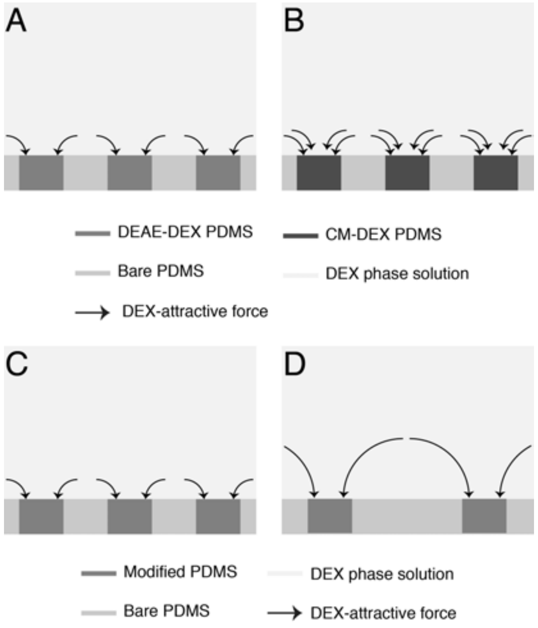

Figure 2.13. Surface adhesion and gap effects on DEX solution line stability. Enforcing surface affinity to DEX phase (A to B) or increasing the inter patch-to-patch distance (C to D) can break up a DEX solution line.

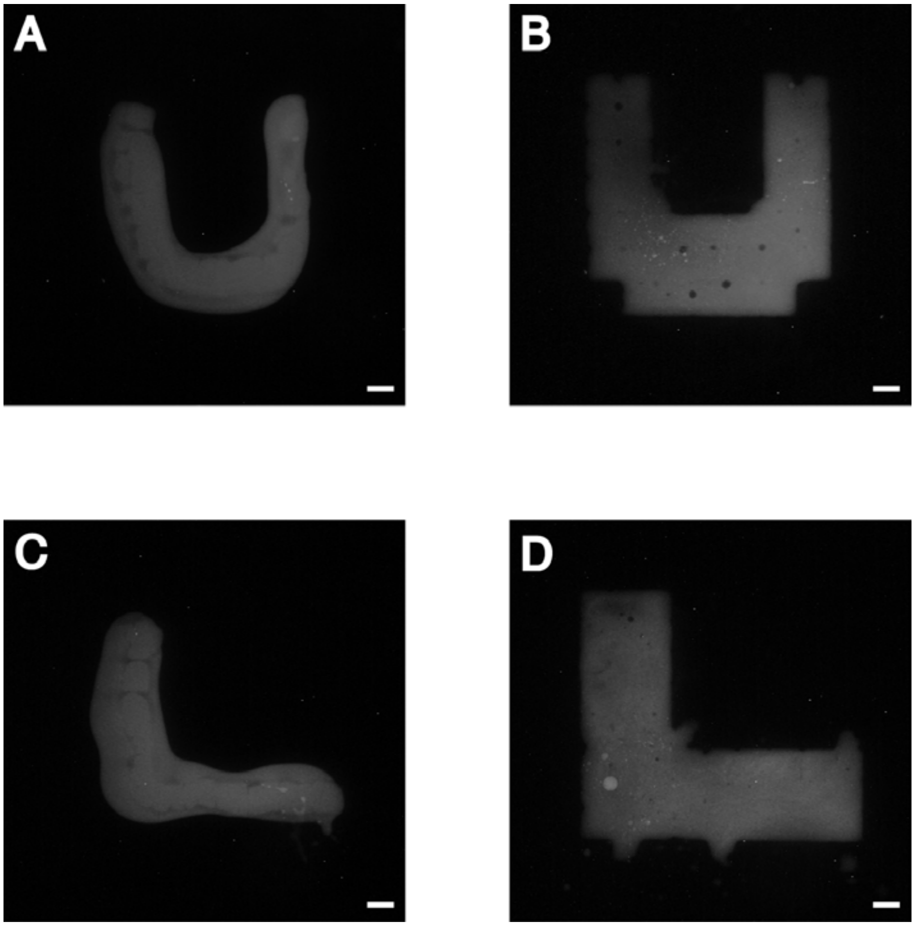

Figure 2.14. Spreading and pinning of arbitrary patterns after dispensing DEX solutions onto a CM-DEX-modified patchy surface. Initial shapes of DEX patterns (A and C) followed by spreading and pinning (B and D). Scale bar 1 mm.

2.5 References

1. Albertsson, P.-Å., *Partition of Cell Particles and Macromolecules*. 3rd ed.; John Wiley & Sons, Inc.: 1986.

2. Hatti-Kaul, R., *Aqueous Two-Phase Systems: Methods and Protocols*. Humana Press, Inc.: 2000.

3. Fang, Y.; Frampton, J. P.; Raghavan, S.; Sabahi-Kaviani, R.; Luker, G.; Deng, C. X.; Takayama, S., Rapid Generation of Multiplexed Cell Cocultures Using Acoustic Droplet Ejection Followed by Aqueous Two-Phase Exclusion Patterning. *Tissue Eng. Part C* **2012,** *18*, 647-657.

4. Keating, C. D., Aqueous Phase Separation as a Possible Route to Compartmentalization of Biological Molecules. *Acc. Chem. Res.* **2012**.

5. Mashayekhi, F.; Chiu, R. Y.; Le, A. M.; Chao, F. C.; Wu, B. M.; Kamei, D. T., Enhancing the Lateral-Flow Immunoassay for Viral Detection using an Aqueous Two-Phase Micellar System. *Anal. Bioanal. Chem.* **2010,** *398*, 2955-2961.

6. Mashayekhi, F.; Meyer, A. S.; Shiigi, S. A.; Nguyen, V.; Kamei, D. T., Concentration of Mammalian Genomic DNA using Two-Phase Aqueous Micellar Systems. *Biotechnol. Bioeng.* **2009,** *102*, 1613-1623.

7. Akbulut, O.; Mace, C. R.; Martinez, R. V.; Kumar, A. A.; Nie, Z.; Patton, M. R.; Whitesides, G. M., Separation of Nanoparticles in Aqueous Multiphase Systems through Centrifugation. *Nano Lett.* **2012,** *12*, 4060-4064.

8. SooHoo, J. R.; Walker, G. M., Microfluidic Aqueous Two Phase System for Leukocyte Concentration from Whole Blood. *Biomed. Microdevices* **2009,** *11*, 323-329.

9. Frampton, J. P.; Fan, Z.; Simon, A.; Chen, D.; Deng, C. X.; Takayama, S., Aqueous Two-Phase System Patterning of Microbubbles: Localized Induction of Apoptosis in Sonoporated Cells. *Adv. Funct. Mater.* **2013,** *23*, 3420-3431.

10. Byun, C. K.; Hwang, H.; Choi, W. S.; Yaguchi, T.; Park, J.; Kim, D.; Mitchell, R. J.; Kim, T.; Cho, Y.-K.; Takayama, S., Productive Chemical Interaction between a Bacterial Microcolony Couple is Enhanced by Periodic Relocation. *J. Am. Chem. Soc.* **2013,** *135*, 2242-2247.

11. Strulson, C. A.; Molden, R. C.; Keating, C. D.; Bevilacqua, P. C., RNA Catalysis through Compartmentalization. *Nat. Chem.* **2012,** *4*, 941-946.

12. Yaguchi, T.; Lee, S.; Choi, W. S.; Kim, D.; Kim, T.; Mitchell, R. J.; Takayama, S., Micropatterning Bacterial Suspensions Using Aqueous Two Phase Systems. *Analyst* **2010,** *135*, 2848-2852.

13. Tavana, H.; Kaylan, K.; Bersano,ÄêBegey, T.; Luker, K. E.; Luker, G. D.; Takayama, S., Rehydration of Polymeric, Aqueous, Biphasic System Facilitates High Throughput Cell Exclusion Patterning for Cell Migration Studies. *Adv. Funct. Mater.* **2011,** *21*, 2920-2926.

14. Tavana, H.; Jovic, A.; Mosadegh, B.; Lee, Q.; Liu, X.; Luker, K.; Luker, G.; Weiss, S.; Takayama, S., Nanoliter Liquid Patterning in Aqueous Environments for Spatially-Defined Reagent Delivery to Mammalian Cells. *Nat. Mater.* **2009,** *8*, 736-741.

15. Tavana, H.; Mosadegh, B.; Takayama, S., Polymeric Aqueous Biphasic Systems for Non-Contact Cell Printing on Cells: Engineering Heterocellular Embryonic Stem Cell Niches. *Adv. Mater.* **2010,** *22*, 2628-2631.

16. Caruso, F.; Rodda, E.; Furlong, D. N.; Niikura, K.; Okahata, Y., Quartz Crystal Microbalance Study of DNA Immobilization and Hybridization for Nucleic Acid Sensor Development. *Anal. Chem.* **1997,** *69*, 2043-2049.

17. Fischer, M. J. E., Amine Coupling through EDC/NHS: a Practical Approach. *Methods Mol. Biol* **2010,** *627*, 55-73.

18. Lee, N. Y.; Chung, B. H., Novel Poly (dimethylsiloxane) Bonding Strategy via Room Temperature ,"Chemical Gluing". *Langmuir* **2009,** *25*, 3861-3866.

19. Jameson, D. M.; Wong, S. S., *Chemistry of Protein and Nucleic Acid Cross-Linking and Conjugation*. 2nd ed.; CRC Press: 2011.

20. Zhou, J.; Ellis, A. V.; Voelcker, N. H., Recent Developments in PDMS Surface Modification for Microfluidic Devices. *Electrophoresis* **2009,** *31*, 2-16.

21. Okahata, Y.; Kawase, M.; Niikura, K.; Ohtake, F.; Furusawa, H.; Ebara, Y., Kinetic Measurements of DNA Hybridization on an Oligonucleotide-Immobilized 27-MHz Quartz Crystal Microbalance. *Anal. Chem.* **1998,** *70*, 1288-1296.

22. Khorasani, M.; Mirzadeh, H.; Kermani, Z., Wettability of Porous Polydimethylsiloxane Surface: Morphology Study. *Appl. Surf. Sci.* **2005,** *242*, 339-345.

23. Pinto, S.; Alves, P.; Matos, C.; Santos, A.; Rodrigues, L.; Teixeira, J.; Gil, M., Poly (dimethyl siloxane) Surface Modification by Low Pressure Plasma to Improve Its Characteristics towards Biomedical Applications. *Colloids Surf., B* **2010,** *81*, 20-26.

24. Adamson, A. W.; Gast, A. P., *Physical Chemistry of Surfaces*. 6th ed.; John Wiley & Sons, Inc.: 1997.

25. Brochard, F., Motions of Droplets on Solid Surfaces Induced by Chemical or Thermal Gradients. *Langmuir* **1989,** *5*, 432-438.

26. Subramanian, R. S.; Moumen, N.; McLaughlin, J. B., Motion of a Drop on a Solid Surface Due to a Wettability Gradient. *Langmuir* **2005,** *21*, 11844-11849.

27. Chaudhury, M. K.; Whitesides, G. M., How to Make Water Run Uphill. *Science* **1992,** *256*, 1539-1541.

28. Nadkarni, G.; Garoff, S., An Investigation of Microscopic Aspects of Contact Angle Hysteresis: Pinning of the Contact Line on a Single Defect. *Europhys. Lett.* **2007,** *20*, 523.

29. Murakami, D.; Jinnai, H.; Takahara, A., Wetting transition from the Cassie–Baxter state to the Wenzel state on textured polymer surfaces. *Langmuir* **2014,** *30*, 2061-2067.

30. Alberts, B.; Johnson, A.; Lewis, J.; Raff, M.; Roberts, K.; Walter, P., *Molecular Biology of the Cell*. 5th ed.; Garland Science: 2012.

Chapter 3

Surface-templated hydrogel patterns prompt matrix-dependent migration of breast cancer cells towards chemokine-secreting cells

This chapter describes a novel technique to fabricate spatially-defined cell-laden collagen hydrogels, using patterned, non-adhesive polyacrylamide-coated polydimethylsiloxane (PDMS) surfaces as a template. Precisely patterned embedded co-cultures of breast cancer cells and chemokine-producing cells generated with this technique, revealed matrix- and chemokine isoform-dependent migration of cancer cells. CXCL12 chemokine-secreting cells induce significantly more chemotaxis of cancer cells when the 3D extracellular matrix includes components that bind the secreted CXCL12 chemokines. Experimental observations using cells that secrete CXCL12 isoforms with different matrix affinities together with computational simulations show that stronger ligand-matrix interactions sharpen chemoattractant gradients, leading to increased chemotaxis of the CXCL12 gradient-sensing CXCR4 receptor-expressing (CXCR4+) cells patterned in the hydrogel. These results extend our recent report on CXCL12 isoform-dependent chemotaxis studies from 2D to 3D environments and additionally reveal the important role of extracellular matrix composition. The developed technology is simple, versatile and robust; and as chemoattractant-matrix interactions are common, the methods described here should be broadly applicable for study of physiological migration of many different cell types in response to a variety of chemoattractants.

3.1 Introduction

Gradient formation and sensing is a complicated process involved in many physiologic and pathologic processes. Cells will change morphology and move toward a chemical gradient depending on the shape, dynamics, and magnitude of the gradient.[1] The simplest model of gradient formation involves diffusion of soluble factors away from cells that secrete them. However, *in vivo* there are two types of microenvironmental interactions that define gradient formation and sensing: ligand-matrix, and ligand-cell. Several studies have demonstrated the importance of complex gradient shape and dynamics *in vivo*, driven by ligand-matrix interactions[2, 3] and by active cell-dependent ligand scavenging.[4] Hence, to properly model and experimentally manipulate these complex chemotactic processes, we need experimental systems that recreate these environmental influences on gradient formation.

Here we develop a technique that enables robust and versatile definition of *in vitro* multi-cellular / microenvironment interactions, in physiologically-relevant 3D environments, and utilize this technique to study the relationship between ligand-matrix and ligand-cell interactions on migration of breast cancer cells. A few *in vitro* assays exist to recreate how ligand-matrix and ligand-cell interactions collectively guide gradient formation. Transwells,[5] hydrogels,[6-10] and microchannels,[11-16] are typically used to spatially pattern cells, define morphogenetic and chemotactic gradients, and monitor cell morphology and chemotaxis. Although these assays isolate individual aspects of gradient formation and sensing, they fail to replicate how multiple cell types and matrix interactions together define a gradient.

We previously developed an experimental source-sink system to replicate the formation of defined soluble gradients between spatially-patterned cells that secrete ligands (source) and cells that scavenge ligands (sink).[17, 18] These previous studies capture the involvement of multiple cell types in source-sink gradient formation and the role of ligand binding to the device- and cell-surfaces. However, the relatively small surface area with limited amount of binding sites available in this simple two-dimensional assay is not sufficient to address the potential influence of ligand-matrix interactions, as compared to the *in vivo* situation in which 3D matrices provide a significantly greater concentration of binding sites.

In this work, we develop a novel patterning system to spatially pattern cells within an extracellular matrix (ECM), creating a model tissue-like environment for studies of directional cell migration. There are several techniques to create desired hydrogel patterns, such as laser lithography[19-25] and microchannel-guides,[26-28] that often require significant expertise, specialized instruments and complicated processing. Our approach enables the precise positioning of multiple cell types within a 3D matrix, using relatively simple tools and expertise that should be accessible to most wet-labs. As a first application of this technology, we spatially pattern cells engineered to secrete the α- and β- isoforms of the CXCL12 chemokine and CXCR4+ cells that respond to CXCL12, while varying the composition of the surrounding matrix. Using this breast cancer model system, we demonstrate (1) the ability to systematically control ligand-matrix interactions via matrix composition; (2) the ability to spatially pattern multiple interacting cell types within a 3D matrix; and (3) the effects of ligand-matrix interactions on gradient formation, and on subsequent cell migration.

3.2 Materials and Methods

Unless otherwise stated, all chemicals and reagents for cell culture were purchased from Sigma-Aldrich, fluorescent dyes from Invitrogen and all other equipment and materials from Fisher Scientific.

3.2.1 Cell culture

MDA-MB-231 (231, ATCC) cells were primarily used for these experiments, and were cultured in fully supplemented Dulbecco's Modified Eagle Medium (DMEM, with 10% Fetal Bovine Serum (FBS), 1% antibiotics-antimycotics). Some demonstration experiments were conducted with NIH 3T3 murine fibroblasts (cultured in fully supplemented DMEM), and human bone marrow endothelial cells (HBMECs, were a gift from Irma de Jong, cultured in fully supplemented Endothelial Cell Growth media, EGM2, with 5% FBS; Lonza). Standard trypsinization-based sub-culture protocols were used to passage cells prior to the experiment. We previously described culture, lentiviral transduction, and migration of 231 cells expressing CXCR4 towards 231 cells secreting CXCL12.[17, 18] Briefly, we transduced 231 cells sequentially with a CXCR4-GFP fusion[29] and NLS-AcGFP to facilitate receptor-based migration and image-based tracking of nuclei,[18] respectively. We expressed CXCL12-isoforms fused to *Gaussia* luciferase (GL) upstream of the fluorescent protein mCherry in a pLVX IRES vector, to facilitate proportional fluorescence sorting for CXCL12-expressing cells.[18]

3.2.2 Preparation of PAA-coated PDMS surface

10:1 (w/w) degassed mixture of PDMS and a curing agent were diluted with toluene (PDMS:toluene = 1:3). 12 mm diameter glass slides were dipped into the mixed solution and baked at 120 °C for 30 min. 9:1 (v/v) mixture of prepolymer solution (18.9 w/w% acrylamide, 0.33 w/w% pluronic F108, and 80.77 w/w% water) and photoinitiator solution (0.3 w/w% benzophenone and 99.7 w/w% 2-propanol) were added to the PDMS-coated slides and polymerized under UV (CL-1000, UVP: 8W x 4min) followed by an extensive wash in water.[30, 31] The PAA-coated PDMS slides were stored at ambient conditions and used for following hydrogel patterning within a few days (Figure 3.1A).

3.2.3 Fabrication of oxidized patterns

The SU-8 master molds were fabricated by soft lithography. Detailed procedure for fabrication of master molds can be found elsewhere.[32] The PDMS replicas of patterns served as oxidation stencils were placed in conformal contact with the PAA-coated PDMS slides and oxidized (100W x 10 min).[33] Oxidized PAA-coated PDMS slides were immediately used for hydrogel patterning (Figure 3.1B).

3.2.4 Surface characterization

Water contact angles in air were measured on PDMS-coated slides and PAA-coated PDMS slides before and after oxidation by the sessile drop technique (4 μL of water) using a goniometer and analyzed with ImageJ. Data are expressed as a mean ± standard deviation (n = 3). Surface topography of PAA-coated PDMS slides oxidized through patterns was measured by atomic force microscope in ScanAsyst mode (Veeco, Bruker) and analyzed with Nanoscope (Veeco, Bruker).

3.2.5 Hydrogel patterning

2 mL of degassed PDMS was poured and cured into each well of a 6-well plate (Figure 3.1C). Each PDMS well was punched along the shape of a 12 mm glass slide and each oxidized PAA-coated PDMS slide was set at the bottom of the well. Trypsinized cells were mixed with neutralized type I bovine collagen (BD Biosciences) to create a suspension of 10 million cells / mL in 2 mg/mL of collagen.

For cell-free experiments, 1 μm diameter fluorescent beads (Sigma) were added to the neutralized collagen solution. 6 μL of the collagen gel solution was dispensed over each adhesive pattern and allowed to polymerize for 45 min in a humidified cell incubator (37 °C, 5% CO2). 250 μL of either 2.5 mg/mL neutralized collagen or 2.5 mg/mL neutralized collagen supplemented with growth factor reduced matrigel (BD Biosciences: 61% laminin, 30% collagen IV, 7% entacin, and 2% other proteins including proteoglycans) mixture of collagen gel and matrigel solutions (75v/v% collagen I + 25v/v% marigel) was poured on each well and allowed to polymerize for 1 hour in the humidified incubator. 2 mL of cell culture media were added to each well and cultured at 37 °C. For observation of non-specific cellular movement, Latrunculin (10μM) was added to the media in control samples to prevent actin polymerization and hence migration.

3.2.6 Cell adhesion test

DMEM cell culture media containing MDA-MB-231 cells was cultured on tissue culture plastic, PAA-coated PDMS or oxidized PAA-coated PDMS slides in a 24-well plate and incubated for 24 hours. Cell culture media was aspirated and samples were rinsed twice in PBS. 1 mL of 4% paraformaldehyde solution was added to fix cells. Cellular actin cytoskeletal structures and the cell nucleus were labeled with Phalloidin and Hoechst dyes, following protocols obtained from the manufacturers. Images were collected with an epifluorescent microscope (TE-300, Nikon) and analyzed with ImageJ to determine cell density and spread area, expressed as a mean ± standard deviation ($n = 6$).

3.2.7 Modeling diffusion and binding kinetics

Finite element modelling of the diffusion and binding kinetics were conducted in COMSOL 4.2 (Burlington, MA), using a 1-D model geometry. Parameters for diffusion of CXCL12 (MW ≈ 10 kDa) were estimated based on the Stokes-Einstein equation relating hydrodynamic radius with diffusion rate, and published values in the literature for diffusion of large molecules in collagen.[34] Flux of CXCL12 molecules at one end of the model was calculated based on the estimated rate of CXCL12 production by cells[18] and on the geometry of the hydrogel system. A reaction-diffusion COMSOL module was used to simulate binding of the secreted soluble factors to uniformly distributed binding sites, representing matrigel proteoglycans in the collagen matrix. Kinetic binding parameters of CXCL12-α and CXCL12-β to matrigel proteoglycans were estimated as being similar to the binding kinetics of CXCL12 isoforms to heparan sulfate.[35] Results are reported as concentrations of soluble factors and as specific gradients across the length-scale of an individual cell. The specific gradient was determined by dividing the concentration difference across 50 μm by the average concentration over that distance.[17]

3.2.8 Binding assay of CXCL12 to different matrix coatings

We previously described and characterized the production and activity of CXCL12-isoforms fused to *Gaussia* luciferase.[18] Measurement of *Gaussia* luciferase activity allows quantitative measurements of CXCL12 associated with cells, bound to extracellular matrix, and in cell culture supernatants. We collected supernatants from 10^6 cells expressing secreted GL, CXCL12-α-GL, CXCL12-β-GL, or GL-negative that were plated in 60 mm dishes. After cells adhered in 10% FBS DMEM media overnight, cells were washed once in PBS, and media was replenished with DMEM with 0.2% albumin (Probumin Media Grade, Millipore). After 24 hours the supernatants were collected and imaged for GL activity and diluted in GL-negative cell supernatants to normalize GL flux activity to that of the lowest condition.

Briefly, to measure GL flux, 1 µl of supernatant was queried in 1:1000 final dilution of the GL-substrate coelanterazine brought to a total volume of 100 µl of PBS, as we have described previously.[18] We added 50 µl of the GL flux-normalized supernatants to 96 well tissue culture plates that were pretreated with extracellular matrix (collagen, collagen and matrigel, matrigel only, or untreated tissue culture). Pre-treatment was achieved by incubating the 96 well plate with the appropriate solutions at 4 °C for 2 hours.

The low temperature prevented polymerization but allowed adsorption of both collagen and matrigel components. Wells were then washed twice with PBS. Wells were grouped in quadruplicate for each supernatant type and extracellular matrix (ECM) type for three independent experimental setups. We incubated these plates for 30 minutes at 37°C to facilitate binding to the ECM. To remove unbound GL-species, we aspirated medium; washed each well in triplicate with an excess of PBS; and replaced medium with 50 µl of PBS per well. We imaged each well with the same substrate and PBS volumes as above. All bioluminescence images were acquired with the IVIS Lumina Series III (Caliper, LifeSciences), and data were analyzed with Living Image 4.3.1

3.2.9 Chemotaxisis of MDA-MB-231 cells

CXCR4+ and source cells (secreted GL as GL, CXCL12-α-GL as CXCL12-a, and CXCL12-β-GL as CXCL12-b) in mixture of collagen and matrigel matrix with 2 mL DMEM media were incubated for 24 hours and imaged with a fluorescent microscope (TE-300, Nikon). The representative leading cell-to-cell distance at day 0 and day 1 were each measured at five points with ImageJ and expressed as a mean ± standard deviation (n = 6 for GL, n = 6 for CXCL12-a, n = 6 for CXCL12-b, each in the presence of matrigel, n = 5 for CXCL12-b in the absence of matrigel).

3.2.10 Statistical analysis

All statistics are reported as means ± standard deviation. ANOVA tests were performed using a commercially-available software package (SigmaStat 3.5; Systat Software Inc., San Jose, CA), using the Tukey test for post-hoc pairwise comparisons.

3.3 Results

3.3.1 Characterization of hydrogel patterns on PAA-coated PDMS

This system enables control of three parameters: spacing between groups of patterned cells, gel composition, and cell type (Figure 3.1). PAA-coated PDMS slides were fabricated as described (Figure 3.1A-C) and clusters of cells encapsulated in hydrogels were patterned adjacent to each other with defined spacing (Figure 3.1D and Figure 3.7). The pattern-to-pattern distance was controllable and hydrogel patterns were stable regardless of cell type and gel composition. Obtaining successful patterns depends on carefully balancing topographic and surface chemistry features of the patterned surface template, at the contact line between the hydrogel precursor solution and the underlying substrate.

Surface chemical heterogeneity and physical topology are both known to define the contact line at liquid-solid and liquid-liquid interface.[32, 36] We characterized the surface properties of PAA-coated PDMS by measuring the contact angle of sessile droplets, and AFM topographical measurements. The contact angle measurement of native PDMS and PAA-coated PDMS illustrates a dramatic reduction of contact angle before and after plasma oxidation (Figure 3.2A). While intact PAA-coated PDMS showed lower contact angle compared to native PDMS due to the hydrophilic nature of PAA introduced on PDMS, both surfaces demonstrated similar contact angles after oxidation.

Meanwhile, AFM measurement reveals distinct surface topology of patterned PAA-coated PDMS (Figure 3.2B). A clear boundary at the edge of the pattern was observed and the step was about 50 nm at the boundary. In contrast, there was no distinct difference between intact and oxidized PAA-coated PDMS regions (Figure 3.8). We confirmed that either reducing oxidation time or leaving substrates for a few days resulted in failure of hydrogel patterning (data not shown), indicating that both surface chemistry and physical topography boundaries are necessary to support the formation of stable hydrogel patterns. We note that the accuracy of the patterning with 250 µm spacing was 246 ± 4.97 µm (n = 3) and the height of a droplet was 0.76 ± 0.041 mm (n = 6). We examined the limitations where the minimum spacing is 100 µm and minimum size of a pattern is 1.5 mm in diameter. Below these dimensions, oxidation and surface treatment did not work properly and failed to sustain the droplet shape.

In addition to the ability to precisely pattern hydrogels, PAA serves as a non-adhesive cell-repellent material,[37] and prevents migration of the cells over the PAA surface. To confirm this, the number of cells adhered to these surfaces were assessed using a standard cell-adhesion test, and indicates that adhesion was virtually eliminated, as compared to tissue culture plastic surfaces. Furthermore, cell spread area was also greatly reduced for the few adherent cells (Figure 3.2C-G), indicating that cells cannot attach sufficiently to spread, and therefore migrate. Cell adhesion and spreading were restored after oxidation of the PAA surface, but as this occurs only within the regions of patterned cells and not in the region of migration between cell patterns, these effects can be ignored in this migration assay. Hence, migrating cells are forced to interact with the hydrogel matrix.

3.3.2 Migration rates depend on matrix composition and CXCL12 production

We first confirmed that cells could migrate through the patterned matrix by monitoring radial movement of MBA-231 cells initially patterned in a single spot (Figure 3.9A). Radial dispersion of cells can be attributed to both random movement and growth of 231 cells (~24 hour doubling time). To confirm that soluble factors can be transported through the matrix, the cytoskeletal disruption compound Latrunculin A was added to the culture and significantly suppressed radial migration (Figure 3.9A-C). Confocal images of GL cells in collagen gel matrix at day3 indicates most of the cells settled down on the surface with a 15 μm-thick cell layer in the presence of latruncurin while the cells radially migrated through the gel matrix without latruncurin (data not shown). We seeded 6 x 10^4 cells / hydrogel-droplet in theory and, based on confocal imaging, confirmed that over 99% (> 5.9 x 10^4) of the cells settled down on the surface at t = 0. We also observed the same trend for other cell types used in this work. It indicates that the observed cell migration did not arise from the randomly distributed suspended cells in hydrogels. Thus we assume that most cells settled down on the surface at t=0 whereas they start to migrate in 3D over the course of time.

Next, to examine effects of cell-matrix and ligand-matrix interactions on cell migration in hydrogel matrices, we patterned encapsulated CXCR4+ migrating cells adjacent to cells that secrete its ligand, CXCL12-β, which we express as a fusion to *Gaussia* luciferase (GL). CXCL12-β cells were used because the cells secrete the most chemokine compared to other CXCL12-isoforms.[18] In control experiments, we replaced the CXCL12-β source cells with cells secreting GL unfused to a chemokine, which does not bind to CXCR4 or regulate signaling through this receptor. To assess migration in this system, we measured the gap spacing between the leading edge of the migrating and source cell populations after 24 hours and report the measured gap closure as the migration distance (Figure 3.3A and B). CXCL12-β drove more rapid migration than the GL control in the presence of matrigel. Without matrigel, migration rate was non-significant for CXCL12-β as compared to the GL control. This suggests that gradient generation and/or sensing of CXCL12-β requires interactions between CXCL12 and matrigel components (Figure 3.3C).

3.3.3 Matrix binding generates steep CXCL12 gradients

We hypothesized that matrigel provides binding sites for CXCL12 factors, which influences the formation of both soluble and bound gradients in the matrix. To evaluate the potential contribution of ligand-matrix interactions in shaping the gradient, we used computational models to simulate diffusion and diffusion with a matrix-binding component. In the diffusion model, unbound CXCL12-β rapidly diffuses through the gel matrix, and generates a negligible specific gradient to stimulate cell migration (Figure 3.4A). In contrast, ligand-matrix binding generates a steep specific gradient of unbound CXCL12-β, albeit at lower concentrations (Figure 3.4B). Bound gradients may have similar profiles, but cannot precede the soluble gradient as diffusion across surfaces is well-established to be significantly less than diffusion through an aqueous medium. These simulation results strongly indicate that interactions between the ligand and matrix facilitates gradient shaping and presents a possible mechanism explaining the matrix-dependent migratory differences observed in our chemotaxis experiments.

Additionally, our model suggests that when cell clusters are spaced more than 500 μm apart, chemotaxis cannot occur within the 24 hour time-frame of the experiment, as steep gradients cannot form across large distances rapidly enough. To confirm the importance of this spacing, we doubled the spacing to 500 μm, and observed no significant migratory differences prompted by GL-secreting cells and CXCL12-expressing cells in 24 hours (Figure 3.10). Hence, the ability of our technique to position the cell clusters close to each other is crucial parameter in observing these gradient-driven migratory responses.

3.3.4 Differential binding of CXCL12 isoforms to matrix components

To better understand the ligand-matrix interactions, we assessed the relative binding of CXCL12-isoforms to various matrix components. We used *Gaussia* luciferase activity to measure the relative binding of secreted GL or CXCL12-α and CXCL12-β fused to GL to wells coated with collagen I alone, collagen I-matrigel mixture, and matrigel alone (Figure 3.5A). Note that this measurement was conducted on the hydrogel-coated 2D well surface in contrast to other measurements in 3D hydrogel system.

Collagen by itself provided no differential binding across all secreted factors (Figure 3.5B). However supplemented matrigel in collagen I caused a rank-order increase in binding, in which GL < CXCL12-α < CXCL12-β. Differential binding was statistically higher with matrigel by itself as compared to collagen only and the collagen-matrigel mixture. These findings suggest that matrigel increases capacity for CXCL12 binding and indicate that ligand-matrix interactions can be a dominant factor in shaping chemotactic gradients of CXCL12 isoforms. Furthermore, this suggests that matrix-binding may provide a mechanism by which migration of CXCR4 cells in response to different CXCL12-isoforms may be altered.

3.3.5 Gradients of CXCL12 isoforms affect migration rate

To further explore the hypothesis that matrix-binding effects generate migration-inducing gradients, we compared the migration behavior in response to GL, CXCL12-α and CXCL12-β in the presence of matrigel (Figure 3.6A). We observed significant differences in migration associated with these secreted factors, in which the migration rate order is GL < CXCL12-α < CXCL12-β. These results are consistent with the results from the binding assay of these molecules to matrigel presented in section 3.2.8 and 3.3.4.

Simulations of gradient formation in the diffusive matrix-binding model revealed distinct gradient dynamics for CXCL12 isoforms, based on the secretion rate and binding kinetics of the isoforms (Figure 3.11). These simulations indicate that CXCR4-β gradients establish out from the source more rapidly than CXCR4-α gradients (Figure 3.6B and C). Hence, in a relatively short-term experiment, migratory cells are exposed to chemotaxis-inducing gradients for different time periods, which likely explains the differences in migration observed between α and β isoforms. While there may also be other effects of adding matrigel, such as altered gel morphology or additional macromolecular crowding effects, taken together, our findings strongly suggest that our model system is able to adequately explore the parameters involved in matrix-sequestering gradient generation effects.

3.4 Discussion

We developed a novel patterning technique that exploits surface heterogeneity and cell-repellent properties to precisely pattern hydrogels for studies of gradient formation and cell migration. This system presents two core advantages over existing technologies for patterning cells: 1) broad applicability to a variety of ECM compositions and cell types; and 2) facile patterning of multiple cell types in defined geometric locations. We leverage our ability to pattern cell-laden hydrogels of varying composition to determine that formation of gradients of CXCL12 isoforms critically depends on ECM molecules for migration of CXCR4+ cells.

Our technology for patterning hydrogels relies on a simple surface patterning technology that biases cells and ligands towards interactions with the hydrogel matrix rather than the rigid substrate. By controlling relative surface energies between oxidized and native PAA-functionalized PDMS, we create geometrically-defined hydrogel patterns while minimizing cell interactions with the solid substrate. This patterning technique is simpler than channel-based or laser lithography-based hydrogel patterning systems and provides more robust patterns than liquid-liquid patterning techniques, such as aqueous two-phase systems.[32, 38] Simple but robust hydrogel patterning with our system decreases the barrier for adoption of 3D assays and improves their flexibility for researchers. Moreover, given the biased interaction among patterned cells, their secreted factors, and the hydrogel ECM, our system facilitates studies of the role of matrix interactions in physiological settings.

Dysregulated composition and architecture of the extracellular matrix is a fundamental hallmark of cancer. Perturbations in the extracellular matrix increase stiffness of the environment, facilitate invasion of cancer cells along collagen fibrils, and enhance tumor growth.[39] Less recognized is that changes in ECM content in tumors augments the capacity of the microenvironment to sequester growth factors in a way that increases local concentrations and establishes chemotactic gradients in pancreatic[40] and breast cancers.[41, 42] For example, heparan sulfate proteoglycans in tumors binds CXCL12 and other soluble chemokines to create a chemotactic gradient that directs cell migration.[43, 44] Our device enables facile control of extracellular matrix environments to study how interactions between chemotactic molecules and extracellular matrix molecules regulates magnitude of chemokine gradients and resultant cell migration.

As a prime example of the interplay among migrating cells, cells secreting chemokines, and different ECM, we investigated migration of CXCR4+ cells towards gradients of different CXCL12-isoforms. We modulated the interaction between the CXCL12 and the ECM by incorporating matrigel and expressing CXCL12 isoforms with different affinities for matrigel. CXCL12-β, which has a higher affinity for matrigel than the α-isoform (Figure 3.5), drove substantially higher migration of CXCR4+ cells. Our 3D hydrogel system revealed another nuance of the source-sink model where CXCL12 gradient formation and sensing does not require CXCL12 scavenging by receptor CXCR7 as previously reported.[4, 5, 18, 45] We found that for some CXCL12-isoforms, binding to the ECM may effectively form a gradient instead of CXCR7 ligand scavenging cells. Our system demonstrates how chemotactic phenotypes evolve differently among cell types in hydrogels and may better recreate *in vivo* physiology.

To further investigate effects of different ligand-matrix interactions on gradient dynamics, we developed a simple computational model of ligand diffusion away from cells secreting CXCL12 isoforms and binding to the ECM. Owing to precisely patterned hydrogel matrix in 3D and the large capacity for CXCL12 binding in the ECM, our computation and experimental model indicates that ligand-matrix interactions replace the cell-scavenging sink required in the previous 2D assay. It should be noted that we cannot decouple the individual contribution of bound and free CXCL12 gradients, which is a limitation of this study. We assume that the combination of bound and unbound gradients of CXCL12 drive CXCR4+ migration (haptotaxis and chemotaxis, respectively). In the future work, bound gradients of CXCL12 can be generated in the hydrogel matrix to selectively assess CXCL12-dependent haptotaxis of CXCR4+ cells. This can be achieved through the use of 3D ECM engineering techniques to tether gradients of molecules to the matrix.[46-49]

Our system's flexibility extends to many different biological questions of how multicellular interactions in 3D environments determine movement and morphogenesis, such as in angiogenesis,[50, 51] metastasis,[52] and other processes[53] that require multiple patterns and cell populations. Here we use our system to analyze a tumor microenvironment to allow cell-autonomous gradient formation and sensing of chemotactic molecules. Our results support the idea that secreted signaling molecules interact with the ECM and direct cancer cell migration. We also note that our ECM patterning technique is amenable to multiplexing for studies of interactions between more than two cell-type or matrix combinations (Figure 3.12).

3.5 Conclusions

Patterns on a non-adhesive surface can serve as a template to create patterns of cell-laden hydrogels with different gel compositions, cell types and soluble signals present. In this work, spatially patterned hydrogel matrices revealed distinct chemotactic behavior of breast cancer cells in response to production of the alpha and beta isoforms of the soluble signaling factor CXCL12. Our computational models indicate that a steep gradient of CXCL12 forms as a result of ligand-matrix binding interactions in reconstituted ECM, and predicts a lag-time in gradient advancement between the CXCL12 isoforms. Our system establishes that autologous gradient formation arises as a result of this interaction, without the presence of cells that scavenge CXCL12. More broadly, our approach presents a simple alternative to generating microstructured biomaterials for advanced migratory and morphogenetic studies that can be easily adopted in a variety of wet-lab environments.

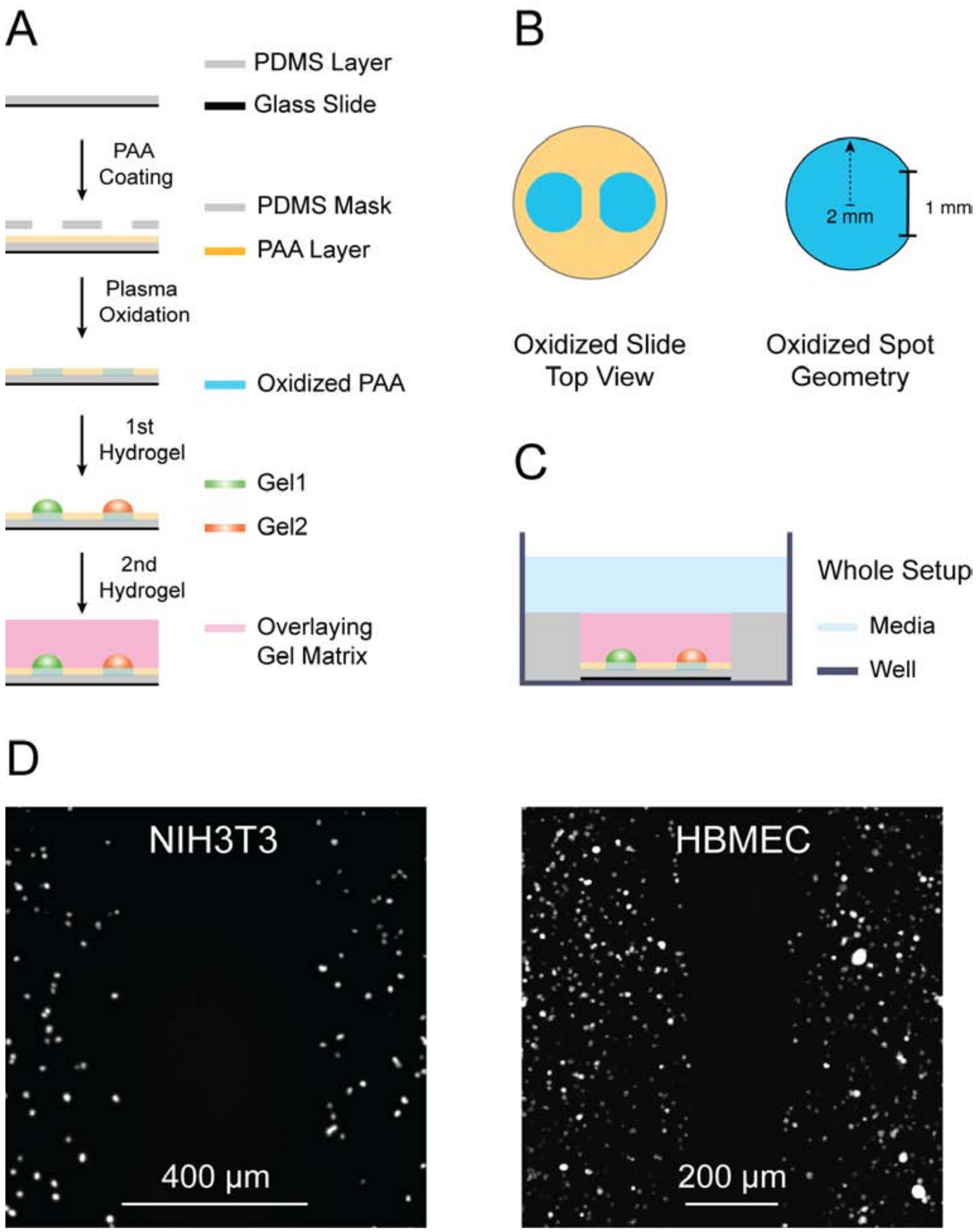

Figure 3.1. Patterning of hydrogels on a cell-repellent surface. (A) PAA was polymerized on PDMS-coated glass slides and oxidized along mask patterns. Hydrogel precursor solutions are added on oxidized regions and cured. Gel solution was overlaid the patterns and incubated for the measurement. (B) Top view illustration of a patterned slide. Whole slide 12 mm diameter and oxidized spot 4 mm diameter. (C) Side view illustration of the whole setup. (D) Fluorescent image of patterned collagen gels containing NIH3T3 cells overlaid by collagen gel with 400 µm pattern-to-pattern distance and fluorescent image of patterned collagen gels containing HBMEC cells overlaid by the mixed gel (60 v/v% matigel + 40 v/v% collagen gel) with 200 µm pattern-to-pattern distance. Scale bar 400 µm for NIH3T3 and 200 µm for HBMEC.

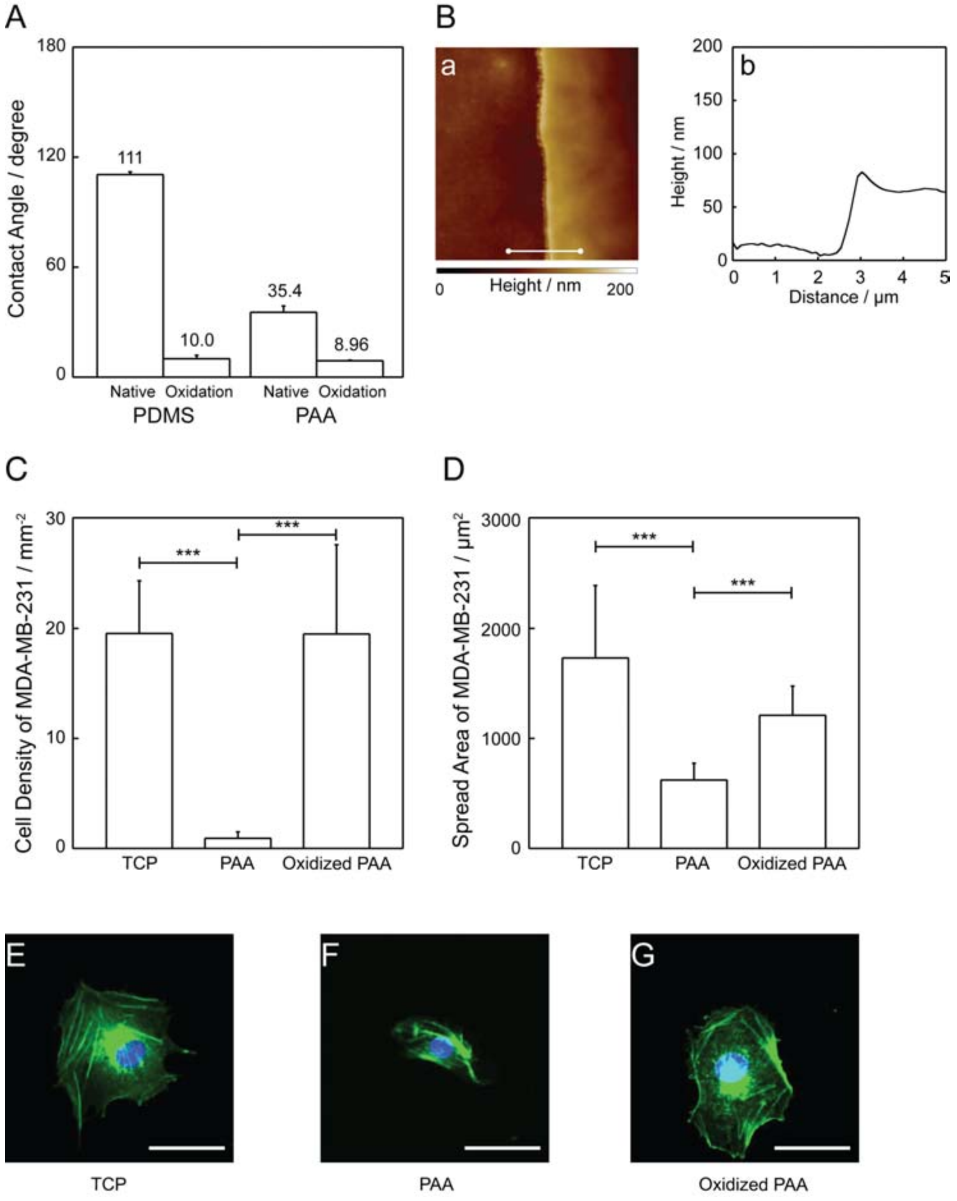

Figure 3.2. Surface characterization of PAA-coated PDMS. A) Contact angle values of water droplet on PDMS, oxidized PDMS, PAA-coated PDMS, and oxidized PAA-coated surface. (B) Surface topography of oxidized PAA-coated PDMS. (a) Height profile at the boundary and (b) highlighted section by white bar. (C-D) Cell adhesion test of MDA-MB-231 cells. (C) Cell density and (D) cell spread area of CXCL12-GL on TCP, PAA-coated PDMS, and oxidized PAA-coated PDMS. Images of a cell on (E) TCP, (F) PAA-coated PDMS, and (G) oxidized PAA-coated PDMS, respectively. Nucleus and cytosol were stained by blue and green, respectively. Scale bar 50 μm.

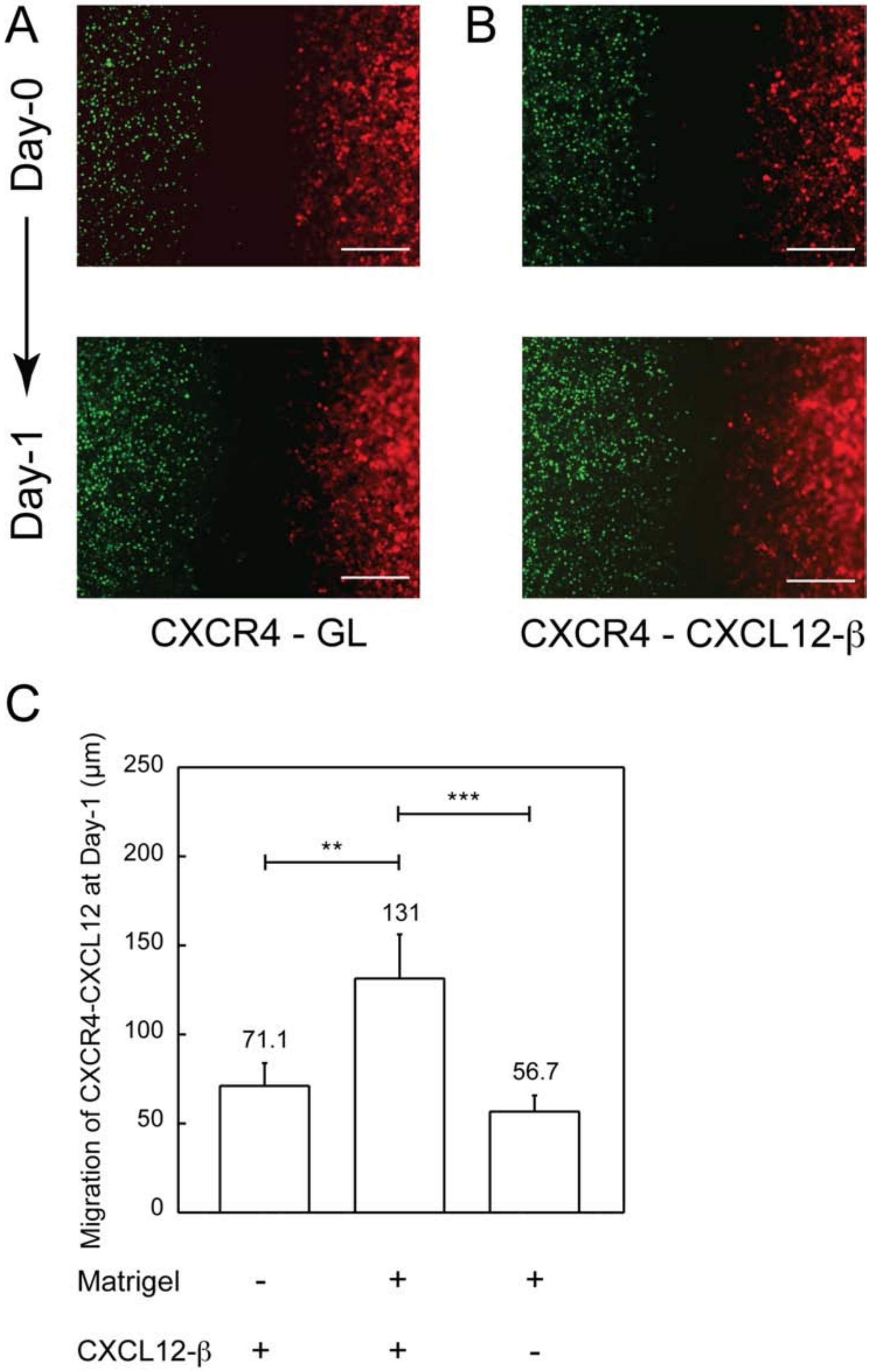

Figure 3.3. Migration assay of CXCR4 cells in 3D gel matrix. (A) Fluorescent images of CXCR4 (green) and GL (red) at day0 and day1. (B) Fluorescent images of CXCR4 (green) and CXCL12-β (red) at day0 and day1. Scale bar 250 μm. (E) Migration of CXCR4-CXCL12 at day 1 in the absence and presence of matrigel (**p <0.01 and ***p < 0.001).

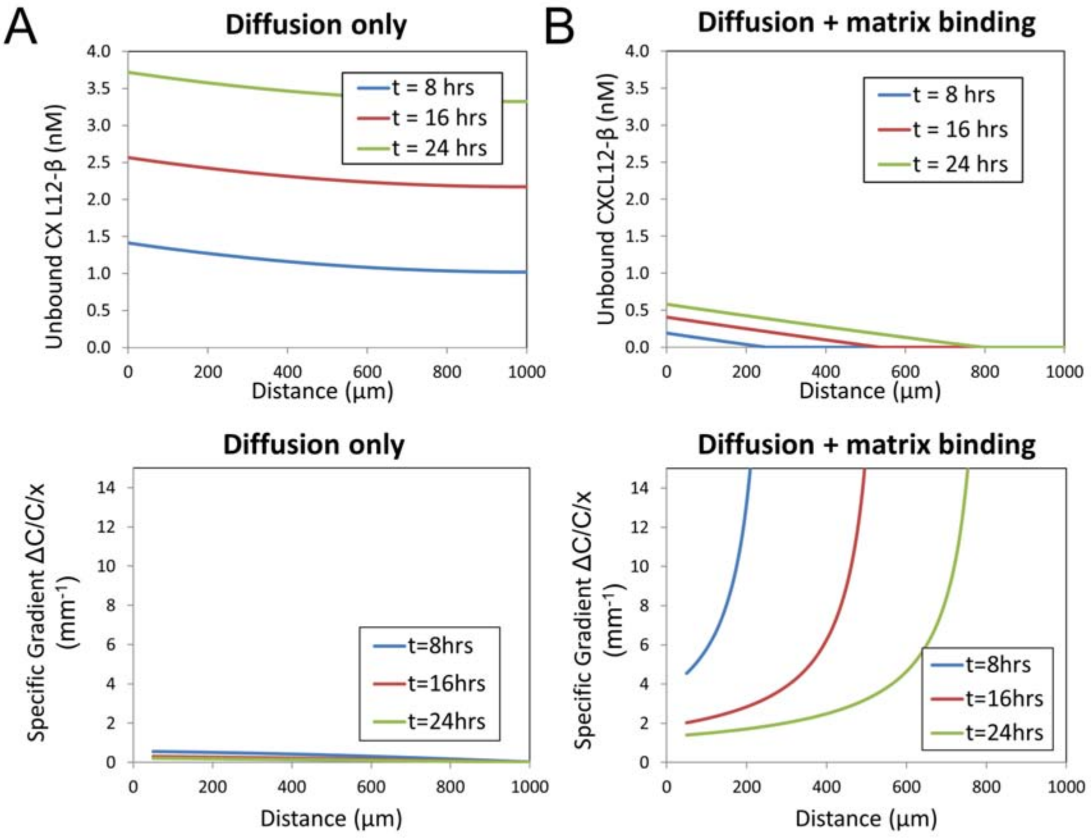

Figure 3.4. Computational modeling of CXCL12-β gradients. Simulation of unbound CXCL12-β concentration as a function of distance and time and CXCL12-β specific gradient (defined as $\Delta C / C_{avg} / x$ across a 50 µm gap) as a function of distance and time in (A) diffusion only and (B) diffusion-matrix binding.

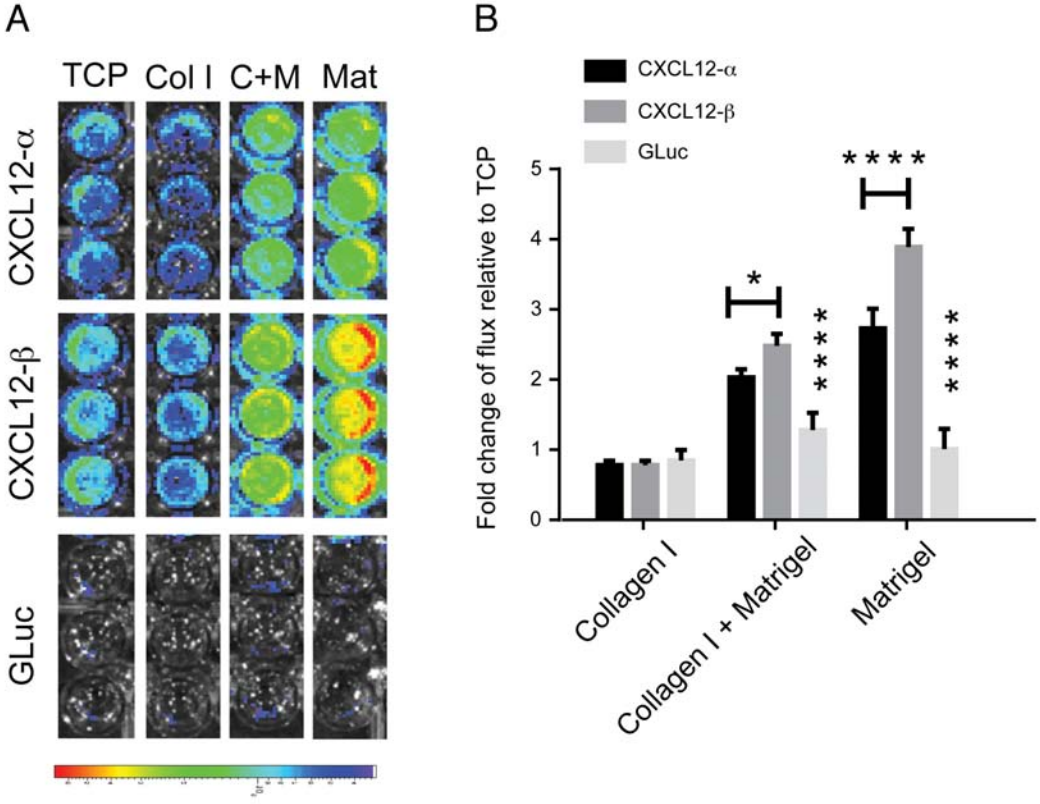

Figure 3.5. Binding assay of CXCL12 isoforms in different gel matrices. (A) Representative heat map of flux plotted on the same log. (B) Fold change of flux relative to tissue culture plastic (TCP) for CXCL12-α, CXCL12-β, and GL treated with collagen, collagen-matrigel, and matrigel. Values are plotted from one of three representative experiments as mean ± S.E.M. for quadruplicate wells. Statistical demarcations above a bar indicate pairwise comparison to all others in that group. The bar indicates individual pairwise differences (*p <0.05, **p <0.01, and ****p <0.0001).

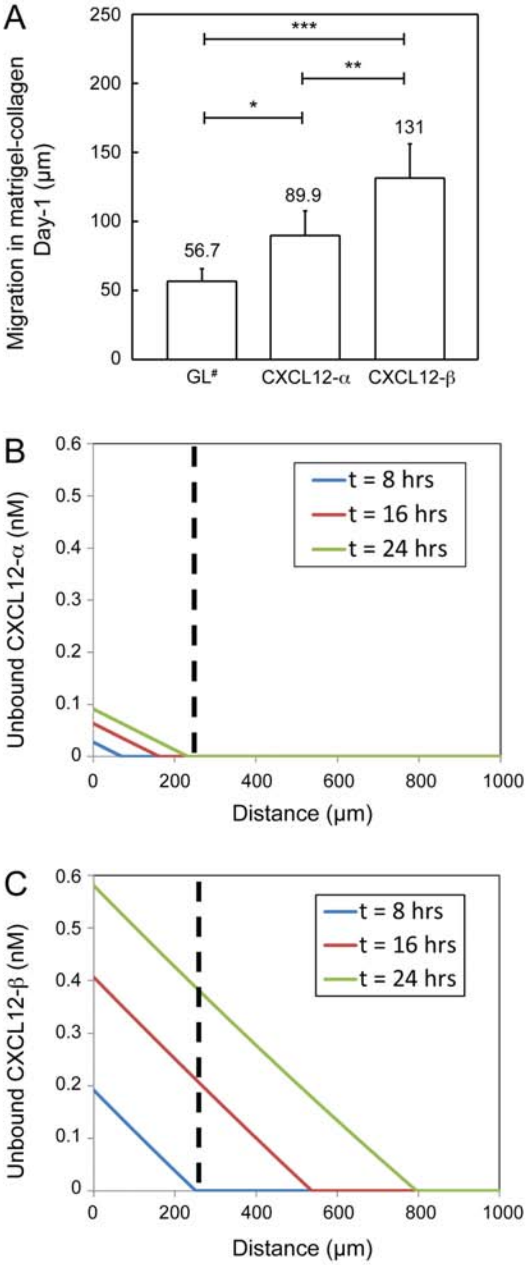

Figure 3.6. Migratory comparison of CXCL12 isoforms in the presence of matrigel. (A) Migration assay of CXCR4-CXCL12 (GL, CXCL12- α, and CXCL12-β) at day1 in the presence of matrigel with 250 μm spacing (*$p < 0.05$, **$p < 0.01$, and ***$p < 0.001$). GL$^{\#}$ represents the replication of the data in Figure 3.3C (+ matrigel / - CXCL12-β). (B-C) Computational simulation of unbound CXCL12-β and CXCL12-α gradient formation as a function of distance and time. Dotted line represents the spacing using between the patterned gels.

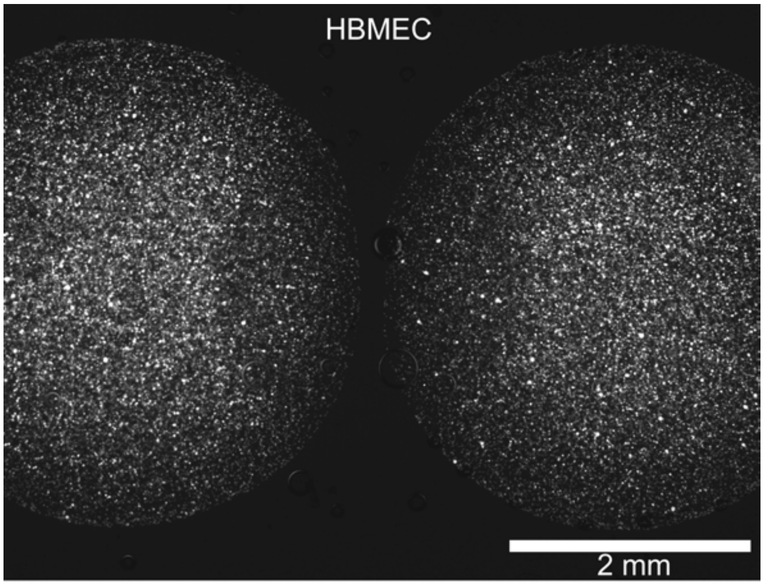

Figure 3.7. HBME cells in the patterned hydrogel droplets overlaid by matrigel with 200 µm spacing.

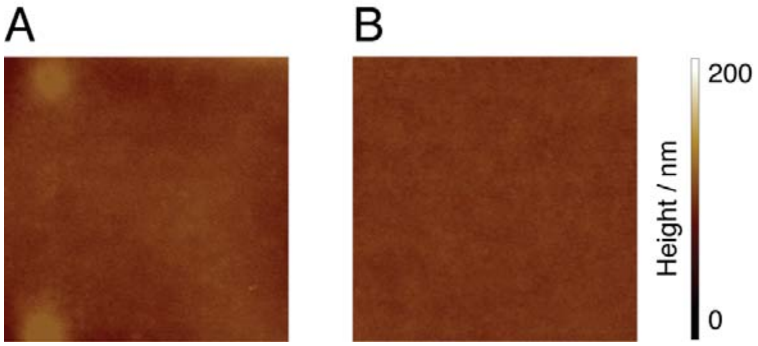

Figure 3.8. Surface topography of intact and oxidized PAA-coated PDMS. Surface height profile of (A) intact and (B) oxidized PAA-coated PDMS measured by AFM (Area 10 µm x 10 µm). Surfaces do not show significantly different topographies between the intact and oxidized regions.

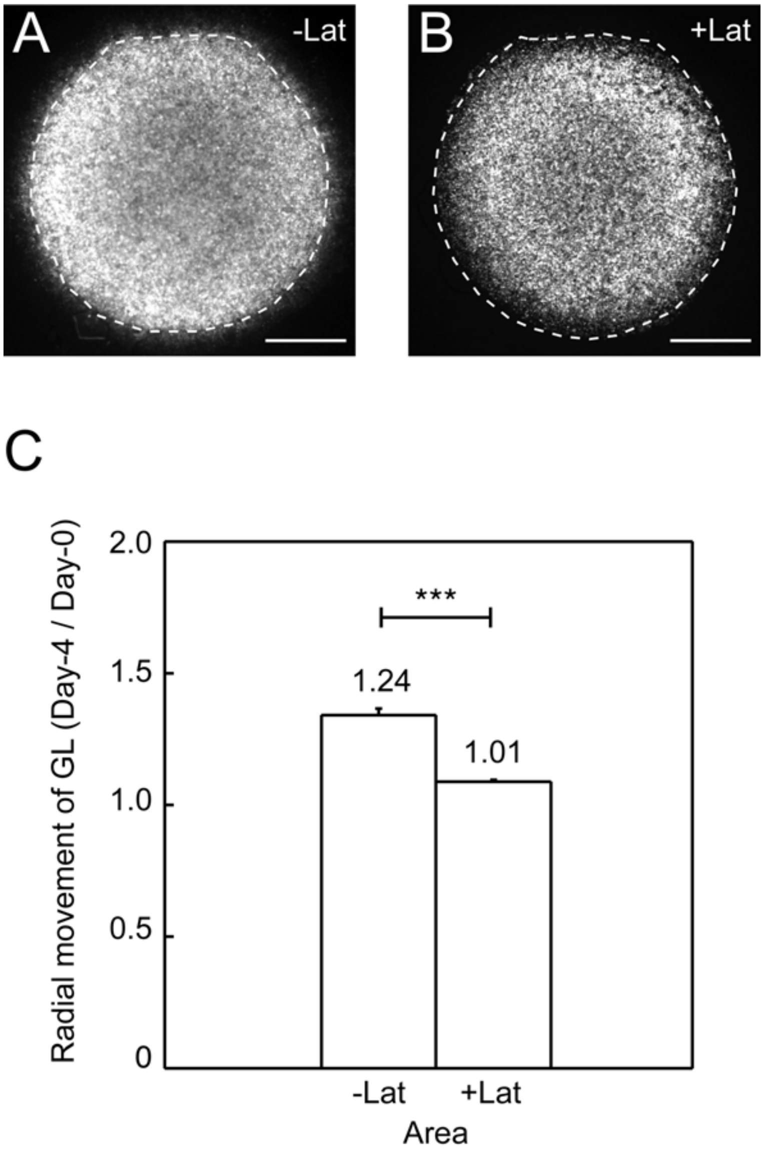

Figure 3.9. Soluble factors can be used to inhibit migration of MDA-MB-231 cells in the patterned hydrogel system. Fluorescent images of GL-expressing cells in the (A) absence and (B) presence of Latrunculin (50 μM) at day4. White dotted line represents initial cell area at day0. (C) Comparison of spread area at day 4 reveals that migration was significantly inhibited by the presence of latrunculin. Area at day4 was normalized by area at day0 (****p* <0.001). Scale bar 1 mm.

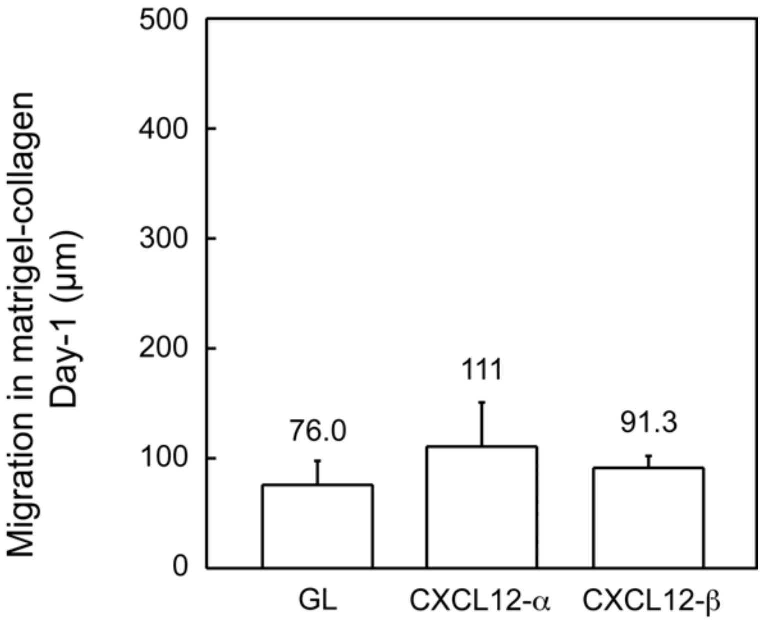

Figure 3.10. Migration assay of CXCR4-CXCL12 (GL, CXCL12- a, and CXCL12-b) at day1 within a matrigel-supplemented collagen matrix with 500 µm spacing. Migration values are expressed as a mean ± standard deviation (n = 3 for GL, n = 3 for CXCL12-a, n = 3 for CXCL12-b). In contrast to similar experiments conducted with spacings of 250 µm, no significant differences in migration were observed between the three cell types ($p > 0.35$).

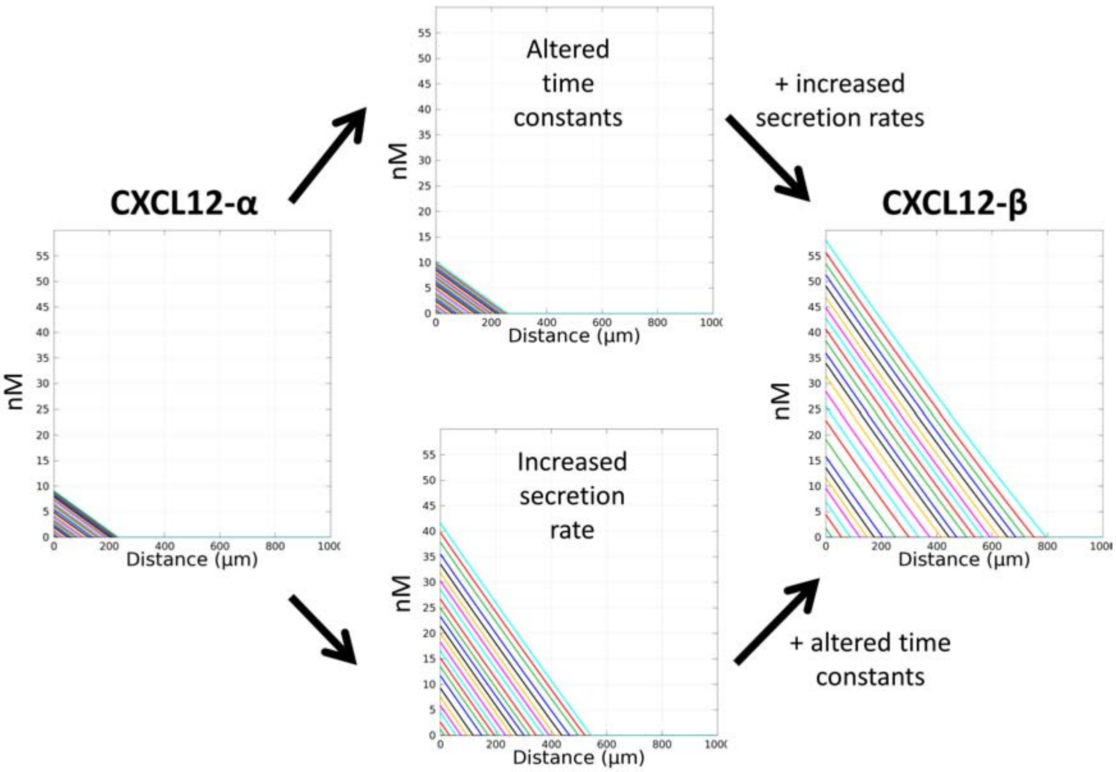

Figure 3.11. Varied simulation parameters to identify the different diffusion profiles for α and β isoforms of CXCL12. The combination of increased secretion rates and altered K_{on} and K_{off} values results in significantly accelerated diffusion profiles over 24 hours between CXCL12-α and CXCL12-β.

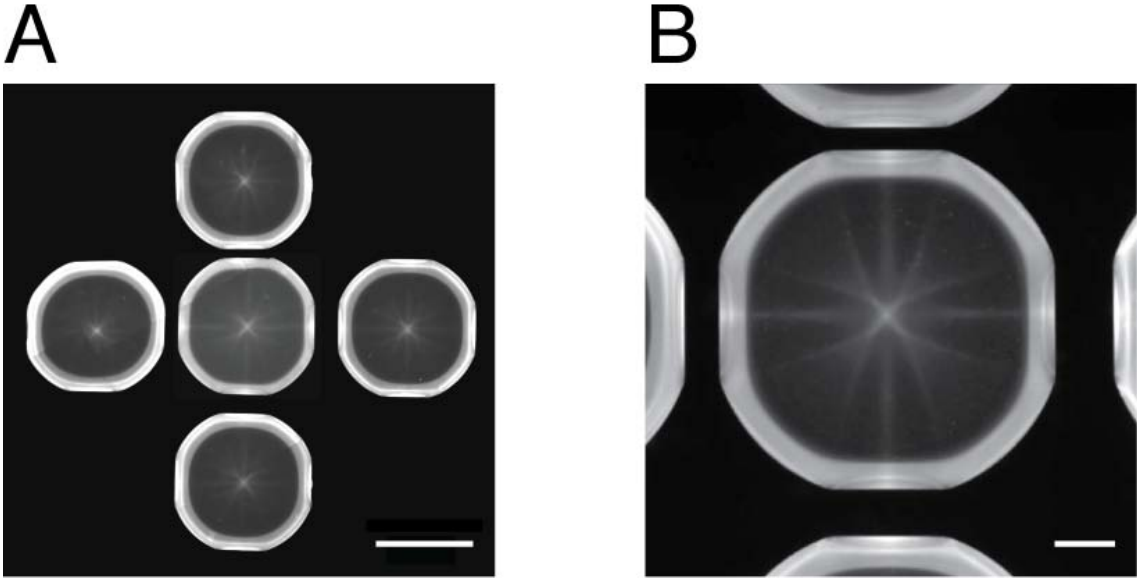

Figure 3.12. Multiplex gel patterning in air. (A) Stitched fluorescent image of multiple hydrogels in air encapsulating fluorescent beads having different pattern-to-pattern distances (200 µm, 300 µm, 400 µm, and 500 µm). Scale bar 500 µm.

3.6 References

1. Kay, R. R.; Langridge, P.; Traynor, D.; Hoeller, O., Changing directions in the study of chemotaxis. *Nat. Rev. Mol. Cell Biol.* **2008,** *9*, 455-463.

2. Weber, M.; Hauschild, R.; Schwarz, J.; Moussion, C.; de Vries, I.; Legler, D. F.; Luther, S. A.; Bollenbach, T.; Sixt, M., Interstitial dendritic cell guidance by haptotactic chemokine gradients. *Science* **2013,** *339*, 328-332.

3. Fleury, M. E.; Boardman, K. C.; Swartz, M. A., Autologous morphogen gradients by subtle interstitial flow and matrix interactions. *Biophys. J.* **2006,** *91*, 113-121.

4. Dona, E.; Barry, J. D.; Valentin, G.; Quirin, C.; Khmelinskii, A.; Kunze, A.; Durdu, S.; Newton, L. R.; Fernandez-Minan, A.; Huber, W., Directional tissue migration through a self-generated chemokine gradient. *Nature* **2013,** *503*, 285-89.

5. Torisawa, Y.-s.; Mosadegh, B.; Cavnar, S. P.; Ho, M.; Takayama, S., Transwells with microstamped membranes produce micropatterned two-dimensional and three-dimensional co-cultures. *Tissue Eng. PartC* **2010,** *17*, 61-67.

6. Aubin, H.; Nichol, J. W.; Hutson, C. B.; Bae, H.; Sieminski, A. L.; Cropek, D. M.; Akhyari, P.; Khademhosseini, A., Directed 3D cell alignment and elongation in microengineered hydrogels. *Biomaterials* **2010,** *31*, 6941-6951.

7. Tang, X.; Ali, M. Y.; Saif, M. T. A., A novel technique for micro-patterning proteins and cells on polyacrylamide gels. *Soft matter* **2012,** *8*, 7197-7206.

8. Nelson, C. M.; VanDuijn, M. M.; Inman, J. L.; Fletcher, D. A.; Bissell, M. J., Tissue geometry determines sites of mammary branching morphogenesis in organotypic cultures. *Science* **2006,** *314*, 298-300.

9. Lee, G. Y.; Kenny, P. A.; Lee, E. H.; Bissell, M. J., Three-dimensional culture models of normal and malignant breast epithelial cells. *Nat. methods* **2007,** *4*, 359-365.

10. He, J.; Mao, M.; Liu, Y.; Shao, J.; Jin, Z.; Li, D., Fabrication of Nature-inspired microfluidic network for perfusable tissue constructs. *Adv. Healthc. Mater.* **2013,** *2*, 1108-1113.

11. Zervantonakis, I. K.; Hughes-Alford, S. K.; Charest, J. L.; Condeelis, J. S.; Gertler, F. B.; Kamm, R. D., Three-dimensional microfluidic model for tumor cell intravasation and endothelial barrier function. *Proc. Natl. Acad. Sci. USA* **2012,** *109*, 13515-13520.

12. Mosadegh, B.; Huang, C.; Park, J. W.; Shin, H. S.; Chung, B. G.; Hwang, S.-K.; Lee, K.-H.; Kim, H. J.; Brody, J.; Jeon, N. L., Generation of stable complex gradients across two-dimensional surfaces and three-dimensional gels. *Langmuir* **2007,** *23*, 10910-10912.

13. Saadi, W.; Rhee, S. W.; Lin, F.; Vahidi, B.; Chung, B. G.; Jeon, N. L., Generation of stable concentration gradients in 2D and 3D environments using a microfluidic ladder chamber. *Biomed. Microdevices* **2007,** *9*, 627-635.

14. Wang, S.-J.; Saadi, W.; Lin, F.; Minh-Canh Nguyen, C.; Li Jeon, N., Differential effects of EGF gradient profiles on MDA-MB-231 breast cancer cell chemotaxis. *Exp. Cell. Res.* **2004,** *300*, 180-189.

15. Barkefors, I.; Le Jan, S.; Jakobsson, L.; Hejll, E.; Carlson, G.; Johansson, H.; Jarvius, J.; Park, J. W.; Jeon, N. L.; Kreuger, J., Endothelial cell migration in stable gradients of vascular endothelial growth factor A and fibroblast growth factor 2 effects on chemotaxis and chemokinesis. *J. Biol. Chem.* **2008,** *283*, 13905-13912.

16. Mosadegh, B.; Saadi, W.; Wang, S. Ä.; Jeon, N. L., Epidermal growth factor promotes breast cancer cell chemotaxis in CXCL12 gradients. *Biotechnol. Bioeng.* **2008,** *100*, 1205-1213.

17. Torisawa, Y.-s.; Mosadegh, B.; Bersano-Begey, T.; Steele, J. M.; Luker, K. E.; Luker, G. D.; Takayama, S., Microfluidic platform for chemotaxis in gradients formed by CXCL12 source-sink cells. *Integr. Biol.* **2010,** *2*, 680-686.

18. Cavnar, S.; Ray, P.; Moudgil, P.; Chang, S.; Luker, K.; Linderman, J.; Takayama, S.; Luker, G., Microfluidic source-sink model reveals effects of biophysically distinct CXCL12 isoforms in breast cancer chemotaxis. *Integr. Biol.* **2014,** *6*, 564-576.

19. Wylie, R. G.; Ahsan, S.; Aizawa, Y.; Maxwell, K. L.; Morshead, C. M.; Shoichet, M. S., Spatially controlled simultaneous patterning of multiple growth factors in three-dimensional hydrogels. *Nat. Mater.* **2011,** *10*, 799-806.

20. Hoffmann, J. C.; West, J. L., Three-dimensional photolithographic micropatterning: a novel tool to probe the complexities of cell migration. *Integr. Biol.* **2013,** *5*, 817-827.

21. Mosiewicz, K. A.; Kolb, L.; van der Vlies, A. J.; Martino, M. M.; Lienemann, P. S.; Hubbell, J. A.; Ehrbar, M.; Lutolf, M. P., In situ cell manipulation through enzymatic hydrogel photopatterning. *Nat. Mater.* **2013,** *12*, 1072-1078.

22. Odawara, A.; Gotoh, M.; Suzuki, I., Control of neural network patterning using collagen gel photothermal etching. *Lab Chip* **2013,** *13*, 2040-2046.

23. Pregibon, D. C.; Toner, M.; Doyle, P. S., Magnetically and biologically active bead-patterned hydrogels. *Langmuir* **2006,** *22*, 5122-5128.

24. Akselrod, G.; Timp, W.; Mirsaidov, U.; Zhao, Q.; Li, C.; Timp, R.; Timp, K.; Matsudaira, P.; Timp, G., Laser-guided assembly of heterotypic three-dimensional living cell microarrays. *Biophys. J.* **2006,** *91*, 3465-3473.

25. Mirsaidov, U.; Scrimgeour, J.; Timp, W.; Beck, K.; Mir, M.; Matsudaira, P.; Timp, G., Live cell lithography: using optical tweezers to create synthetic tissue. *Lab Chip* **2008,** *8*, 2174-2181.

26. Eng, G.; Lee, B. W.; Parsa, H.; Chin, C. D.; Schneider, J.; Linkov, G.; Sia, S. K.; Vunjak-Novakovic, G., Assembly of complex cell microenvironments using geometrically docked hydrogel shapes. *Proc. Natl. Acad. Sci. USA* **2013,** *110*, 4551-4556.

27. Khademhosseini, A.; Langer, R., Microengineered hydrogels for tissue engineering. *Biomaterials* **2007,** *28*, 5087-5092.

28. Bong, K. W.; Bong, K. T.; Pregibon, D. C.; Doyle, P. S., Hydrodynamic focusing lithography. *Angew. Chem.* **2010,** *122*, 91-94.

29. Song, J. W.; Cavnar, S. P.; Walker, A. C.; Luker, K. E.; Gupta, M.; Tung, Y.-C.; Luker, G. D.; Takayama, S., Microfluidic endothelium for studying the intravascular adhesion of metastatic breast cancer cells. *PLoS ONE* **2009,** *4*, e5756.

30. Fiddes, L. K.; Chan, H. K. C.; Lau, B.; Kumacheva, E.; Wheeler, A. R., Durable, region-specific protein patterning in microfluidic channels. *Biomaterials* **2010,** *31*, 315-320.

31. Simmons, C. S.; Ribeiro, A. J.; Pruitt, B. L., Formation of composite polyacrylamide and silicone substrates for independent control of stiffness and strain. *Lab Chip* **2013,** *13*, 646-649.

32. Kojima, T.; Takayama, S., Patchy Surfaces Stabilize Dextran-Polyethylene Glycol Aqueous Two-Phase System Liquid Patterns. *Langmuir* **2013,** *29*, 5508-5514.

33. Folch, A.; Toner, M., Cellular micropatterns on biocompatible materials. *Biotechnol. Progr.* **1998,** *14*, 388-392.

34. Raghavan, S.; Shen, C. J.; Desai, R. A.; Sniadecki, N. J.; Nelson, C. M.; Chen, C. S., Decoupling diffusional from dimensional control of signaling in 3D culture reveals a role for myosin in tubulogenesis. *J. Cell Sci.* **2010,** *123*, 2877-2883.

35. Laguri, C.; Sadir, R.; Rueda, P.; Baleux, F.; Gans, P., renzana-Seisdedos, F., and Lortat-Jacob, H.(2007) The novel CXCL12gamma isoform encodes an unstructured cationic domain which regulates bioactivity and interaction with both glycosaminoglycans and CXCR4. *PLoS ONE 2*, e1110.

36. Adamson, A. W.; Gast, A. P., *Physical Chemistry of Surfaces*. 6th ed.; John Wiley & Sons, Inc.: 1997.

37. Chiang, E. N.; Dong, R.; Ober, C. K.; Baird, B. A., Cellular responses to patterned poly (acrylic acid) brushes. *Langmuir* **2011,** *27*, 7016-7023.

38. Tavana, H.; Jovic, A.; Mosadegh, B.; Lee, Q.; Liu, X.; Luker, K.; Luker, G.; Weiss, S.; Takayama, S., Nanoliter liquid patterning in aqueous environments for spatially-defined reagent delivery to mammalian cells. *Nat. Mater.* **2009,** *8*, 736-741.

39. Lu, P.; Weaver, V. M.; Werb, Z., The extracellular matrix: a dynamic niche in cancer progression. *J. Cell Biol.* **2012,** *196*, 395-406.

40. Koninger, J.; Giese, T.; di Mola, F. F.; Wente, M. N.; Esposito, I.; Bachem, M. G.; Giese, N. A.; Buchler, M. W.; Friess, H., Pancreatic tumor cells influence the composition of the extracellular matrix. *Biochem. Biophys. Res. Commun.* **2004,** *322*, 943-949.

41. Sasisekharan, R.; Shriver, Z.; Venkataraman, G.; Narayanasami, U., Roles of heparan-sulphate glycosaminoglycans in cancer. *Nat. Rev. Cancer* **2002,** *2*, 521-528.

42. Okolicsanyi, R. K.; van Wijnen, A. J.; Cool, S. M.; Stein, G. S.; Griffiths, L. R.; Haupt, L. M., Heparan sulfate proteoglycans and human breast cancer epithelial cell tumorigenicity. *J. Cell. Biochem.* **2013,** *115*, 967-76.

43. Kreuger, J.; Salmivirta, M.; Sturiale, L.; Gimenez-Gallego, G.; Lindahl, U., Sequence analysis of heparan sulfate epitopes with graded affinities for fibroblast growth factors 1 and 2. *J. Biol. Chem.* **2001,** *276*, 30744-30752.

44. Sadir, R.; Imberty, A.; Baleux, F. ß.; Lortat-Jacob, H., Heparan sulfate/heparin oligosaccharides protect stromal cell-derived factor-1 (SDF-1)/CXCL12 against proteolysis induced by CD26/dipeptidyl peptidase IV. *J. Biol. Chem.* **2004,** *279*, 43854-43860.

45. Dambly-Chaudiere, C.; Cubedo, N.; Ghysen, A., Control of cell migration in the development of the posterior lateral line: antagonistic interactions between the chemokine receptors CXCR4 and CXCR7/RDC1. *BMC Dev. Biol.* **2007,** *7*, 23.

46. Luhmann, T.; Hall, H., Cell guidance by 3D-gradients in hydrogel matrices: importance for biomedical applications. *Materials* **2009,** *2*, 1058-1083.

47. Luhmann, T.; Hanseler, P.; Grant, B.; Hall, H., The induction of cell alignment by covalently immobilized gradients of the 6th Ig-like domain of cell adhesion molecule L1 in 3D-fibrin matrices. *Biomaterials* **2009,** *30*, 4503-4512.

48. DeLong, S. A.; Moon, J. J.; West, J. L., Covalently immobilized gradients of bFGF on hydrogel scaffolds for directed cell migration. *Biomaterials* **2005,** *26*, 3227-3234.

49. Seidi, A.; Ramalingam, M.; Elloumi-Hannachi, I.; Ostrovidov, S.; Khademhosseini, A., Gradient biomaterials for soft-to-hard interface tissue engineering. *Acta Biomater* **2011,** *7*, 1441-1451.

50. Raghavan, S.; Nelson, C. M.; Baranski, J. D.; Lim, E.; Chen, C. S., Geometrically controlled endothelial tubulogenesis in micropatterned gels. *Tissue Engineering PartA* **2010,** *16*, 2255-2263.

51. Staton, C. A.; Reed, M. W.; Brown, N. J., A critical analysis of current in vitro and in vivo angiogenesis assays. *Int. J. Exp. Pathol.* **2009,** *90*, 195-221.

52. Sung, S.-Y.; Hsieh, C.-L.; Wu, D.; Chung, L. W.; Johnstone, P. A., Tumor microenvironment promotes cancer progression, metastasis, and therapeutic resistance. *Curr. Prob. Cancer* **2007,** *31*, 36-100.

53. Bhowmick, N. A.; Neilson, E. G.; Moses, H. L., Stromal fibroblasts in cancer initiation and progression. *Nature* **2004,** *432*, 332-337.

Chapter 4

Microscale Determination of Aqueous Two-Phase System Binodals by Droplet Dehydration in Oil

This chapter analyzes the use of a dehydrating oil system to determine binodal curves of aqueous two phase system (ATPS). Aqueous droplets containing phase-forming polymers are dehydrated at the interface between two immiscible oils. The droplets shrink due to diffusion of water into the oil phase while constantly maintaining a spherical shape. Upon sufficient dehydration, dilute one-phase solutions of phase-forming polymers separate into two phases. Comparison of the droplet diameter at this phase separation point and at the beginning allows facile calculation of the concentration of polymers that determine the binodal curve. The miniaturized droplet dehydration-based binodals obtained in this manner matched the binodals determined by the conventional diluting method but using several orders of magnitude less sample volume (150 nL droplets versus 10 mL vials).

4.1 Introduction

An aqueous two-phase system (ATPS) is composed of two immiscible polymer-based solutions, which forms two distinct aqueous phases. It is widely developed as a macroscale molecular separation technique.[1] Recently, it has been utilized for microscale applications such as reagent,[2] cell,[3] micelle,[4-6] microbubble,[7] microdroplet,[8] and bacteria micropatterning,[9] as well as for studies as a proto-cell model.[10, 11] ATPSs can enhance chemical[12, 13] and biological[14, 15] reactions by compartmentalizing molecules into one of the two phases. Having the phase diagram (binodal) of the two polymers in ATPSs is critical for handling and understanding ATPSs. The conventional method for determining the binodal of different ATPSs is to start with a concentrated 2-phase solution, and then to dilute it gradually until the phase boundary disappears (Scheme 4.1a). Generally, this requires large amounts of samples (on the order of grams of polymer).[16]

This work describes a different approach where small amounts of dilute 1-phase solutions are concentrated until 2-phases form. We validate the technique using commonly used polymer-polymer ATPSs as well as an uncommon protein-polymer ATPS. Previous work has shown that some organic oils like soybean oil with water-trapping groups can extract and entrap small amounts of water from water-in-oil droplets containing solutes, leading to concentration of the solutes.[17] A series of quantitative analyses of dehydration of aqueous microdroplets in soybean oil have been developed.[18-20] A recent study has demonstrated reversible phase transitions of microdroplets in PEG-DEX system.[21] We hypothesize that dilute, single phase solutions of ATPS-forming polymers can be dehydrated and concentrated in soybean oil to induce dynamic phase separation and allow determination of the binodal using small amounts of materials.

In our initial attempts we indeed observed dehydration and droplet shrinking. We were unable to determine a binodal curve, however, because the microdroplet volume calculations could not be performed accurately due to the formation of squashed, non-spherical droplet shapes that forms once the droplets stick to the wall or substrate. We therefore searched a method to eliminate wall contact of the droplets. An airborne analysis system using levitated droplets has been developed for concentrating solutes in miniaturized droplets by evaporation of water.[22-24] While two-phase formation of dilute dextran-polyethylene glycol (DEX-PEG) systems by evaporating a one-phase droplet through fluorescence imaging was reported,[25] the method requires complicated device set up, long settling times, and special volume calculations due to formation of an elliptical droplet shape during levitation.

To circumvent such technical issues, we next tried dehydration of miniature droplets (~ 150 nL) at an interface between two immiscible oils: fluorinated oil (FC-40) and soybean oil. Due to density differences, the aqueous droplets float at the interface with FC-40 (1.8 g/cm^3) at the bottom and soybean oil (0.92 g/cm^3) on top. The droplets maintained a spherical shape owing to the fluidity and hydrophobicity of the fluorinated oil together with some buoyance provided by the soybean oil, enabling straightforward quantitative volume calculation from time-lapse droplet images. Sub-millimeter sized single droplets were used in this system in order to facilitate the slow diffusion of water from the droplet. Use of surfactants that may affect phase forming behavior of ATPSs was avoided.

Dilute one-phase droplets containing ATPS phase-forming polymers dehydrated slowly until phase-forming polymers were concentrated slightly above the binodal concentration (Scheme 4.1b). We observed negligible leaking of phase-forming polymers into the oil phase because of their charged or polar nature. We used the microscale droplet dehydration method to determine bionodal curves from one-phase solutions of PEG-DEX, DEX-polyvinyl alcohol (PVA), PEG-PVA, and bovine serum albumin (BSA)-PEG systems. The method was validated by comparison with binodal curves obtained by the conventional macroscale diluting method.

4.2 Materials and Methods

Experimental Section

Materials

All chemicals and reagents were purchased from commercial sources: Fluorinert FC-40, soybean oil, Mw 10,000 and 500,000 DEX, Mw 8,000 and 35,000 PEG, and Mw 105,000 PVA were from Sigma-Aldrich; Mw 66,000 BSA was from Millipore; Mw 10,000 and 40,000 rhodamine B (RB)-PEG were from Nanocs; Mw 10,000 and 500,000 fluorescein isothiocyanate (FITC)-DEX were from TdB Consultancy; 35 mm x 10 mm disposable petri dish was from Fisher Scientific; phosphate-buffered saline (PBS) buffer solution (pH 7.4) was from GE Health Care.

Characterization

2.5 mL FC-40 and 3 mL soybean oil were poured into a petri dish. A droplet (~ 150 nL) was released by a micropipette at FC-40-soybean oil interface. All measurements were conducted at room temperature (25 °C). The initial volume of the droplet volume used in this work was one-order of magnitude smaller (~ 150 nL) than the maximum volume soybean oil can absorb; 3 µL of water can diffuse into 3 mL soybean oil in theory.

Contact Angle Measurement

Contact angles of PBS droplets in soybean oil on petri dish surface or FC-40-soybean oil interface were measured by the sessile drop technique and analyzed with ImageJ. Three sets of measurements were averaged.

Time-lapse Droplet Shrinking

PBS droplets at FC-40-soybean oil interface were continuously monitored. The cross section of the droplet viewed from the bottom was measured using an optical microscope (Nikon Eclipse TE 2000-U) and analyzed by ImageJ. Three sets of measurements were averaged.

Determination of ATPS Binodal Curve

40 w/w % 10k DEX, 20 w/w % 500k DEX, 50 w/w % 10k PEG, 20 w/w % 35k PEG, 20 w/w % PVA, and 20 w/w % BSA dissolved in PBS solution were used as stock solutions. In the diluting method, various solutions of phase-forming polymers (2 g in total) were diluted by PBS solution down to binodal points where phase boundary disappears after a 3000 rpm x 20 min centrifugation (Scheme 4.2a). Those points were fitted with the previously reported method[26] using R. In the dehydrating method, the binodal solutions were further diluted (~ 2 times) and an aliquot of the solutions (~ 150 nL) mixed with 0.001 w/w % FITC-DEX and/or RB-PEG was dispensed at FC-40-soybean oil interface and dehydrated through the aforementioned protocol (Scheme 4.2b). The binodal points were determined when phase separation became visually apparent. Images were taken by an optical microscope in the fluorescence imaging mode and analyzed by ImageJ.

Characterization of Dehydration of ATPS Droplets

The PEG-DEX binodal solutions prepared with the aforementioned dilution method were diluted 10, 20, 50, and 100 times. The binodal compositions were determined when phase separation became visually apparent. Images were taken by an optical microscope in the fluorescence imaging mode and analyzed by ImageJ.

Theoretical Section

We assume the diffusion of water in FC-40 is negligible due to low water solubility (< 0.0007 %v/v at 25 °C) compared to that of soybean oil (0.3 %v/v at 25 °C). As *Baipayee et al.* previously described, we adopt a pseudo-steady-state mass diffusion model with radial symmetry of PBS droplet shrinking. The rate of change of area, A, is given by:

$$\frac{dA}{dt} = -\frac{8\pi M_w D_{w,o}(C_{sat} - C_{ref})}{\rho_w} \quad (1)$$

Where M_w is the molecular weight of water, $D_{w,o}$ is the diffusion coefficient of water in soybean oil, ρ_w is the density of water, and C_{sat} and C_{ref} are the saturation concentration of water in oil and the concentration far away from the droplet, respectively. The volume as a function of time (t) is given by:

$$V = (Kt + V_0^{\frac{2}{3}})^{\frac{3}{2}} \quad (2)$$

Where V_0 is the initial volume and K is a constant given by,

$$K = -\left(\frac{128}{9}\right)^{\frac{1}{3}} \pi^{\frac{2}{3}} \left(\frac{M_w D_{w,o} C_{sat}}{\rho_w}\right) \quad (3)$$

It should be noted that it is very difficult to theoretically predict the shrinking rate and concentration of droplets that include water-soluble polymers because of deviations due to water sorption to those polymers. As we are focusing on the binodal concentration, we can simply calculate concentration as:

$$M_b = \left(\frac{V_0}{V_b}\right) M_i \quad (4)$$

Where M_i and M_b are the initial and binodal concentration and V_b is the volume when the concentration reaches binodal concentration.

4.3 Results and Discussion

Figure 4.1 shows the results of the contact angle measurement of PBS droplets in soybean oil on a dish surface and at an FC-40-soybean oil interface. The sub-millimeter sized droplets sank to the bottom of the soybean oil layer within 1 min after releasing from a micropipette. The droplet at the FC-40-soybean oil interface retains its spherical shape while the droplet released in soybean oil spreads on the dish surface as expected. The difference in droplet shape likely arises from the hydrophobic and fluid nature of the FC-40 surface. Importantly, the constant spherical shape allows facile calculation of the surface area and volume change from the cross sectional image of the droplet as shown in Scheme 4.1.

The surface area and volume of droplets of PBS solutions decreased over time due to the diffusion of water into the soybean oil phase as shown in Figure 4.2. We confirmed the diffusion of water in the sub-millimeter sized droplets followed a pseudo-steady-state mass diffusion model during our measurement time scale (eq 1 and eq 2). Although the diffusion of water from a sub-millimeter sized droplet of PBS solution in soybean oil was about 1 $\mu m^2/s$, the same order as a pure water droplet in soybean oil (5 $\mu m^2/s$ from ref 17), the rate of change in solute concentration was five-orders of magnitude lower than the microdroplets due to the smaller surface-to-volume ratio. We take advantage of this slow shrinking for determination of binodal in ATPSs that requires quantitative volume change calculation from the initial droplet state to the binodal droplet state.

Figure 4.3 shows ATPS phase formation upon dehydration of a 10k DEX – 8 k PEG system. The solution was homogeneous below the binodal concentration (Figure 4.3a, c, and e). However, two phases started to form once the concentration in the droplet approached the binodal concentration (Figure 4.3b, d, and f). Since we assume only water diffuses into soybean oil phase while other molecules retain in the droplet, we can calculate the binodal concentrations from the images of droplets (eq 4). We defined the binodal state where the phase morphology changed from the initial phase morphology (Figure 4.8a) upon dehydration (Figure 4.8b and c).

We confirmed accurate volume calculations up to 50 times condensation. Dehydration of the droplets above 50 times condensation requires the droplets shrink down from sub-millimeter to tens of micron. Although increases in concentration of over 1000 times are theoretically plausible, the very small droplets that will need to be observed change concentrations so rapidly that accurate binodal concentration determination becomes difficult. In practical implementations, one often already knows the approximate binodal curve (e.g. for characterizing different batches of known ATPS forming polymers). Even for unknown polymer combinations, one or two approximate point along the binodal curve can be roughly measured first before a full binodal curve determination.

Low Mw and high Mw PEG-DEX systems were validated as shown in Figure 4.4. The uncertainty of this dehydrating method in determining the binodal curve is shown for low Mw PEG-DEX system in Figure 4.9. Not unexpectedly, the binodal points were slightly above the binodal curve determined by the diluting method. The true binodal curve is expected to be between these two types of binodal curves determined. We also observed that the phase morphology of the droplets far above binodal points differed depending on the polymer composition (Figure 4.10). This robustness of forming ATPSs across different concentrations of polymers shows that the dehydrating method is applicable for use in determining the binodal all along the binodal curve and for various low Mw to high Mw PEG-DEX combinations. Although we observed the binodal states using both phase contrast and fluorescent images for confirmation purposes, the binodal states can be determined from phase contrast images alone (Figure 4.3d).

We next validated other ATPSs as shown in Figure 4.5. The binodal points determined by phase contrast images agreed well with the binodal curves determined by the diluting method in both DEX-PVA and PEG-PVA systems (Figure 4.13d and e). It indicates that this dehydrating method is applicable to a wide range of ATPSs that use different synthetic polymers. We also tested if this method is applicable to expensive molecules like natural proteins. Thus, we next tested 66 k BSA – 35 k PEG system as shown in Figure 4.6. The binodal points agreed well with the binodal curve obtained with conventional methods. We observed no conspicuous leaking of BSA during our measurement time frame (~ 12 hours) and confirmed binodal states by both phase contrast and fluorescent images (Figure 4.13f and 4.14). This result suggests that the microscale dehydrating method is effective for polymer-protein ATPS systems as well.

The total amount of proteins used in the microscale dehydration method for binodal determination is remarkably small (µg) compared to the conventional diluting method (g). Thus, this method opens the ability to explore the suitability, as phase forming polymers, of a variety of natural proteins, synthetic peptides, or nucleic acids that are usually limited and expensive.

4.4 Conclusions

We demonstrate a novel method for the determination of binodals of ATPSs using quantitative analysis of dehydration of aqueous solution droplets in soybean oil. Water-soluble phase-forming molecules in ATPSs typically have charges or polar groups, allowing them to be retained in the aqueous rather than oil phase. Slow rate of diffusion of water with a constant spherical shape at an FC-40-soybean oil interface allows easy volume change calculation over time and provides quantitative determination of binodals. Although we utilized fluorescently labeled polymers in some of the demonstrations, binodals are readily determined without fluorescent-tagged phase-forming molecules in all cases studied. This method is envisioned to be particularly versatile for analysis of ATPSs where the amounts of samples are limited (~ µg) and the diluting method, which requires large amounts of the samples (g), cannot be used. The slow dehydration rate and small droplet volumes is advantageous for careful observation of the phase separation phenomenon close to the binodal as the process requires a certain amount of settling time for the phases to separate.

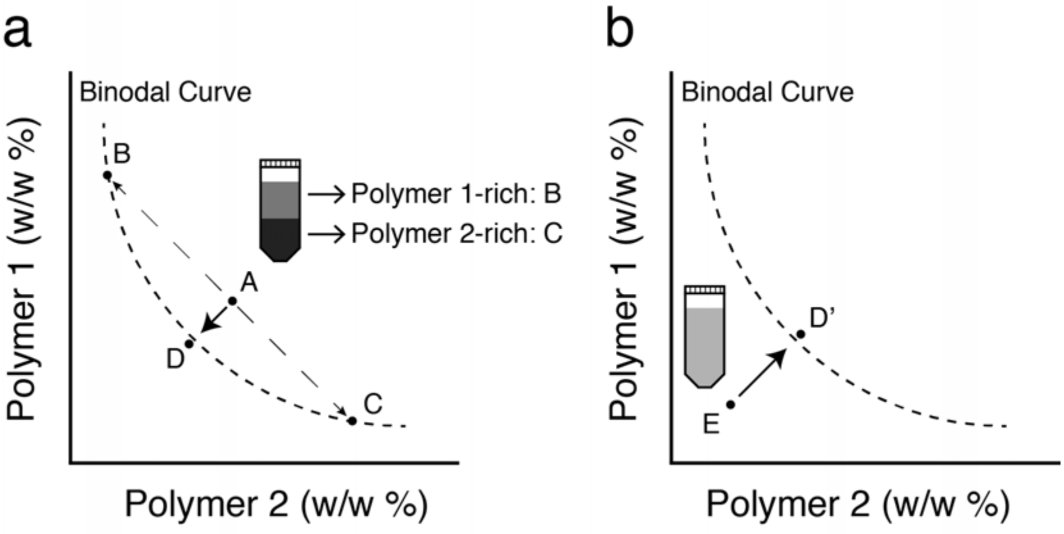

Scheme 4.1. Determination of binodal curves by dilution and concentration: a) the conventional diluting technique defines the binodal point when an interface disappears (Point D) by diluting the concentrated two-phase solution (Point A). In contrast, b) the dehydrating technique defines the binodal point as the point at which two phases starts forming (Point D') by dehydrating the dilute one-phase solution (Point E).

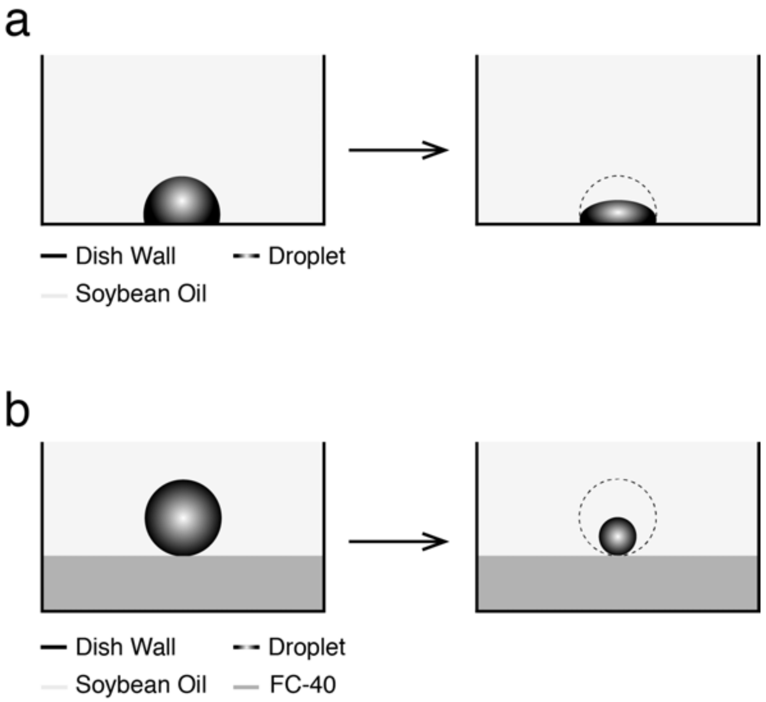

Scheme 4.2. Schematic image of droplet shrinking in soybean oil on: a) a petri dish surface, or b) an FC-40 oil surface.

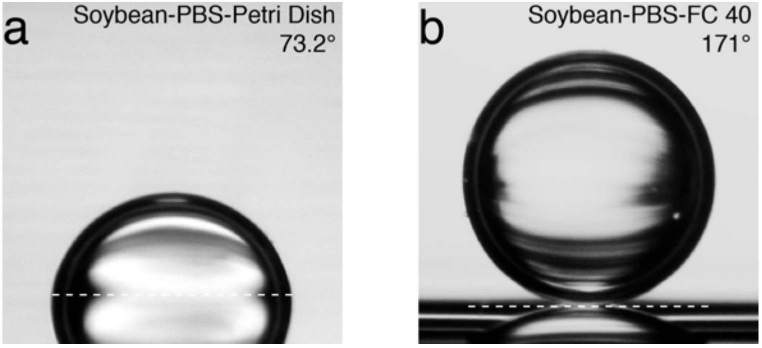

Figure 4.1. Shapes of droplets of PBS solution in soybean oil on a) dish substrate and b) FC-40.

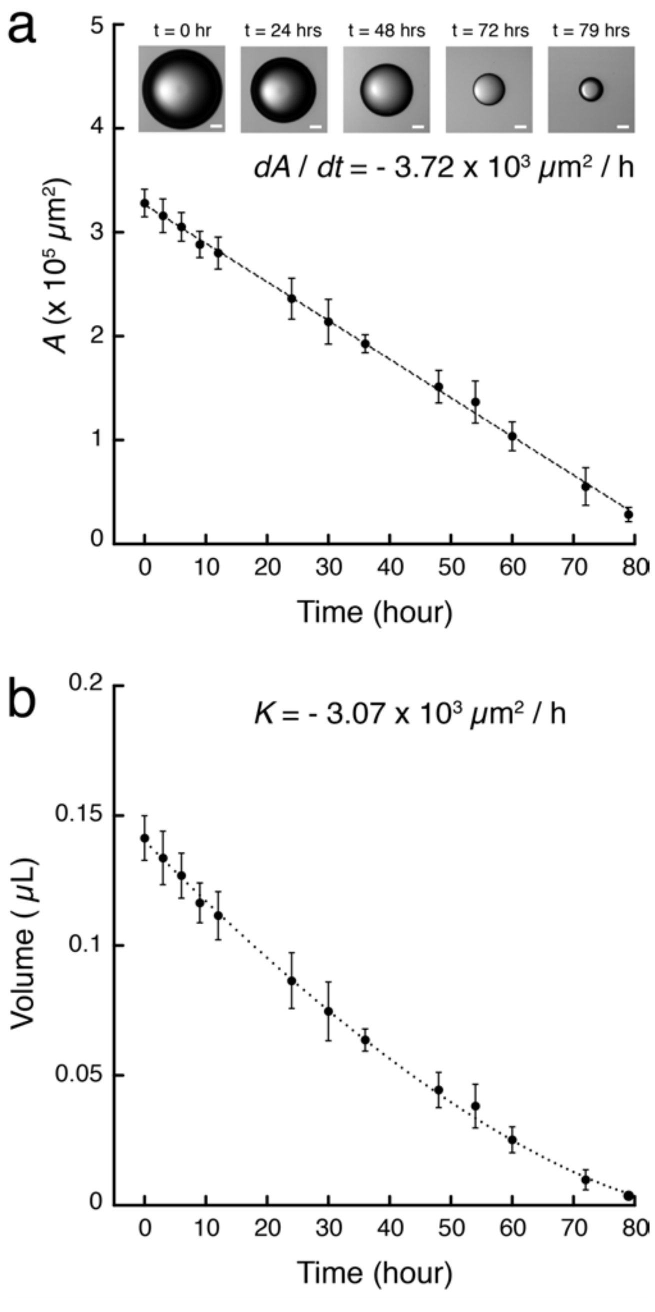

Figure 4.2. Time-lapse droplet shrinking of a PBS solution. a) The surface area of the droplets decreased linearly as a function of time. b) The volume of the droplets decreased exponentially as a function of time. Eq 1 (a) and eq 2 (b) were fitted into the plots (dotted line). Measurements were conducted at 25 °C. Scale bar 100 µm.

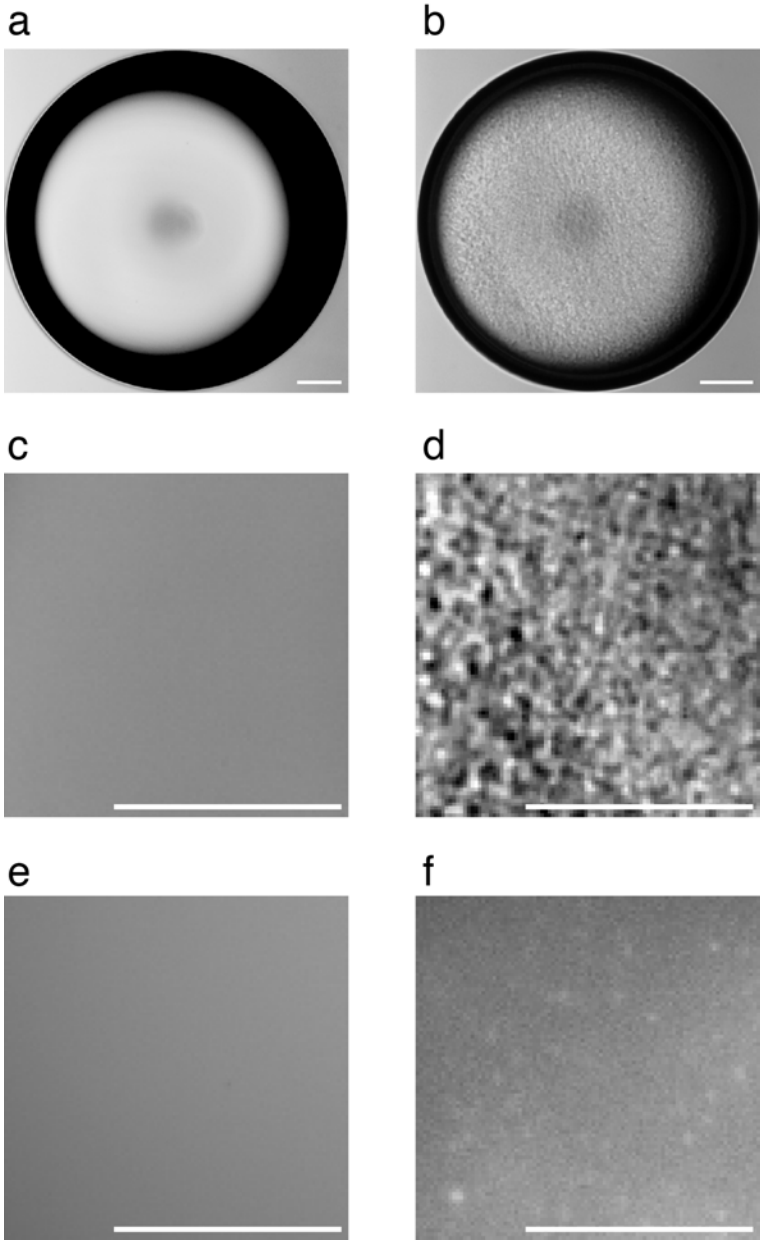

Figure 4.3. Phase separation at the binodal point of a 10k DEX - 8k PEG system induced by dehydration of water. The phase contrast images and magnified images at concentrations below the binodal point (a and c) and at the binodal point (b and d). Fluorescent images of DEX below the binodal point (e) and at the binodal point (f) are also shown. Measurements were conducted at 25 °C. Scale bar 100 µm.

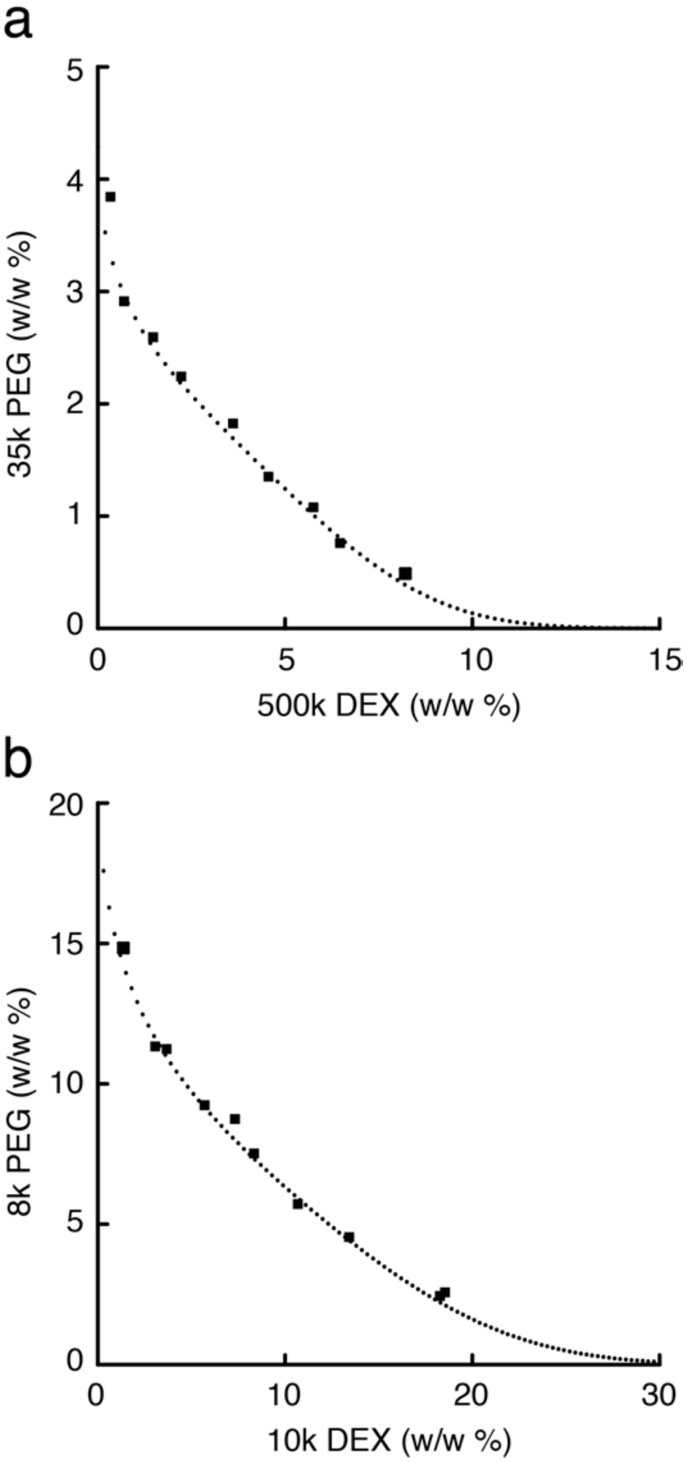

Figure 4.4. Binodal points (closed square) in DEX-PEG system determined by the dehydrating method: a) 500k DEX – 35k PEG and b) 10k DEX – 8k PEG. The binodal curves (dotted curve line) determined by the diluting method (Figure 4.7). Measurements were conducted at 25 °C.

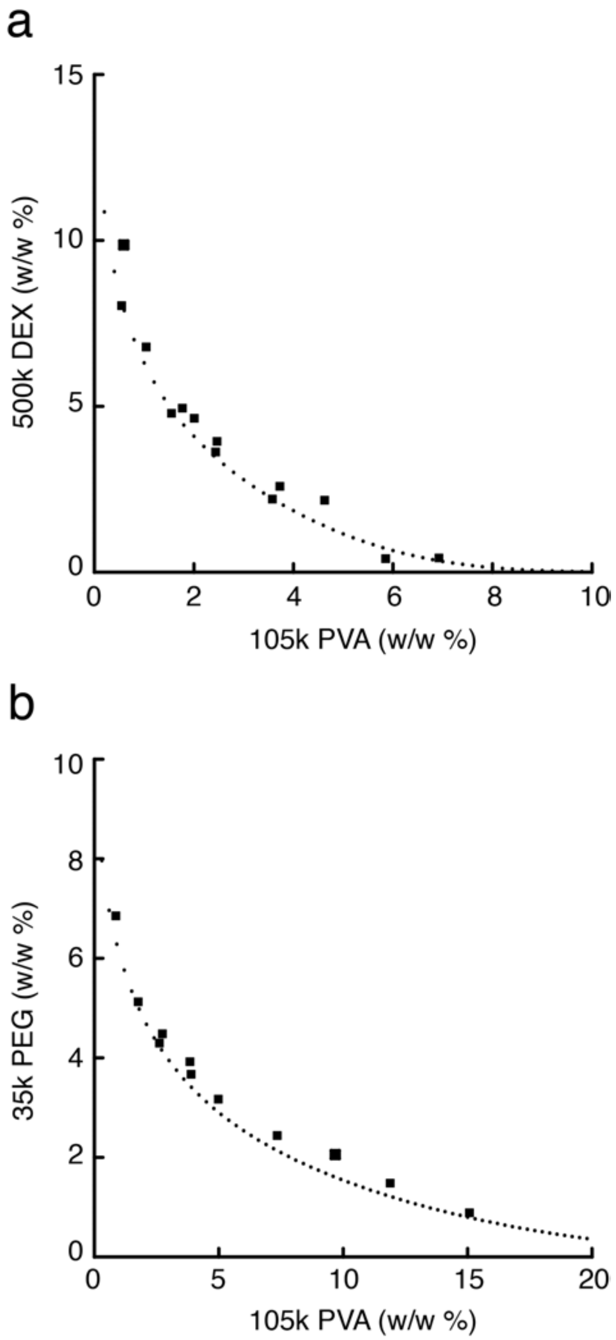

Figure 4.5. Binodal points (closed square) in DEX-PVA system and PEG-PVA system determined by the dehydrating method: a) 500k DEX – 105k PVA and b) 35k PEG – 105k PVA. The binodal curve (dotted curve line) determined by the diluting method (Figure 4.11). Measurements were conducted at 25 °C.

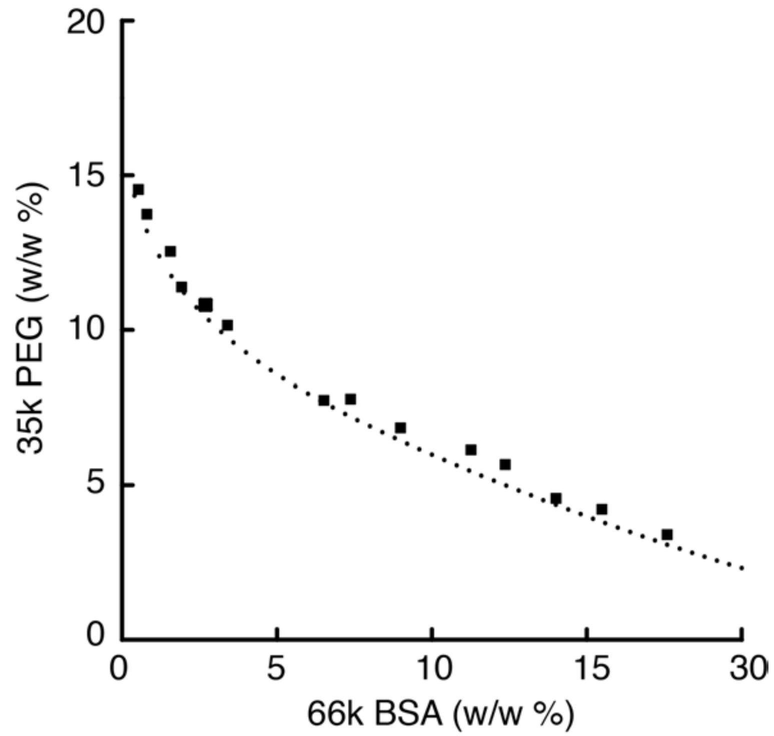

Figure 4.6. Binodal points (closed square) in 66k BSA – 35k PEG system determined by the dehydrating method. The binodal curve (dotted curve line) determined by the diluting method (Figure 4.12). Measurements were conducted at 25 °C.

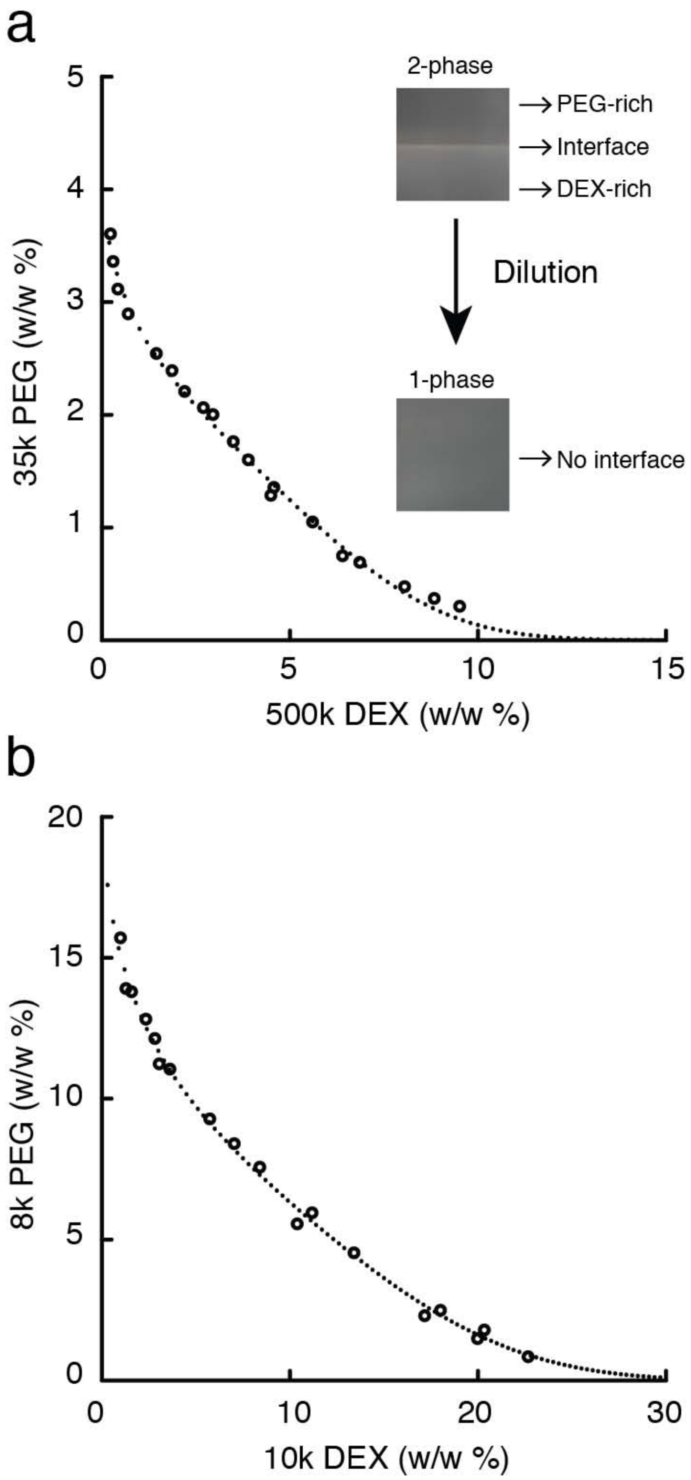

Figure 4.7. Binodal points (open circle) in DEX-PEG system determined by the diluting technique: a) 500k DEX – 35k PEG and b) 10k DEX – 8k PEG. Those points were fitted (see ref 25) to obtain a binodal curve (dotted curve line). Measurements were conducted at 25 °C.

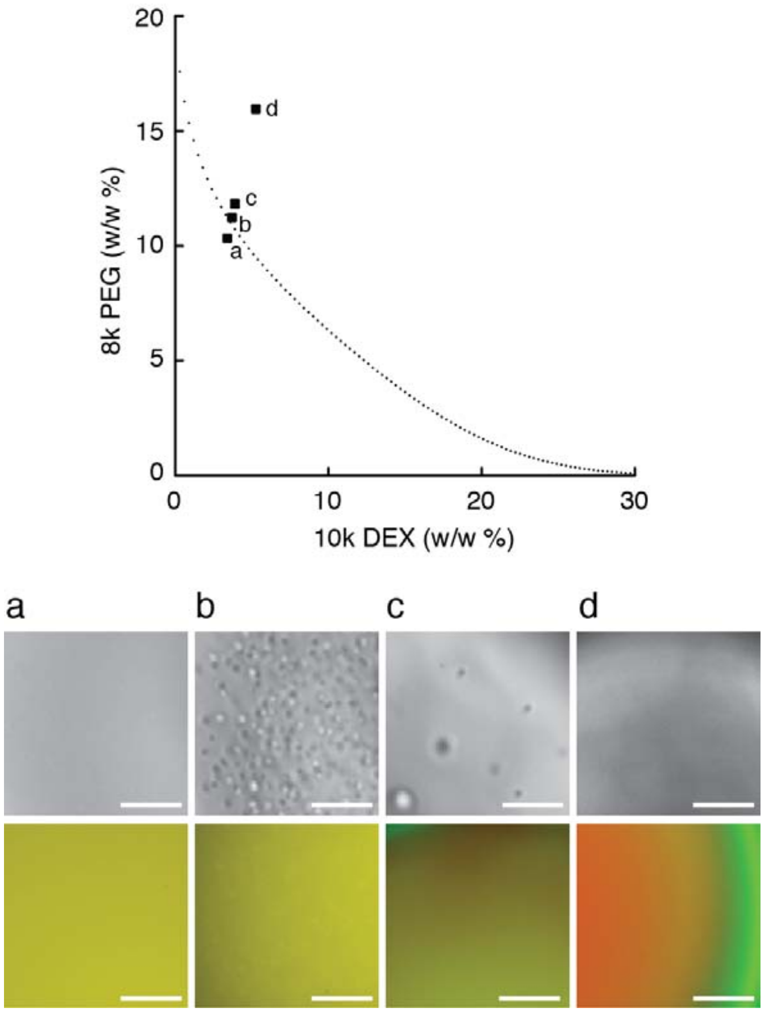

Figure 4.8. Time-lapse droplet images in 10k DEX – 8k PEG system determined by the dehydrating technique: a) before Binodal, b-c) on binodal, and d) completed phase separation. Phase contrast images (top) and merged fluorescent images (bottom) of DEX (green) and PEG (red). Measurements were conducted at 25 °C. Scale bar 50 µm.

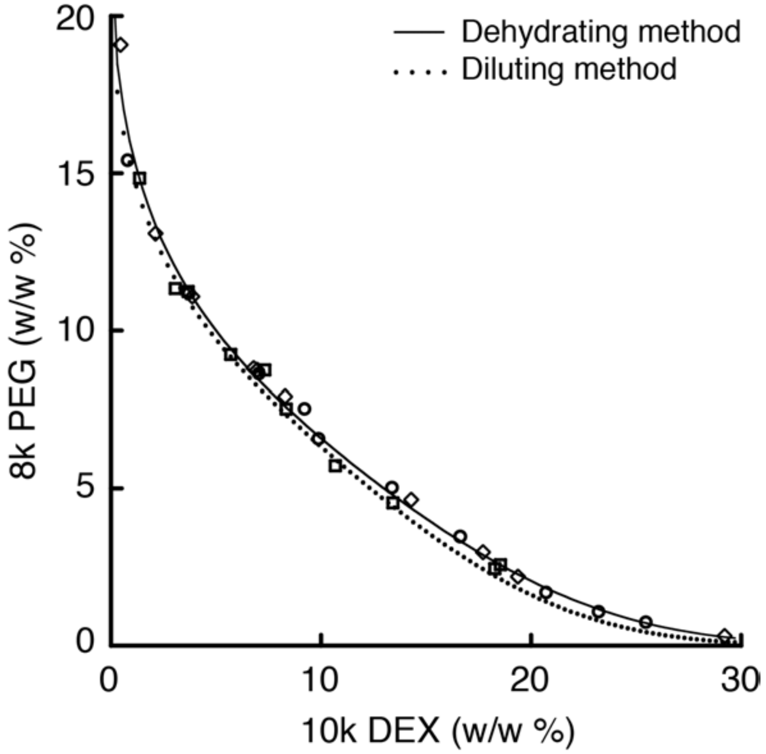

Figure 4.9. The uncertainty of binodal points in 10k DEX – 8k PEG system determined by the dehydrating technique: three independent measurements (open square, diamond, and circle). Binodal curves determined by the dehydrating technique (solid line) and diluting technique (dotted line). Measurements were conducted at 25 °C.

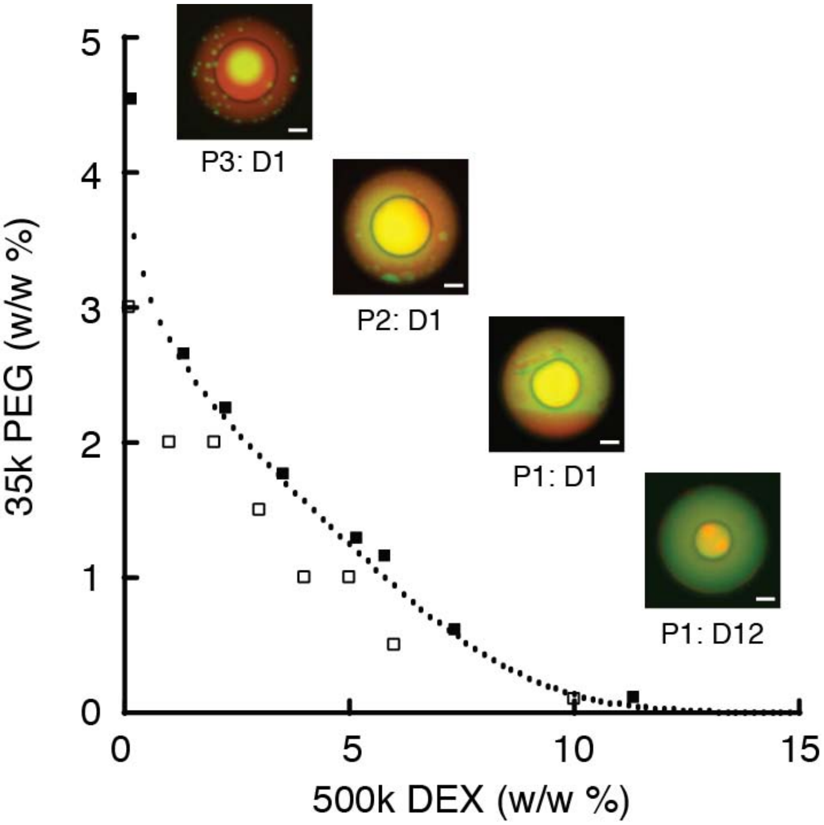

Figure 4.10. Binodal points (closed square) for a 500k DEX – 35k PEG system determined by the dehydrating technique. Various initial concentrations of 1-phase DEX-PEG solution (open square) were tested. The merged fluorescent images of DEX (green) and PEG (red) after 24 hours of dehydration far above the critical points. Measurements were conducted at 25 °C.

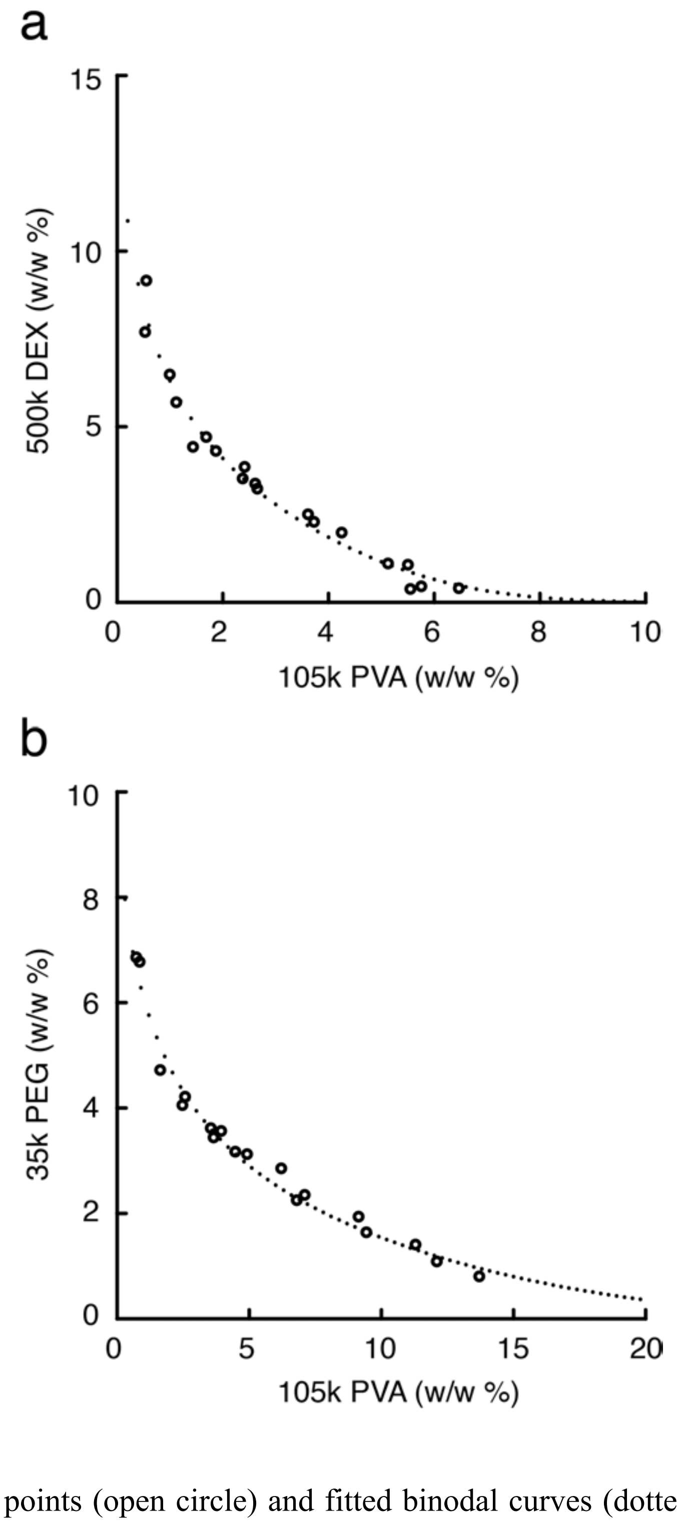

Figure 4.11. Binodal points (open circle) and fitted binodal curves (dotted curve line) in DEX-PVA system and PEG-PVA system determined by the diluting technique: a) 500k DEX – 105k PVA and b) 35k PEG – 105k PVA. Measurements were conducted at 25 °C.

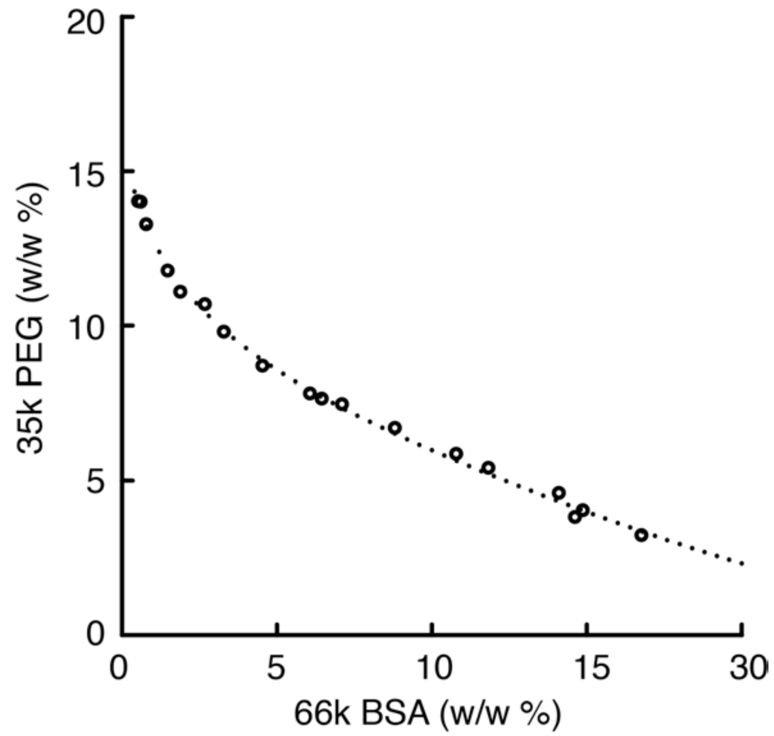

Figure 4.12. Binodal points (open circules) and fitted binodal curves (dotted curve line) in 66k BSA – 35k PEG system determined by the diluting technique. Measurements were conducted at 25 °C.

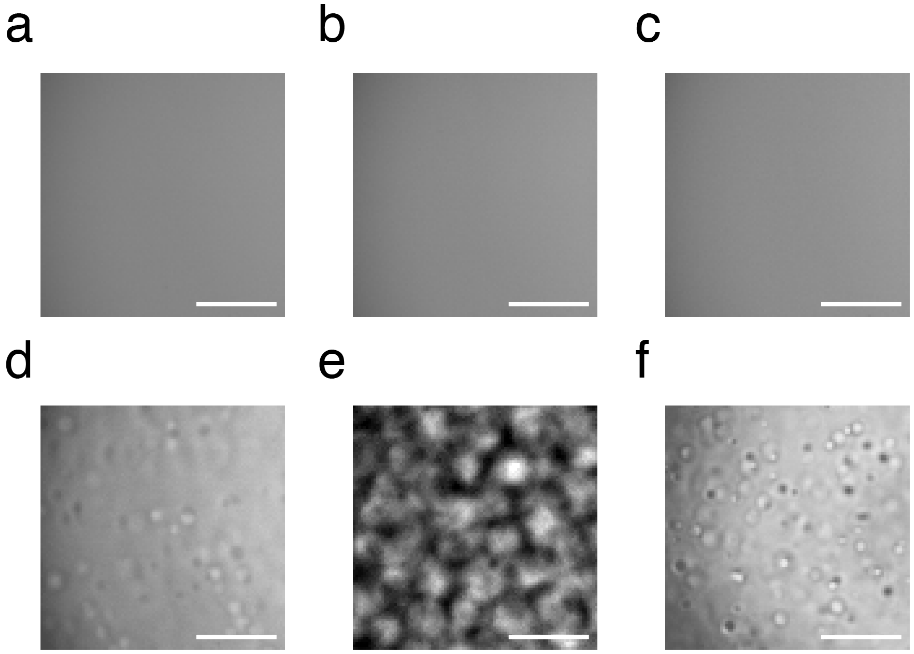

Figure 4.13. Magnified phase contrast images of droplets below and at binodal point. Droplets in 500k DEX – 105k PVA, 35k PEG – 105k PVA, and 66k BSA – 35k PEG systems below binodal point (a, b, and c), and at binodal point (d, e, and f), respectively. Measurements were conducted at 25 °C. Scale bar 50 μm.

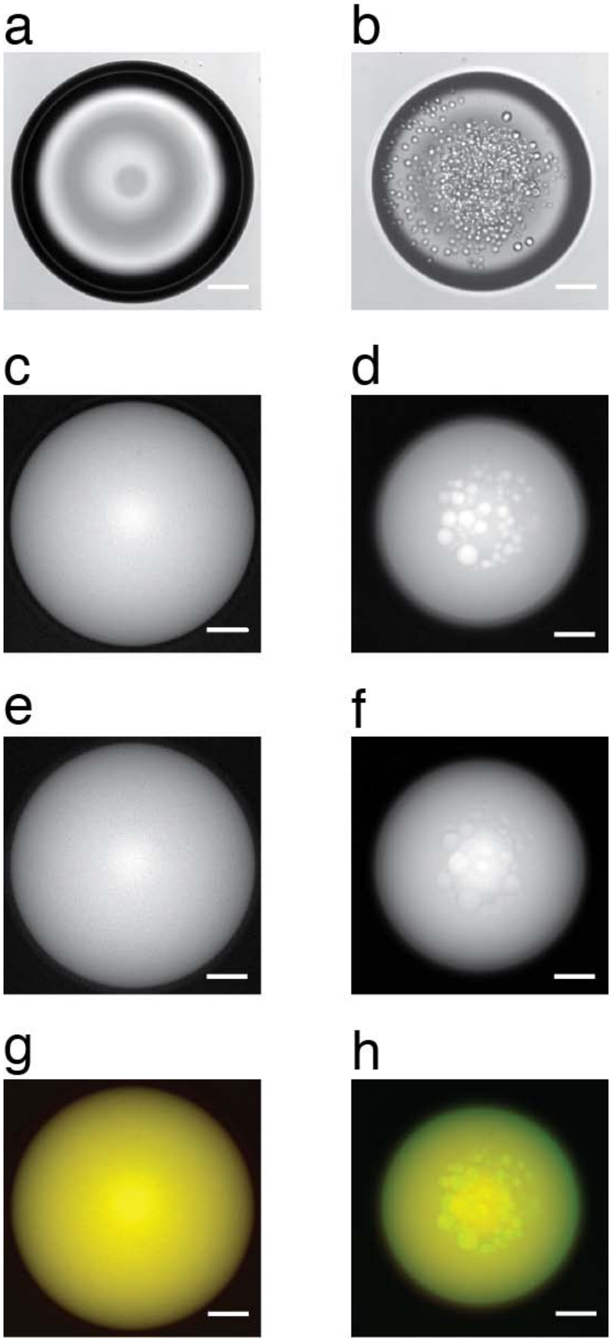

Figure 4.14. Phase separation at binodal point in 66k BSA - 35k PEG system induced by dehydration of water. The phase contrast images, fluorescent images of BSA and PEG at below binodal point (a, c, and e) and at binodal point (b, d, and f), respectively. The merged fluorescent images of BSA (green) and PEG (red) below binodal point (g) and at binodal point (h). Measurements were conducted at 25 °C. Scale bar 100 μm.

4.5 References

1. Albertsson, P.-A., *Partition of Cell Particles and Macromolecules*. 3rd ed.; John Wiley & Sons, Inc.: 1986.

2. Tavana, H.; Jovic, A.; Mosadegh, B.; Lee, Q.; Liu, X.; Luker, K.; Luker, G.; Weiss, S.; Takayama, S., Nanoliter Liquid Patterning in Aqueous Environments for Spatially-Defined Reagent Delivery to Mammalian Cells. *Nat. Mater.* **2009,** *8*, 736-741.

3. Tavana, H.; Mosadegh, B.; Takayama, S., Polymeric Aqueous Biphasic Systems for Non-Contact Cell Printing on Cells: Engineering Heterocellular Embryonic Stem Cell Niches. *Adv. Mater.* **2010,** *22*, 2628-2631.

4. Kamei, D. T.; Wang, D. I.; Blankschtein, D., Fundamental Investigation of Protein Partitioning in Two-Phase Aqueous Mixed (nonionic/ionic) Micellar Systems. *Langmuir* **2002,** *18*, 3047-3057.

5. Mashayekhi, F.; Meyer, A. S.; Shiigi, S. A.; Nguyen, V.; Kamei, D. T., Concentration of Mammalian Genomic DNA using Two-Phase Aqueous Micellar Systems. *Biotechnol. Bioeng.* **2009,** *102*, 1613-1623.

6. Mashayekhi, F.; Chiu, R. Y.; Le, A. M.; Chao, F. C.; Wu, B. M.; Kamei, D. T., Enhancing the Lateral-Flow Immunoassay for Viral Detection using an Aqueous Two-Phase Micellar System. *Anal. Bioanal. Chem.* **2010,** *398*, 2955-2961.

7. Frampton, J. P.; Fan, Z.; Simon, A.; Chen, D.; Deng, C. X.; Takayama, S., Aqueous Two-Phase System Patterning of Microbubbles: Localized Induction of Apoptosis in Sonoporated Cells. *Adv. Funct. Mater.* **2013,** *23*, 3420-3431.

8. Hardt, S.; Hahn, T., Microfluidics with Aqueous Two-Phase Systems. *Lab Chip* **2012,** *12*, 434-442.

9. Byun, C. K.; Hwang, H.; Choi, W. S.; Yaguchi, T.; Park, J.; Kim, D.; Mitchell, R. J.; Kim, T.; Cho, Y.-K.; Takayama, S., Productive Chemical Interaction between a Bacterial Microcolony Couple is Enhanced by Periodic Relocation. *J. Am. Chem. Soc.* **2013,** *135*, 2242-2247.

10. Keating, C. D., Aqueous Phase Separation as a Possible Route to Compartmentalization of Biological Molecules. *Acc. Chem. Res.* **2012,** *45*, 2114-2124.

11. Koga, S.; Williams, D. S.; Perriman, A. W.; Mann, S., Peptide-Nucleotide Microdroplets as a Step towards a Membrane-Free Protocell Model. *Nat. Chem.* **2011,** *3*, 720-724.

12. Cacace, D.; Keating, C. D., Biocatalyzed Mineralization in an Aqueous Two-Phase System: Effect of Background Polymers and Enzyme Partitioning. *J. Mater. Chem. B* **2013,** *1*, 1794-1803.

13. Crosby, J.; Treadwell, T.; Hammerton, M.; Vasilakis, K.; Crump, M. P.; Williams, D. S.; Mann, S., Stabilization and Enhanced Reactivity of Actinorhodin Polyketide Synthase Minimal Complex in Polymer-Nucleotide Coacervate Droplets. *Chem. Commun.* **2012,** *48*, 11832-11834.

14. Strulson, C. A.; Molden, R. C.; Keating, C. D.; Bevilacqua, P. C., RNA Catalysis through Compartmentalization. *Nat. Chem.* **2012,** *4*, 941-946.

15. Li, P.; Banjade, S.; Cheng, H.-C.; Kim, S.; Chen, B.; Guo, L.; Llaguno, M.; Hollingsworth, J. V.; King, D. S.; Banani, S. F., Phase Transitions in the Assembly of Multivalent Signalling Proteins. *Nature* **2012,** *483*, 336-340.

16. Mace, C. R.; Akbulut, O.; Kumar, A. A.; Shapiro, N. D.; Derda, R.; Patton, M. R.; Whitesides, G. M., Aqueous Multiphase Systems of Polymers and Surfactants Provide Self-Assembling Step-Gradients in Density. *J. Am. Chem. Soc.* **2012,** *134*, 9094-9097.

17. He, M.; Sun, C.; Chiu, D. T., Concentrating Solutes and Nanoparticles within Individual Aqueous Microdroplets. *Anal. Chem.* **2004,** *76*, 1222-1227.

18. Bajpayee, A.; Edd, J. F.; Chang, A.; Toner, M., Concentration of Glycerol in Aqueous Microdroplets by Selective Removal of Water. *Anal. Chem.* **2010,** *82*, 1288-1291.

19. Eslami, F.; Elliott, J. A., Design of Microdrop Concentrating Processes. *J. Phys. Chem. B* **2013,** *117*, 2205-2214.

20. Wu, T.; Hirata, K.; Suzuki, H.; Xiang, R.; Tang, Z.; Yomo, T., Shrunk to Femtolitre: Tuning High-Throughput Monodisperse Water-in-Oil Droplet Arrays for Ultra-Small Micro-Reactors. *Appl. Phys. Lett.* **2012,** *101*, 074108.

21. Boreyko, J. B.; Mruetusatorn, P.; Retterer, S. T.; Collier, C. P., Aqueous Two-Phase Microdroplets with Reversible Phase Transitions. *Lab Chip* **2013,** *13*, 1295-1301.

22. Santesson, S.; Johansson, J.; Taylor, L. S.; Levander, I.; Fox, S.; Sepaniak, M.; Nilsson, S., Airborne Chemistry Coupled to Raman Spectroscopy. *Anal. Chem.* **2003,** *75*, 2177-2180.

23. Santesson, S.; Cedergren-Zeppezauer, E. S.; Johansson, T.; Laurell, T.; Nilsson, J.; Nilsson, S., Screening of Nucleation Conditions using Levitated Drops for Protein Crystallization. *Anal. Chem.* **2003,** *75*, 1733-1740.

24. Santesson, S.; Andersson, M.; Degerman, E.; Johansson, T.; Nilsson, J.; Nilsson, S., Airborne Cell Analysis. *Anal. Chem.* **2000,** *72*, 3412-3418.

25. Santesson, S.; Ramirez, I. B.-R.; Viberg, P.; Jergil, B.; Nilsson, S., Affinity Two-Phase Partitioning in Acoustically Levitated Drops. *Anal. Chem.* **2004,** *76*, 303-308.

26. Merchuk, J. C.; Andrews, B. A.; Asenjo, J. A., Aqueous Two-Phase Systems for Protein Separation: Studies on Phase Inversion. *J. Chromatogr., B: Anal. Technol. Biomed. Life Sci.* **1998,** *711*, 285-293.

Chapter 5

Shrinking Microdroplets Assists Metamorphoses of The Nanoparticle Assemblies

This chapter demonstrates self-assembly of cadmium telluride nanoparticles (CdTe NPs) in the shrinking microenvironment described in Chapter 4. Terminal assemblies of nanoparticles are particularly convenient for controlling the size and morphology of these superstructures. As most techniques for controlling NP assembly have focused upon altering particle properties in static bulk solutions, little attention has been paid to the alternation of micro-scale NP environment. Here we report and characterize the spontaneous assembly of CdTe NPs within an aqueous micro-droplet suspended in oil. The gradual diffusion of the aqueous solution into the surrounding oil medium results in an overall shrinking of the microdroplet, and a concomitant agglomeration of NPs into branched assemblies that evolve in size from ~50 µm to ~1000 µm. Here, the fractal dimension of NP assemblies increases from ~1.7 to ~1.9 through dentritic evolution. High surface-to-volume ratio of the microdroplet can efficiently absorb soybean oil constituents and assist the dentritic evolution. The obtained NP dendrites can be further altered morphologically by illumination with ambient light, resulting in their disassembly. The use of this platform for the study of NP aggregation sheds light on the role of NP environment and presents a unique opportunity to explore NP assembly along with chemical modification.

5.1 Introduction

Processes underlying the self-assembly of nanoparticles (NPs) can yield complex superstructures comprised of semiconductor or metallic materials. [1, 2] Since the process is governed by inter-particle attraction and repulsion,[3, 4] these superstructures can be tailored by manipulating the attractive and repulsive interactions. Modification of particle properties has been vigorously studied for the manipulation of NP assemblies.[5, 6] The formulation of surface stabilizers, and the ratio of surface stabilizer to NPs, for example, can affect these interactions and the nature of the resulting structures.[7] Semiconductor NPs have received much attention in particular for being central to flexible electronics and green energy devices. CdTe NPs were shown to form assemblies with an exceptional variety of geometrical forms ranging from nanowires[8] and sheets[9], to twisted helices[10] depending upon the surface properties of the NPs. The manipulation of assembly based on NP surface properties has less structural flexibility once assembled in static bulk conditions and requires laborious NP synthesis every time the surface properties need to be modified.

Meanwhile, alternation of the micro-scale environment can also affect the resulting assemblies. Recent studies have also reported on techniques triggering self-assembly of semiconductor NPs at liquid-liquid[11-14] or air-substrate[15-20] interfaces. Interestingly, superstructures with highly branched[21-23] and hedgehog-like[24] morphologies obtained at these interfaces revealed chemical and optical properties distinct from those recorded by more traditional methods of assembly. Despite their advantages, these techniques often require the careful control of experimental conditions, and yield assemblies that remain structurally heterogeneous. The semiconductor materials with highly branched dentritic architecture are expected to have larger surface area to collect the light and thus more efficient photo-harvesting and photo-catalytic properties.[22, 25-27] Given their morphology strongly affects their properties and colloidal stability, improved yet simple structural control is needed.

Here, we describe adaptation of a slow and steady droplet dehydration system comprised of aqueous droplets suspended in certain oils[28-30] for the self-assembly of CdTe NPs controlled by the liquid-liquid microenvironment. Our approach, requiring no external control of the dehydration process, is simple and can easily be adapted for specific types of NPs. As a preliminary demonstration of this method, water droplets containing CdTe NPs were placed in an oil 'bath' where the droplets underwent a steady dehydration that resulted in the formation of complex NP assemblies. We have observed dramatic changes in the morphology of NP assemblies under different conditions, and have compared these assemblies to those produced by similar processes in bulk. We characterize the structural and chemical properties of NPs, simulate the NPs assembly in a droplet dehydrating condition, and alter the droplet environment to trigger metamorphoses of the NPs assemblies.

5.2 Materials and Methods

Materials

All materials were purchased from commercial sources. Fluorinert FC-40, soybean oil, hexadecane, deionized water, MeOH, NaOH, HCl, NaCl, thioglycolic acid (TGA) were from Sigma-Aldrich; 35 mm x 10 mm disposable petri dishes were from Fisher Scientific; Grids with ultra thin carbon film on holey carbon film support for transmission electron microscope (TEM) measurement were from Ted Pella; Si wafers for atomic force microscope (AFM) and scanning electron microscope (SEM) measurements were from University Wafer; Plain glass microscope slides for confocal microscope measurement were from Corning; Al_2Te_3 was from CERAC Inc.

Preparation of CdTe NPs

An aqueous dispersion of CdTe NPs stabilized with TGA (TGA / Cd^{2+} = 1.2) was synthesized as previously reported.[31, 32] The orange-ish NP dispersion with a luminescence peak around 550 nm was obtained. 100 μL of the CdTe NPs dispersion was precipitated by 100 μL of MeOH and centrifuged for 30 min at 10,000 rpm. CdTe precipitates were resuspended in DI-water at pH 9 (titrated by addition of NaOH) at a final concentration around ~10 nM. 2.5 mL FC-40 and 3 mL soybean oil (dehydrating oil) or hexadecane (inert oil) were poured into a petri dish. A droplet of the CdTe NPs solution (~ 150 nL) was released by a micropipette at FC-40-soybean oil interface or FC-40-hexadecane interface in the petri dish. The CdTe bulk solution and the water droplet containing CdTe NPs were incubated at the room temperature (25 °C) under dark environment for the following characterization.

Time-lapse microscopy of droplet shrinking

The water droplet containing CdTe NPs at FC-40-soybean oil or FC-40-hexadecane interface was continuously monitored. The cross section of the droplet viewed from the bottom was measured using an optical microscope (TE-300, Nikon) and analyzed by ImageJ. Three sets of measurements were averaged and expressed as a mean ± standard deviation. The rate of change of area, A, is given by Equation 1:

$$\frac{dA}{dt} = -\frac{8\pi M_w D_{w,o}(C_{sat} - C_{ref})}{\rho_w} \quad (1)$$

Where M_w is the molecular weight of water, $D_{w,o}$ is the diffusion coefficient of water in soybean oil, ρ_w is the density of water, and C_{sat} and C_{ref} are the saturation concentration of water in oil and the concentration far away from the droplet, respectively. Detailed explanation can be found elsewhere.[28, 29]

The droplet maintains spherical shape at FC40-soybean oil interface and thus we can estimate the volume of the droplet from the optical image. We can simply calculate concentration as:

$$M_f = \left(\frac{V_0}{V_f}\right) M_i \quad (2)$$

Where M_i and M_f are the initial and final concentration and V_f is the volume when the shrinking rate is significantly reduced at Day-3.

Computational modeling of NP concentration gradient formation during dehydration

The COMSOL multiphysics software package (v 5.1) was used to investigate and model regional changes in NP concentration within the water droplet as a function of incubation time at the FC-40-soybean oil interface. Simulated distribution data was generated and analyzed for the time period ranging from 0 to 72 hours.

The fractal dimension of CdTe assemblies

The fractal dimensions were obtained by BoneJ (a free imageJ plugin) based on box-counting method[33] from the representative SEM images of the CdTe assemblies. Three sets of images were averaged with standard deviation.

Characterization of CdTe assemblies

The bulk solution and water droplets containing CdTe NPs at FC-40-soybean oil interface or FC-40-hexadecane interface were incubated under dark condition for 1-7 days and cast onto substrates for AFM, confocal microscope, SEM, and TEM imaging.

AFM measurement

CdTe NPs assemblies at Day-3 cast onto Si wafers were imaged by AFM (Dimension Icon, Veeco) in ScanAsyst mode and the images were processed by Nanoscope (Veeco).

SEM and EDX measurement

CdTe NPs assemblies at Day-1-7 cast onto Si wafers were analyzed by SEM (Nova 200 NanoLab, FEI) operated at 5-15 kV and the images were processed by ImageJ. Au deposition was carried out prior to SEM imaging in order to increase phase contrast. For EDX measurement, the CdTe assemblies were imaged and EDX spectra were collected without Au deposition. The EDX spectra were analyzed by NOVA software.

TEM measurement

CdTe NPs assemblies at Day-3 cast onto TEM grids were imaged by TEM (JEOL 3011) operated at 300kV including electron diffraction in the selected area and the images were processed by ImageJ.

Confocal measurement

CdTe NPs assemblies at t = 0 and Day-3 cast onto glass slides were scanned by a confocal microscope (Nikon-A1, Nikon) with 480 nm excitation wavelength and 540 nm emission wavelength. Fluorescent spectra at the area of interest were collected by Lambda scanning with 480 nm excitation wavelength. For *in situ* droplet measurement, the water droplet in soybean oil placed on the glass substrate (25 mm petridish with a glass slide on the bottom specialized for confocal imaging) was continuously monitored and fluorescent spectra were collected by Lambda scanning until Day-3.

External alternation of the NP microenrionment

Bulk NP assembly with soybean oil-derived additives

DI-water and soybean oil (water : oil = 4:1 and 1:4) were vigorously mixed and incubated for phase separation over night. The water-phase was collected and used for the CdTe NPs resuspension. DI-water solutions with glycerol (0.1 v/v%) or linoleic acid (0.1 v/v%) were used for the NPs resuspension. The CdTe assemblies at Day-3 in the soluitons were imaged by SEM.

Compaction of CdTe assemblies by adding salts

The CdTe bulk solution was prepared with 500 mM NaCl solution (pH 9.0) and the droplets from the bulk solution were incubated at FC-40-soybean oil interface and characterized by SEM.

De-assembly of CdTe assemblies by irradiating light

The droplets contacting CdTe NPs were exposed to the ambient light at Day-3 for 24 hours. Additionally, the droplets were incubated at FC-40-soybean oil interface over 5 days when the ambient light irradiated at Day-0, 2, 3, or 4. The assemblies were analyzed by SEM.

5.3 Results and Discussion

5.3.1 Dentritic NPs assemblies

Water droplets containing CdTe NPs shrink from dehydration at FC-40-soybean oil interface as a function of time at a constant rate (1.4 $\mu m^2 / s$) until t = 72 hours (Figure 5.1). The shrinking rate is dramatically reduced (0.051 $\mu m^2 / s$) after t = 72 hours. SEM images reveal a distinct evolution of the CdTe NP assemblies over time (Figure 5.2). The NPs in the droplets evolve from compact structures (compact dendrites) into extended and branched structures (extended dendrites) over the course of three days (Figure 5.2A-C), while a majority of the NPs in the bulk solution form the compact dendrites during the same three-day period (Figure 5.2E and F). The approximate fractal dimension of the extended dentritic structures illustrate higher dimension (D = 1.9±0.04) compared to the compact dentritic structures (D = 1.7±0.08). The extended dentritic structures remain stably after Day-3, in a manner that coincides with the steep reduction of the shrinking rate (Figure 5.2D). Meanwhile the NPs structure in the bulk solution shows no significant morphological change throughout the experiment period (Figure 5.2G). We hypothesize that the

CdTe NPs complete the assembly at Day-3 and, as reported previously (ref 28-30), the resulting structures inhibit the flux of water molecules at the droplet interface. Note that, as previously reported (ref 10), the straight ribbons of the NPs in the bulk solution were observed when increasing the NPs concentration up to 100-fold (Figure 5.9A). However, the high initial concentration gave rise to random aggregation of the NPs in droplets at Day-3 (Figure 5.9B). The concentration producing the straight ribbons may be too high for the dehydration system.

5.3.2 Concentration of NPs in the microdroplet

Simulation of the time-lapse concentration change of NPs in the droplet by COMSOL confirm that the homogeneous distribution of NPs within the droplet at t = 0 (Figure 5.12A), verified experimentally (Figure 5.15A), and the gradual concentration of particles over 72 hours (Figure 5.12B-C). After 72 hours, the NPs are predicted to completely occupy the droplet periphery (Figure 5.12C). These observations are consistent with the *in situ* droplet imaging data (Figure 5.15B) and with the time point when droplet dehydration rate significantly dropped after 72 hours (Figure 5.1). In contrast, the simulation in hexadecane shows the homogeneous distribution of NPs over 72 hours (Figure 5.13C). Given those results, we assumed at first that the dentritic evolution was attributed to the increased CdTe NPs concentration due to dehydration. We estimated the final concentration from the droplet image and it was about eight times higher than the initial concentration (see Methods). To prove this assumption, the NPs solution was adjusted to the higher concentration and the NPs droplet incubated at an FC-40-hexadecane interface; the shrinking rate is 0.10 $\mu m^2 / s$, one order of magnitude slower than the shrinking rate for droplets in soybean oil (Fig 5.1: open circle). The NPs assemblies formed in droplets dispersed in hexadecane mostly formed the compact dendrites (Figure 5.2H and I). The result indicates that the dentritic evolution depends on the shrinking microenvironment rate rather than solely on increased NP concentration.

5.3.3 Structural characterization of compact and extended CdTe dendrites

To understand the basis of these NPs assemblies, we characterized the assemblies by AFM, TEM, EDX, and confocal imaging. AFM images reveal that the compact dendrites are ~10 μm in size with ~1 μm height (Figure 5.3A) while the extended dendrites have ~10 μm core and mm-scale branches with ~1 μm height (Figure 5.3B). TEM images of the dentritic structures show that the compact and extended dendrites are composed of CdTe and CdS where the lattice spacing for assembled NPs was 0.38 nm (CdTe) and 0.34 nm (CdS), respectively (Figure 5.4). Selected-area electron diffraction (SAED) patterns of the dendrites demonstrate the presence of characteristic diffraction patterns for both CdTe (111) (d = 0.74 nm) and (220) (d = 0.45 nm), and CdS (111) (d = 0.66 nm) and (200) (d = 0.57 nm) planes. It should be noted that Te oxidation occurs in dark environments and completes within 24 hours in the bulk solution, as previously reported (ref 10). The exchange of Te and S from TGA would occur as Te oxidation proceeds. EDX data show that the compact and extended dendrites are a mixture of CdTe and CdS where Cd : Te : S is 45 : 28 : 27 for the compact dendrite and 42 : 40 : 18 for the extended dendrites, respectively (Figure 5.5 and Figure 5.10). The data suggest that the compact dentritic assemblies have nearly the same amount of Te and S whereas the dendrites have different amounts of the two chemical species. The observed differential amount of Te and S can be explained by the fact that the total amount of oxygen in the droplet solution is smaller than the amount in the bulk solution, which may prevents Te oxidation during the dentritic evolution.

5.3.4 Optical characterization of compact and extended CdTe dendrites

In addition to the structural differences between the compact and extended dendrites, confocal laser scanning microscopy and UV/VIS spectroscopy reveal distinct optical properties. The assemblies in bulk and in the droplet individually retain the fluorescence (Figure 5.6). The fluorescence spectrum of the extended dendrites exhibits a distinct blue shift (l_{em} = 515 nm), whereas the spectrum of the compact dendrite shows a slight red shift (l_{em} = 555 nm) compared to the as-prepared CdTe solution (l_{em} = 550 nm) (Figure 5.11A). The previously reported NP dentritic structures showed only red shift (ref 22 and 23) and, to the best of our knowledge, this is the first observation of blue shifts in dentritic structures. Given that the compact dendrite that has nearly equal amount to CdTe and CdS shows no blue shift, the different amounts of CdTe and CdS along with the radially elongated assembly of the NPs may increase the interparticle distance and weaken the electronic coupling among NPs, thus leading to the blue shift. Additionally, we conducted *in situ* droplet imaging through Day-3 in soybean oil. At t = 0, the droplet shows homogeneously distributed brightness, indicating that the CdTe NPs are well dispersed (Figure 5.15A). Some structures appear and gradually grow in the droplet after Day-1 (Figure 5.15B). The fluorescent spectrum of the droplet exhibits significant blue shift after Day-1 (Figure 5.11B). The observed morphology change in the droplet coincident with the blue shift after Day-1 is consistent with the observed dentritic evolution of the NPs in the droplet in soybean oil. In contrast, such optical properties were not confirmed in the bulk NPs solution by UV/Vis spectroscopy (Figure 5.11C).

5.3.5 Constituents of soybean oil transferred in a droplet affecting CdTe self-assembly

The nonadditivity of van der Waals attraction, electrostatic repulsion, hydrophobicity, and other interactions controls collective behavior of NPs.[34] We hypothesized that the nonadditivity might somehow change upon dehydration where some constituents of soybean oil involve the transition from compact to extended dendrites and performed bulk NPs assembly using water containing soybean oil-derived constituents (Figure 5.7). The NPs assemblies collected in the water phase of water-soybean oil mixtures (water : oil = 1:4 and 4:1) formed dendrites with residual oil spots and extended as the oil proportion increased (Figure 5.7A and B). These data imply that oil constituents transferred into the water phase may assist formation of extended dendrites. Next, glycerol and linoleic acid, the main constituents of soybean oil, were added to DI-water and incubated with the NPs. Interestingly, linoleic acid-containing solutions (0.1 v/v%) gave transitional dendrites while glycerol-containing solutions (0.1 v/v%) resulted in dispersed NP aggregates (Figure 5.7D and E). We assume that impurities such as dissolved fatty acids from soybean oil may attach on the NP surface, hinder particle interactions by steric hindrance, and help extension of the compact dendrites. We also observed that the dispersed microdroplets of the oil or fatty acid in the water-phase limits uniform dentritic formation due to oil contamination. We note that the shrinking microdroplet environment gradually increases the surface-to-volume ratio that can facilitate the impurity absorption from soybean oil while minimizing oil contamination and produce larger dendrites in contrast to the bulk water/oil mixture system.

5.3.6 Influence of interparticle interaction on CdTe self-assembly

Interparticle interaction is a key element that governs overall morphology of NP assembly and alternation of the micro-scale NPs assembly environment can also affect the interaction. To study the effect of the parameters on assembly, we hypothesize that (1) increased ionic strength may reduce the interparticle repulsion – thereby shrinking the assembled NP structures; and (2) that ambient light can alter the interparticle attraction by triggering photo-oxidation of the NP surface during NP evolution. To change the interplay between NPs, we (1) added salts or (2) irradiated the droplets with ambient light during NP evolution. SEM images in the presence of NaCl illustrate compact assemblies in bulk and in droplets (Figure 5.8A). This result confirms that the increased ionic strength triggered the shrinkage of the assemblies. Meanwhile, we irradiated with ambient light at different time points (Figure 5.8B). We observed degradation of the dentritic structures regardless of the timing when the irradiation was performed (Figure 5.14). We hypothesize that ambient light causes surface oxidation of the NPs, which results in loss of the TGA stabilizers, a concomitant increase in interparticle repulsion, and the ultimate disassembly of structures. These findings together confirm that interparticle interaction parameters altered by the NPs assembly environment influence NP evolution and dynamically change their morphology.

5.4 Conclusions

In this work, soybean oil-mediated slow and continuous dehydration of CdTe NP-containing droplets transformed compact dendrites into extended dendrites at Day-3. The dentritic structure retained after Day-3 and showed uniform distribution. The dendrites have different chemical properties and distinct optical properties compared with the NP assemblies in the bulk solution. The dynamic morphological change of the CdTe assemblies appears to rely on a delicate balance of interparticle interactions that evolve over time. Dissolved constituents of soybean oil in the microdroplet may increase the interparticle repulsion and helps the dentritic evolution. Increasing interparticle interactions by increasing ionic strength caused compaction of the assemblies whereas reducing interparticle attraction by irradiation with light triggered NP dis-assembly. The data demonstrate that the micro-scale NP environment can alter the NPs assembly patterns without laborious particle modification. The experimental set up is simple and should be adaptable for modulating the self-assembly of a large range of semiconductive NPs. The semiconductive dendrites with high fractal dimension and large surface-area have potential as light-harvesting materials. Metamorphoses of such NPs can be similarly examined while a further study is necessary to utilize the assembled structures in droplets in photo-harvesting application.

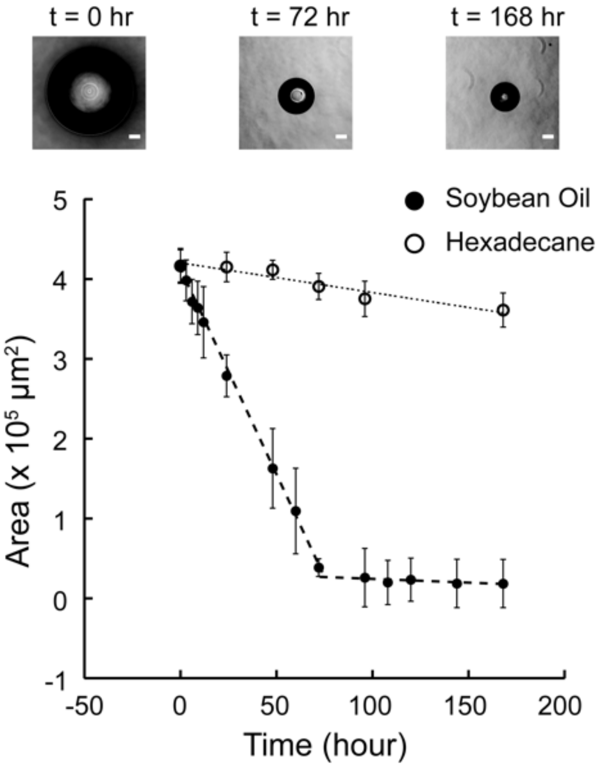

Figure 5.1. Time-lapse droplet shrinking of a DI-water solution containing CdTe. The droplets were monitored over 7 days in soybean oil (closed circle) and hexadecane (open circle), respectively. Equation 1 was fitted into the plots (dotted line). Scale bar 100 μm.

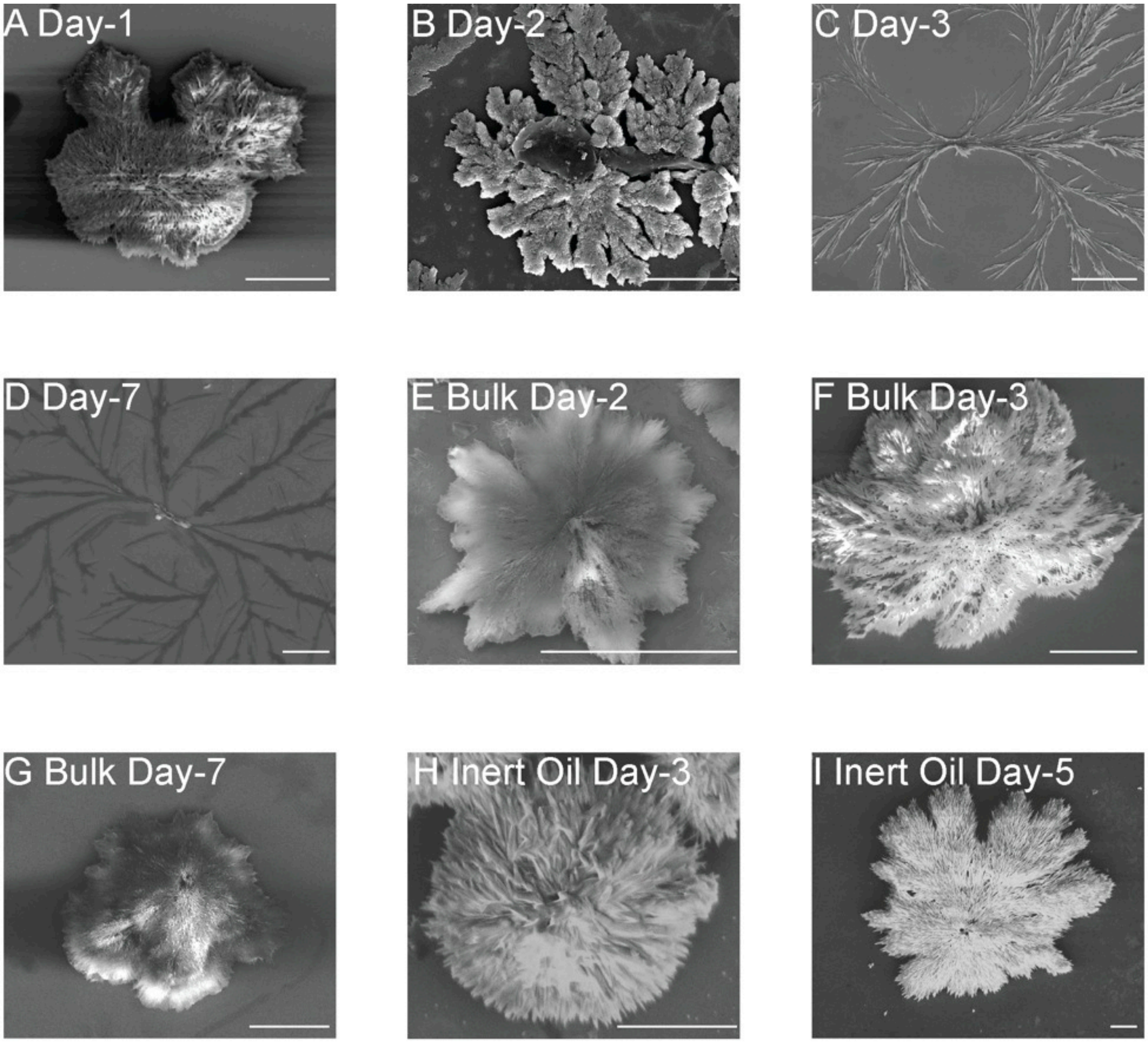

Figure 5.2. SEM images of CdTe assemblies. The droplets containing CdTe in soybean oil at (A) Day-1, (B) Day-2, (C) Day-3, and (D) Day-7. The bulk solution of CdTe at (E) Day-2, (F) Day-3, and (G) Day-7. The droplet containing CdTe in hexadecane at (H) Day-3 and (I) Day-5. Scale bar 10 μm.

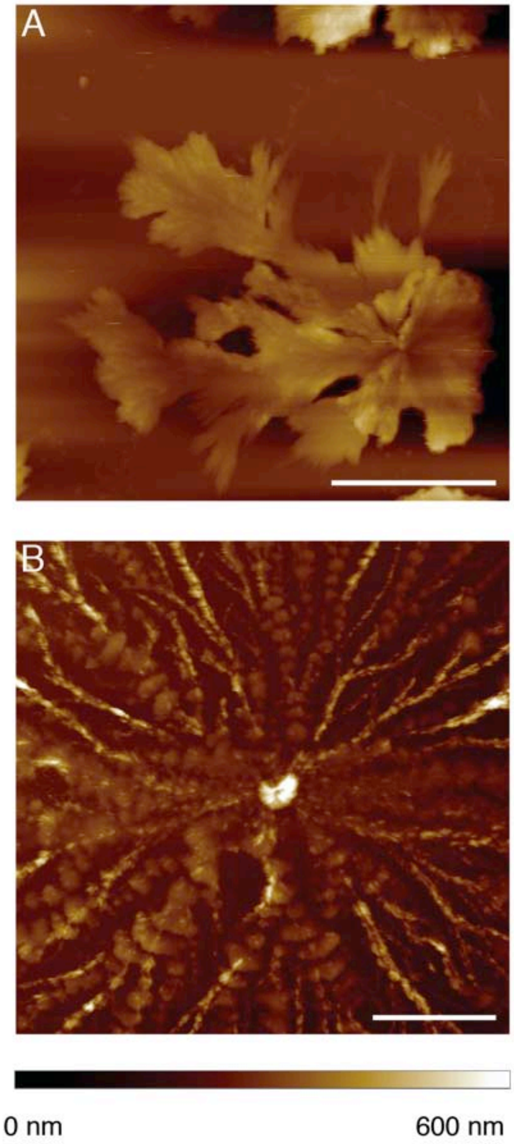

Figure 5.3. AFM image of (A) the compact dendrite (15 μm x 15 μm) and (B) the extended dendrite (40 μm x 40 μm). Scale bar (A) 5 μm and (B) 10 μm.

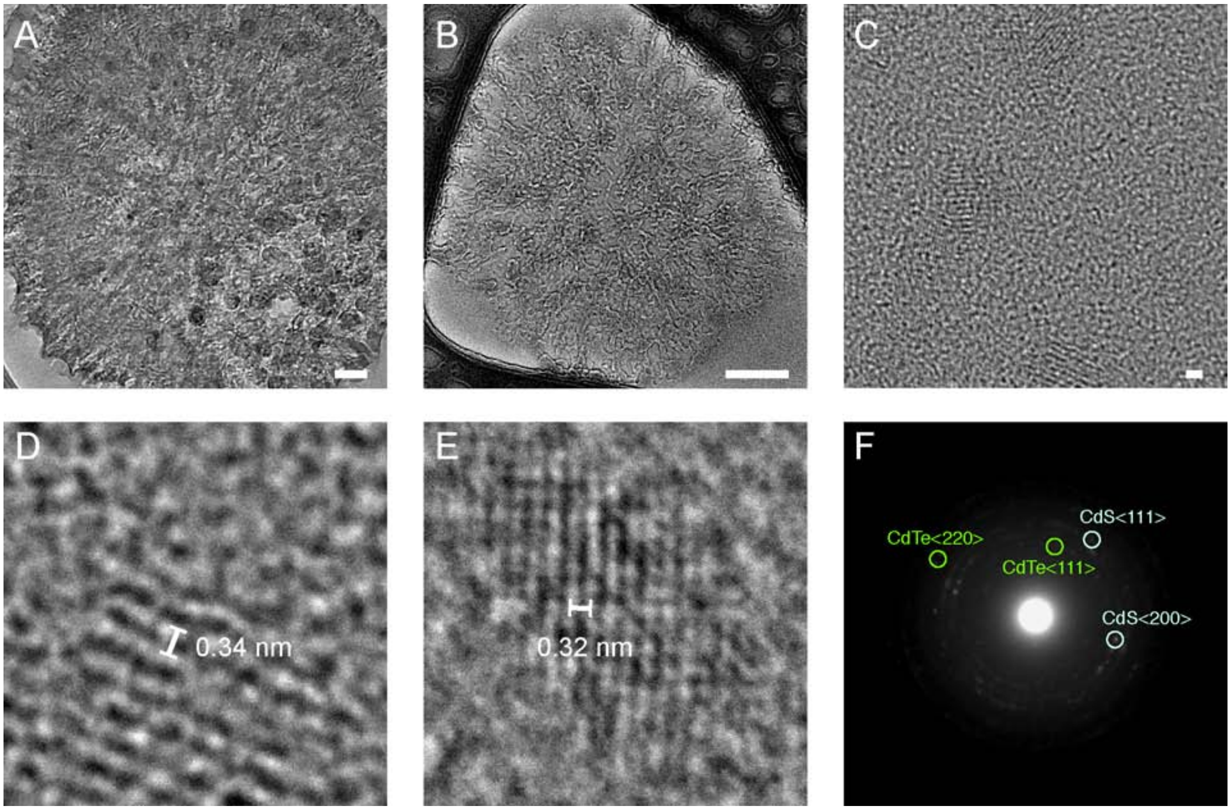

Figure 5.4. TEM image of the CdTe assemblies collected at Day-3. The representative image of CdTe assembly (A) in bulk and (B) in droplets, (C) the lattice image of the extended dendrite, (D) the lattice distance of CdTe, (E) the lattice distance of CdS, and (F) SAED of the extended dendrite. Scale bar (A) and (B) 100 nm, and (C) 1 nm.

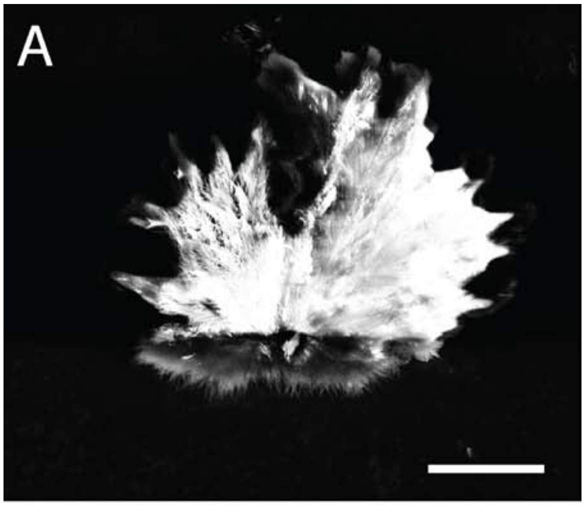

Compact dendrite at Day-3
Cd : Te : S = 45 : 28 : 27

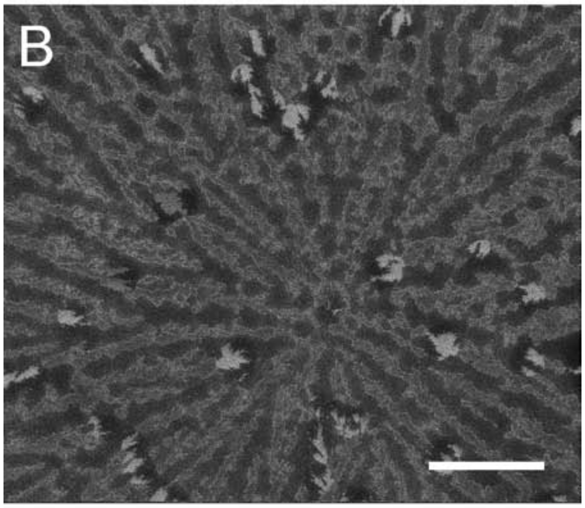

Extended dendrite at Day-3
Cd : Te : S = 42 : 40 : 18

Figure 5.5. EDX image of (A) the compact dendrite and (B) the extended dendrite collected at Day-3. Scale bar 10 μm.

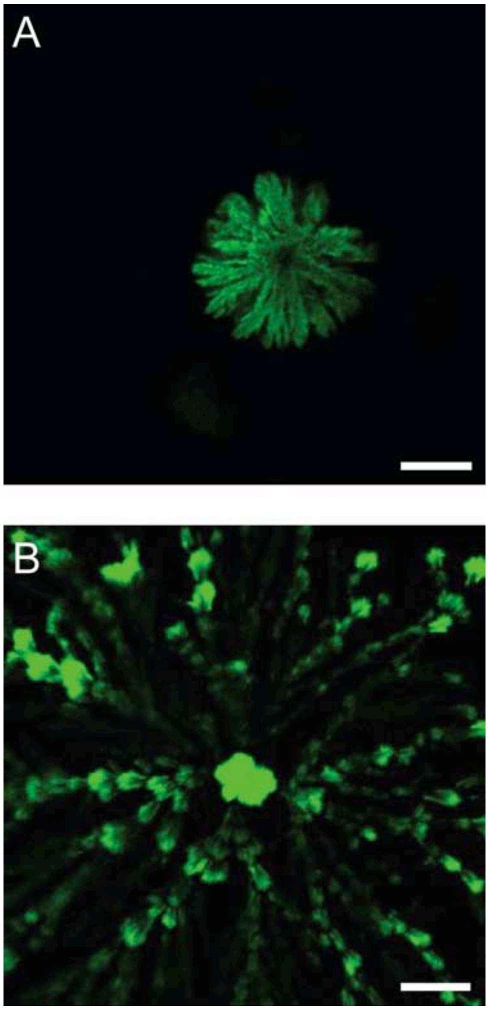

Figure 5.6. Confocal microscopy images of the (A) the compact dendrite and (B) the extended dendrite collected at Day-3. Scale bar 10 µm.

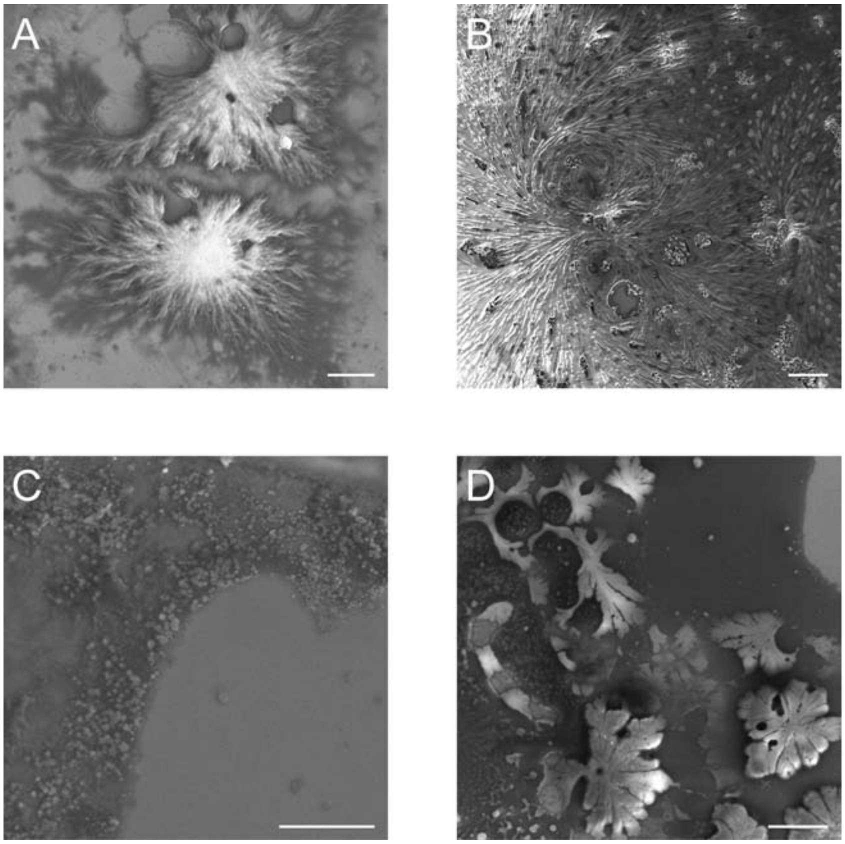

Figure 5.7. SEM images of the NPs assemblies at Day-3 with soybean oil constituents. The NPs assemblies collected from the water phase of water and soybean oil mixtures: water : oil = (A) 4 : 1 and (B) 1 : 4. The NPs assemblies collected from 0.1% glycerol and 0.1% linoleic acid. Scale bar 10 μm.

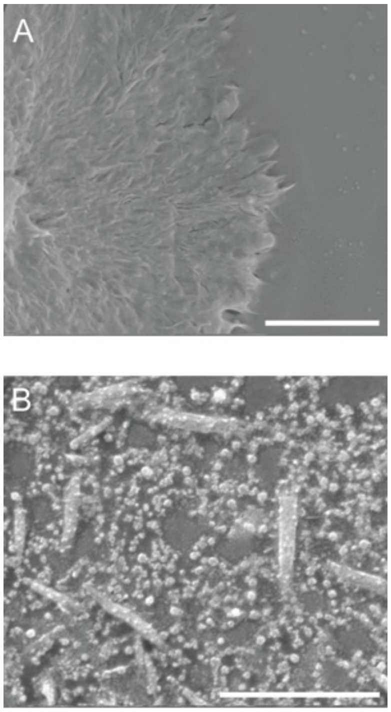

Figure 5.8. SEM images of the NPs assemblies in the droplets collected at Day-3 in the presence of salt and light. The representative image of the CdTe assembly under (A) 500 mM NaCl and (B) ambient light. Scale bars 3 µm.

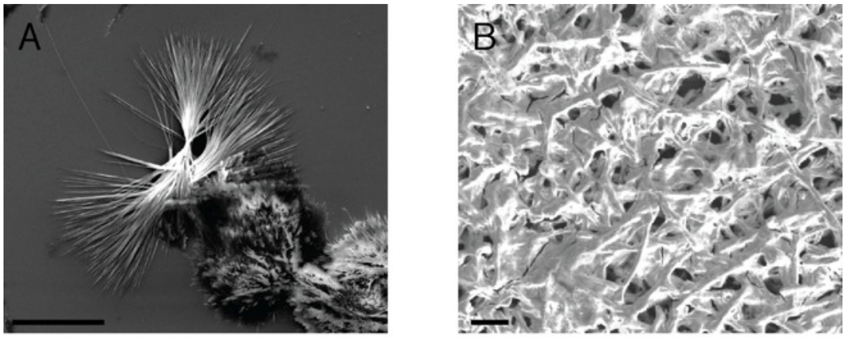

Figure 5.9. SEM image of the CdTe assemblies prepared by the 100-fold high concentration: (A) bulk and (B) droplet solution at Day-3. Scale bar 5 μm.

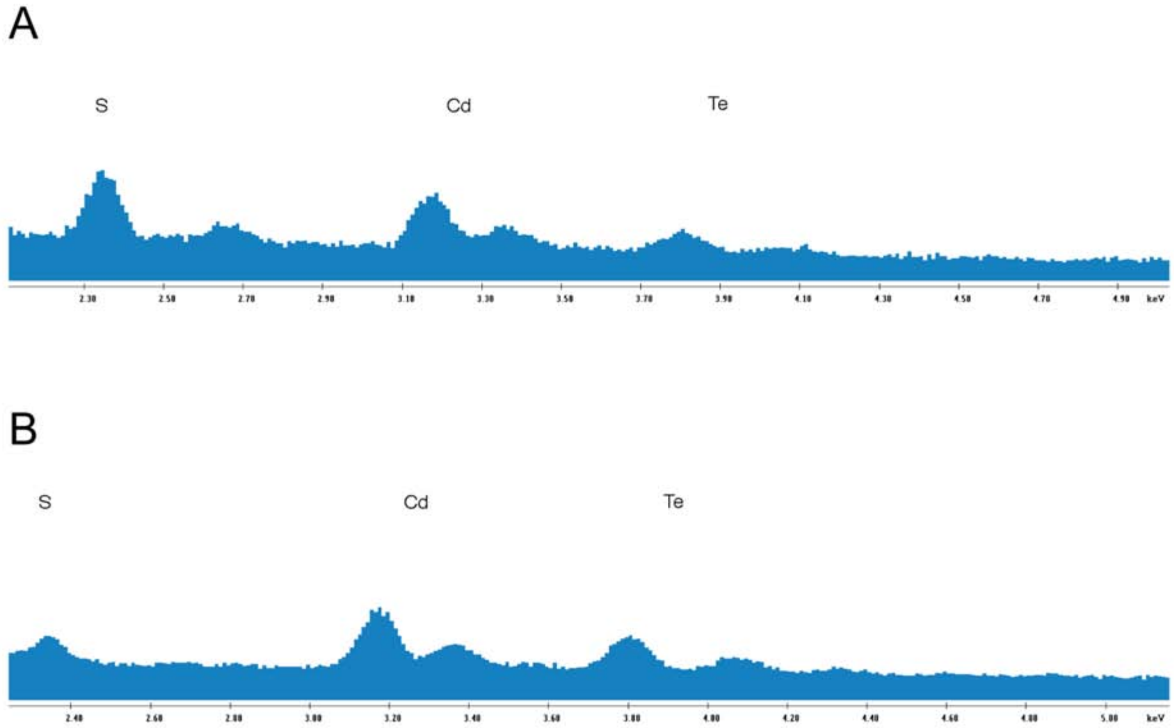

Figure 5.10. EDX data of the CdTe assemblies collected at Day-3. (A) the compact dendrite and (B) the extended dendrite.

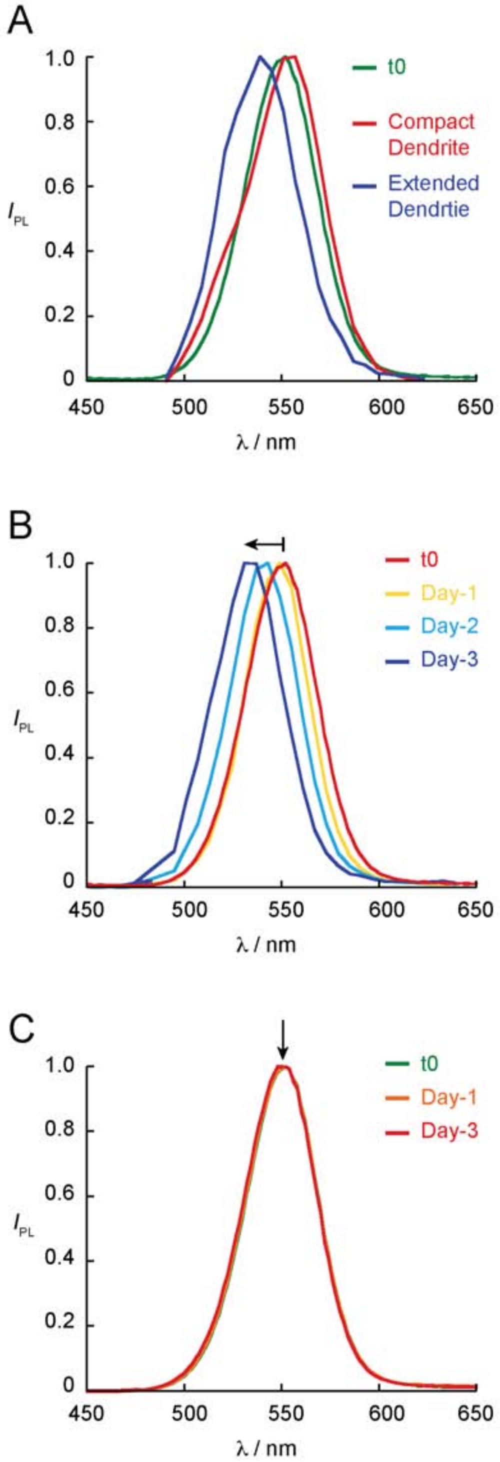

Figure 5.11. Fluorescent spectra of the CdTe assembled structures. (A) Lambda scanned spectra of the compact and extended dentritic structures collected at Day-3. Fluorescent spectra of (B) the droplet solution and (C) the bulk solution over three days.

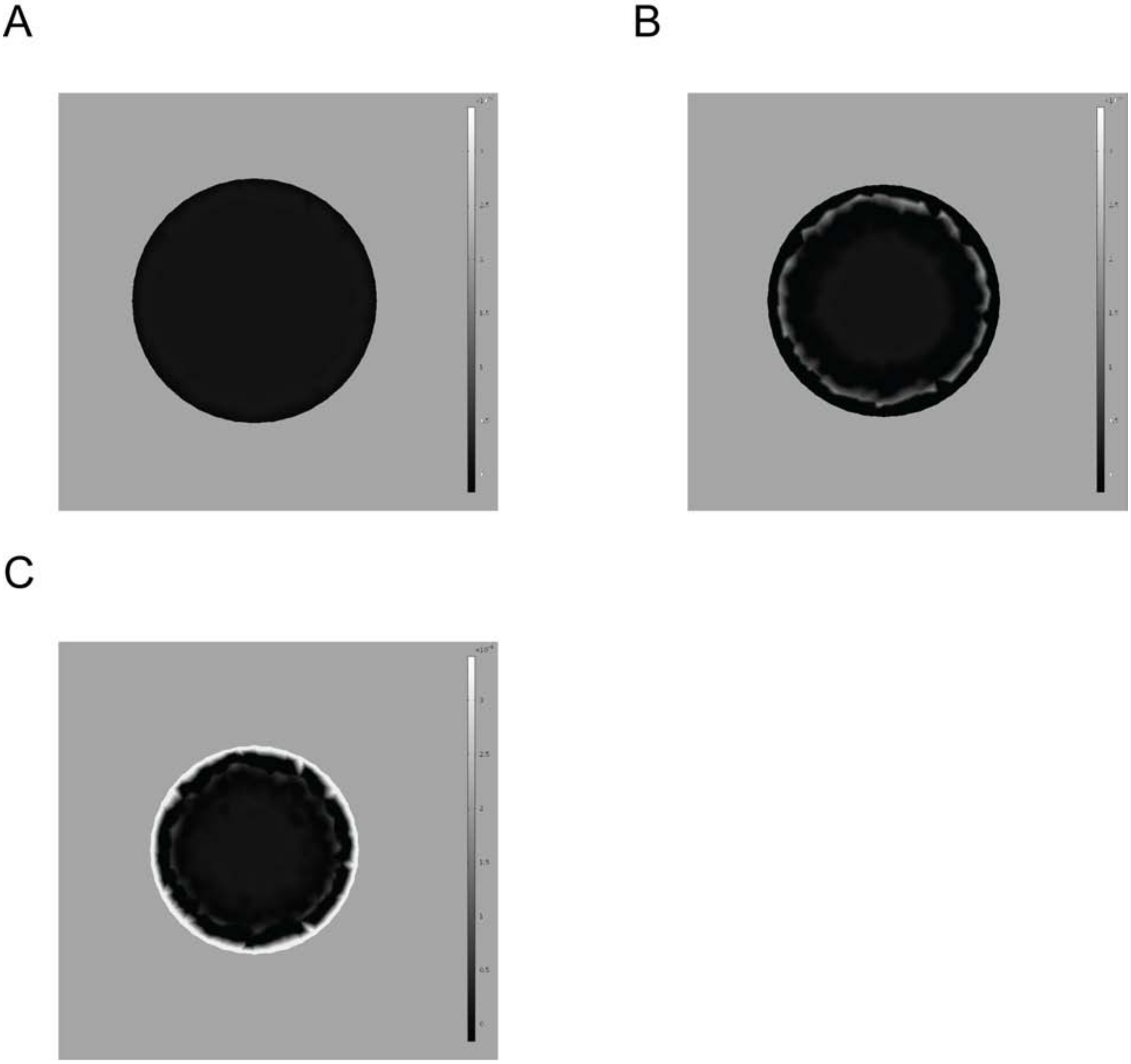

Figure 5.12. A computational model of droplet dehydration in soybean oil at (A) t = 0, (B) t = 24 hrs, (C) t = 72 hrs.

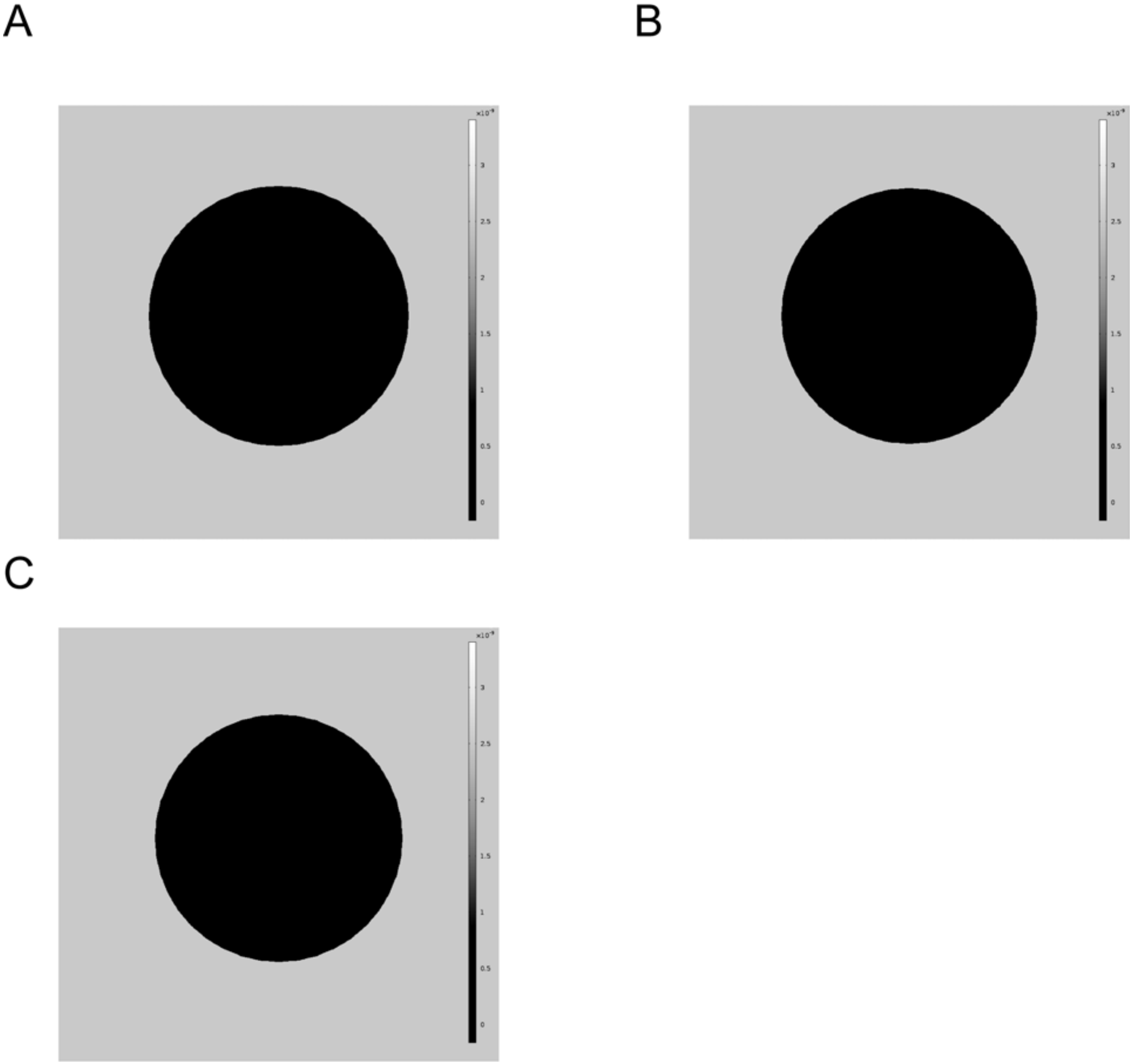

Figure 5.13. A computational model of droplet dehydration in hexadecane at (A) t = 0, (B) t = 24 hrs, (C) t = 72 hrs.

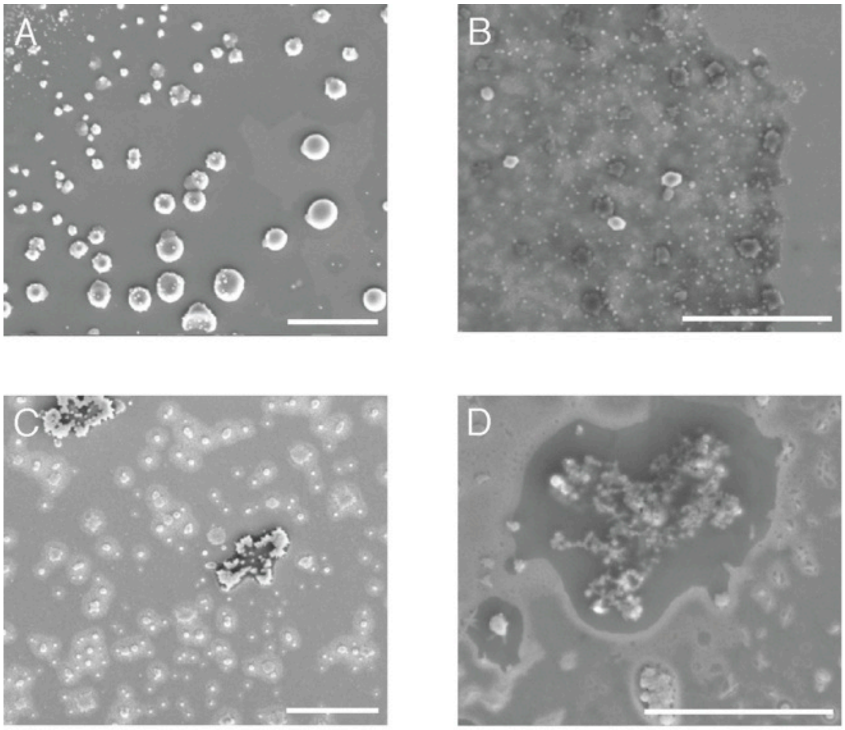

Figure 5.14. SEM images of the NPs droplets irradiated at different time points over 5 days. (A) irradiated at Day-4, (B) irradiated at Day-3, (C) irradiated at Day-2, and (D) irradiated at Day-0. Scale bar 5 μm.

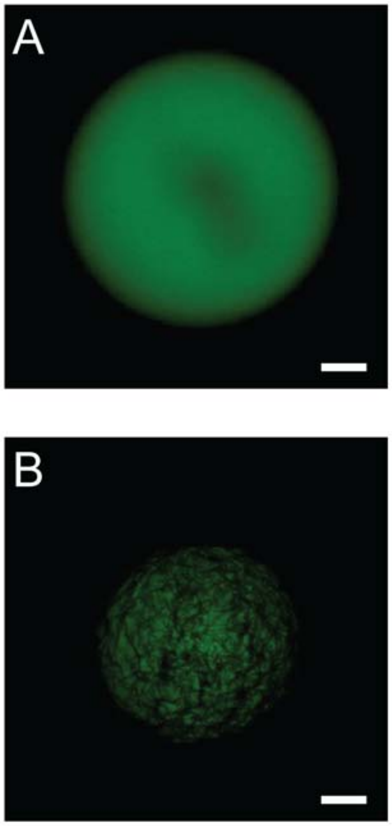

Figure 5.15. Reconfigured 3D z-stack images of the CdTe droplets dehydrated on a glass surface at (A) t = 0 and (B) t = Day-3. Scale bar 100 µm.

5.5 References

1. Nie, Z.; Petukhova, A.; Kumacheva, E., Properties and Emerging Applications of Self-Assembled Structures Made from Inorganic Nanoparticles. *Nat. Nanotechnol.* **2009,** *5*, 15-25.

2. Grzelczak, M.; Vermant, J.; Furst, E. M.; Liz-Marzán, L. M., Directed Self-Assembly of Nanoparticles. *ACS Nano* **2010,** *4*, 3591-3605.

3. Whitesides, G. M.; Grzybowski, B., Self-Assembly at All Scales. *Science* **2002,** *295*, 2418-2421.

4. Whitesides, G. M.; Boncheva, M., Beyond Molecules: Self-Assembly of Mesoscopic and Macroscopic Components. *Proc. Natl. Acad. Sci. U. S. A.* **2002,** *99*, 4769-4774.

5. Park, S. Y.; Lytton-Jean, A. K.; Lee, B.; Weigand, S.; Schatz, G. C.; Mirkin, C. A., DNA-Programmable Nanoparticle Crystallization. *Nature* **2008,** *451*, 553-556.

6. Kovalenko, M. V.; Scheele, M.; Talapin, D. V., Colloidal Nanocrystals with Molecular Metal Chalcogenide Surface Ligands. *Science* **2009,** *324*, 1417-1420.

7. Yaroslavov, A. A.; Sinani, V. A.; Efimova, A. A.; Yaroslavova, E. G.; Rakhnyanskaya, A. A.; Ermakov, Y. A.; Kotov, N. A., What is The Effective Charge of TGA-Stabilized CdTe Nanocolloids? *J. Am. Chem. Soc.* **2005,** *127*, 7322-7323.

8. Tang, Z.; Kotov, N. A.; Giersig, M., Spontaneous Organization of Single CdTe Nanoparticles into Luminescent Nanowires. *Science* **2002,** *297*, 237-240.

9. Tang, Z.; Zhang, Z.; Wang, Y.; Glotzer, S. C.; Kotov, N. A., Self-Assembly of CdTe Nanocrystals into Free-Floating Sheets. *Science* **2006,** *314*, 274-278.

10. Srivastava, S.; Santos, A.; Critchley, K.; Kim, K.-S.; Podsiadlo, P.; Sun, K.; Lee, J.; Xu, C.; Lilly, G. D.; Glotzer, S. C., Light-Controlled Self-Assembly of Semiconductor Nanoparticles into Twisted Ribbons. *Science* **2010,** *327*, 1355-1359.

11. Lin, Y.; Böker, A.; Skaff, H.; Cookson, D.; Dinsmore, A.; Emrick, T.; Russell, T. P., Nanoparticle Assembly at Fluid Interfaces: Structure and Dynamics. *Langmuir* **2005,** *21*, 191-194.

12. Lin, Y.; Skaff, H.; Emrick, T.; Dinsmore, A.; Russell, T., Nanoparticle Assembly and Transport at Liquid-Liquid Interfaces. *Science* **2003,** *299*, 226-229.

13. Duan, H.; Wang, D.; Kurth, D. G.; Möhwald, H., Directing Self-Assembly of Nanoparticles at Water/Oil Interfaces. *Angew. Chem. Int. Ed.* **2004,** *43*, 5639-5642.

14. Böker, A.; He, J.; Emrick, T.; Russell, T. P., Self-Assembly of Nanoparticles at Interfaces. *Soft Matter* **2007,** *3*, 1231-1248.

15. Brinker, C. J.; Lu, Y.; Sellinger, A.; Fan, H., Evaporation-Induced Self-Assembly: Nanostructures Made Easy. *Adv. Mater.* **1999,** *11*, 579-585.

16. Bigioni, T. P.; Lin, X.-M.; Nguyen, T. T.; Corwin, E. I.; Witten, T. A.; Jaeger, H. M., Kinetically Driven Self Assembly of Highly Ordered Nanoparticle Monolayers. *Nat. Mater.* **2006,** *5*, 265-270.

17. Chokprasombat, K.; Sirisathitkul, C.; Ratphonsan, P., Liquid-Air Interface Self-Assembly: A Facile Method to Fabricate Long-Range Nanoparticle Monolayers. *Surf. Sci.* **2014,** *621*, 162-167.

18. Pietra, F.; Rabouw, F. T.; Evers, W. H.; Byelov, D. V.; Petukhov, A. V.; Donegá, C. d. M.; Vanmaekelbergh, D., Semiconductor Nanorod Self-Assembly at The Liquid/Air Interface Studied by in situ GISAXS and ex situ TEM. *Nano Lett.* **2012,** *12*, 5515-5523.

19. Rabani, E.; Reichman, D. R.; Geissler, P. L.; Brus, L. E., Drying-Mediated Self-Assembly of Nanoparticles. *Nature* **2003,** *426*, 271-274.

20. Corno, J. A.; Stout, J.; Yang, R.; Gole, J. L., Diffusion-Controlled Self-Assembly and Dendrite Formation in Silver-Seeded Anatase Titania Nanospheres. *J. Phys. Chem. C* **2008,** *112*, 5439-5446.

21. Dong, W.; Li, X.; Shang, L.; Zheng, Y.; Wang, G.; Li, C., Controlled Synthesis and Self-Assembly of Dendrite Patterns of Fe3O4 Nanoparticles. *Nanotechnology* **2009,** *20*, 035601.

22. Sukhanova, A.; Baranov, A. V.; Perova, T. S.; Cohen, J. H.; Nabiev, I., Controlled Self-Assembly of Nanocrystals into Polycrystalline Fluorescent Dendrites with Energy-Transfer Properties. *Angew. Chem. Int. Ed.* **2006,** *45*, 2048-2052.

23. Sun, H.; Wei, H.; Zhang, H.; Ning, Y.; Tang, Y.; Zhai, F.; Yang, B., Self-Assembly of CdTe Nanoparticles into Dendrite Structure: A Microsensor to Hg2+. *Langmuir* **2010,** *27*, 1136-1142.

24. Bahng, J. H.; Yeom, B.; Wang, Y.; Tung, S. O.; Hoff, J. D.; Kotov, N., Anomalous Dispersions of "Hedgehog" Particles. *Nature* **2015,** *517*, 596-599.

25. Klar, T. A.; Franzl, T.; Rogach, A. L.; Feldmann, J., Super-Efficient Exciton Funneling in Layer-by-Layer Semiconductor Nanocrystal Structures. *Adv. Mater.* **2005,** *17*, 769-773.

26. Wargnier, R.; Baranov, A. V.; Maslov, V. G.; Stsiapura, V.; Artemyev, M.; Pluot, M.; Sukhanova, A.; Nabiev, I., Energy Transfer in Aqueous Solutions of Oppositely Charged CdSe/ZnS Core/Shell Quantum Dots and in Quantum Dot-Nanogold Assemblies. *Nano Lett.* **2004,** *4*, 451-457.

27. Li, J.; Cheng, Z.; Liu, M.; Zhang, M.; Hu, M.; Zhang, L.; Jiang, H.; Li, J., Electrospun Dendritic ZnO Nanofibers and Its Photocatalysis Application. *J. Appl. Polym. Sci.* **2015,** *132*.

28. Kojima, T.; Takayama, S., Microscale Determination of Aqueous Two Phase System Binodals by Droplet Dehydration in Oil. *Anal. Chem.* **2013,** *85*, 5213-5218.

29. He, M.; Sun, C.; Chiu, D. T., Concentrating Solutes and Nanoparticles within Individual Aqueous Microdroplets. *Anal. Chem.* **2004,** *76*, 1222-1227.

30. Bajpayee, A.; Edd, J. F.; Chang, A.; Toner, M., Concentration of Glycerol in Aqueous Microdroplets by Selective Removal of Water. *Anal. Chem.* **2010,** *82*, 1288-1291.

31. Rajh, T.; Micic, O. I.; Nozik, A. J., Synthesis and Characterization of Surface-Modified Colloidal Cadmium Telluride Quantum Dots. *J. Phys. Chem.* **1993,** *97*, 11999-12003.

32. Rogach, A.; Katsikas, L.; Kornowski, A.; Su, D.; Eychmüller, A.; Weller, H., Synthesis and Characterization of Thiol-Stabilized CdTe Nanocrystals. *Ber. Bunsen-Ges. Phys. Chem.* **1996,** *100*, 1772-1778.

33. Doube, M.; Ktosowski, M.; Arganda-Carreras, I.; Cordelières, F. P.; Dougherty, R. P.; Jackson, J. S.; Schmid, B.; Hutchinson, J. R.; Shefelbine, S. J., BoneJ: Free and Extensible Bone Image Analysis in ImageJ. *Bone* **2010,** *47*, 1076-1079.

34. Batista, C. A. S.; Larson, R. G.; Kotov, N. A., Nonadditivity of Nanoparticle Interactions. *Science* **2015,** *350*, 1242477.

Chapter 6

Spatio-temporally Regulated Enzyme Reactions in Membrane-Free Compartments Formed in An Aqueous Three Phase System

Spatio-temporal compartmentalization of molecules and bioreactions is an important features of cellular systems. While membrane-bounded multi-compartment bioreaction models are common, much less work has explored the use of membrane-free multi-compartment systems. Given the potential paucity of membrane forming and reorganizing molecules and mechanisms in the primordial soup, formation of membrane-free multi-compartments and exploration of their use in bioreactions and compartment reorganization may provide an alternative mechanism for the evolution of primitive cells. Membrane-free multi-compartments may also have practical applications in biosensing and reactions.

This chapter describes stable membrane-free multi-compartmentalization utilizing an aqueous three phase system that combines a complex coacervate with a commonly used polymeric aqueous two-phase system (ATPS). We hypothesized that complex coacervates made of negatively charged adenosine triphosphate (ATP) and positively charged poly(diallyldimethylammonium chloride) (PDDA) will form additional compartments within an ATPS comprised of dextran (DEX) and polyethylene glycol (PEG) leading to formation of an aqueous three phase system. Indeed, such systems efficiently formed stable, all-aqueous multi-compartment systems. Importantly, the ATP-PDDA coacervates were able to stably partition a variety of proteins and molecules within the aqueous three phase system. Furthermore, such molecules "trapped" within different coacervate compartments could be merged by physical relocation or the contents released on demand by changing the ionic strength (addition of salts), which "dissolves" the coacervate phase. In both cases, the manipulations allow cascade reactions to occur across originally separated compartments. Alternatively, treatment of the multi-compartment aqueous three phase system with dextranase degraded the DEX phase leaving a multi-compartment coacervate-PEG two phase system. While the demonstrations are simple and not necessarily focused on ingredients from the primordial soup, we believe the spatio-temporal regulation of reactions in non-membrane bounded multi-compartment systems are interesting and warrant further investigation.

6.1 Introduction

The minimal living cell (protocell), a proposed precursor of modern cells, is described as a single-compartment construct.[1] While a single compartment can collect molecules to maintain minimal cell activities, multi-compartment systems are important in regulating complex biological processes with controlled timing and at desired locations.[2] Models to emulate protocell functions with a single compartment can be categorized into two types: membrane-bounded[3-6] and membrane-free[7-9] constructs. In nature, eukaryotes[10] and prokaryotes,[11-13] a variety of membrane-bounded and membrane-free microcompartments are known.

Recently, several studies[14-17] describe synthetic membrane-bounded multi-compartment systems capable of performing inter-compartment enzymatic cascade reactions. These artificial microcompartments have great potentials as novel micro-reactors that package biomaterials for therapeutic applications[18] as well as perform multi-step enzymatic reactions.[19] Such constructs, however, have limitations in spatiotemporal control of reactions due to lack of compartment localization and fusion capabilities. The compartment localization, dissociation, and fusion capabilities are the core characteristics of the protocells.

In this work, we describe stable membrane-free multi-compartmentalization through a hybrid platform of ATP-PDDA complex coacervation and DEX-PEG aqueous two-phase system (ATPS). While DEX-PEG ATPS[20, 21] and ATP-PDDA complex coacervation[22, 23] have each been separately demonstrated as single-compartment protocell models, a system that combines the two types of system into one has not been utilized. Importantly, the resulting aqueous three phase system can be reduced to a two phase system of DEX-PEG, by addition of salt, or of coacervate-PEG by addition of dextranase triggering different reactions to occur across compartments.

First we evaluate the structural stability and molecular retention of the ATP-PDDA coacervates in PEG-DEX system and ionic strength-mediated release of coacervate-encapsulated substances into the DEX phase. Next we perform a two-enzyme cascade reaction that occurs with substrate transport across compartments. Spatiotemporal control could also be performed where reactions are triggered by coacervate coalescence. Another way reactions can be triggered is to disintegrate compartmentalization by enzymatically degrading DEX. This is, to our knowledge, the first demonstration of membrane-free multi-compartmentalization. Our robust membrane-free system recapitulates multi-compartmentalization and provides a unique reactor platform to explore spatiotemporal enzymatic reactions.

6.2 Materials and Methods

Dextran (Mw 500000), polyethylene glycol (Mw 35000), horse radish peroxidase (150 units/mg), GOx (15 units/mg), dextranase (10 units/mg), fluorescein isothiocyanate, rhodamine B isothiocyanate, Ampliflu Red, 2,2'-azino-bis(3-ethylbenzothiazoline-6-sulfonic acid) diammonium salt, 3,3'-diaminobenzidine, MES, MOPS, NaOH, Pur-A-Lyzer Maxi dialysis kit (Mwco 12000) were from Sigma-Aldrich. FITC-DEX (Mw 500000) was from TdB Consultancy AB. Food colorings (blue, green, red, and yellow) were from ESCO Foods. 35 mm plastic dishes with glass bottoms (No.0) were from MatTek Corp. 24-wll plates with flat bottom were from Corning.

6.2.1 Preparation of ATP-PDDA coacervate and DEX-PEG ATPS

ATP (20 mM, pH 6, MES), PDDA (20 mM, pH 6, MES), and loading materials were mixed and centrifuged at 5,000 rpm for 5 min. The supernatant was removed, and the remaining coacervate-rich phase was kept at 4 °C and used within 1 day after preparation. Fixed formulation of an ATPS was used: DEX (10 w/w%, 500 kDa) and PEG (10 w/w%, 35 kDa).

6.2.2 Printing and degrading of ATP-PDDA coacervates in DEX-PEG ATPS

1 μL of food coloring (red, yellow, green, and blue) was premixed in the preparation of coacervates. 50 μL of DEX solution (10 w/w%, pH 6, MES) was placed on a plastic 24-well plate (Corning Coaster) and 0.5 μL of the coacervate-rich phase was dispensed into the DEX droplet. 500 μL of PEG solution (10 w/w%, pH 6, MES) or PEG-NaCl solution (10 w/w%, 250 mM NaCl, pH 6, MES) was added to the DEX solution for retention and release of the food colorings, respectively. Time-lapse images were collected with a stereoscope (C-DSD115, Nikon) at t = 0, 24, and 72 hrs for the retention measurement and at t = 0 - 35 min (every minute) and at t = 1200 min for the release measurement.

6.2.3 Confocal imaging of ATP-PDDA coacervates in DEX-PEG ATPS

Rhodamine B at a final concentration of 1 μM was premixed during the preparation of coacervates. 50 μL DEX droplet (10 w/w%, MES, pH 6) containing 1 mg/ml FITC-DEX was placed in a glass-bottom dish (MatTek) and 0.5 μL of the coacervates was dropped off into the DEX droplet. 500 μL of PEG solution was added to the dish right before the imaging. Fluorescent Z-stack images were taken (Nikon-A1, Nikon) and processed by ImageJ (NIH).

6.2.4 Two-enzyme cascade reaction using ATPS-Complex Coacervate system

HRP (final concentration 0.1 mg/ml, pH 6, MES) and ABTS (final concentration 1 mg/ml, pH 6, MES), DAB (final concentration 1 mg/ml, DMSO), oPD (final concentration 1mg/ml, DMSO) or Ampliflu Red (final concentration 1 mg/ml, DMSO) were premixed in the preparation of the coacervates, respectively. DEX solution (10 w/w%, pH 6, MES) containing GOx (final concentration 0.1 mg/ml, pH 6, MES) was placed on a 24-well plate and 0.5 μL of the coacervates were dispensed into the DEX solution. 500 μL of PEG solution (10 w/w%, pH 6, MES) was added to the DEX solution. Glucose (final concentration 1 mM, pH 6, MES) was added to the PEG solution followed by imaging with a stereoscope or epifluorescent microscope (TE-300, Nikon).

6.2.5 Spontaneous GOx partitioning in the ATP-PDDA coacervate

0.5 μL of the blank coacervate or FITC-GOx-laden coacervate (final concentration 0.1 mg/ml) was dispensed in 10 μL of DEX solution containing FITC-GOx (final concentration 1 mg/ml) or DEX solution, respectively, and submerged in 500 μL of PEG solution. Brightfield and fluorescent images were collected at t = 0 and 24 hrs.

6.2.6 Degradation of DEX phase by compartmentalized or redistributed dextranase

Dextranase (final concentration 0.1 mg/ml, pH 6, MES) was premixed in the preparation of coacervates. 10 µL of 10% (w/w) DEX solution containing 1 µg/ml FITC-DEX was added to each well in a 24-well plate. 0.5 µL of pure ATP-PDDA coacervates and dextranase-laden coacervates were dispensed into the dextran droplet, respectively. 500 µL of 10% (w/w) PEG solution (either dissolved in MES or MES with 165 mM NaCl) was added to each well. Time-lapse images were taken by the epifluorescent microscope and the surface areas of DEX phase were analyzed by ImageJ. The area values were averaged with three replicates and expressed as mean with standard deviation.

6.2.7 Dextranase activity assay in the crowding microenvironment

Bulk dextranase activity was measured using the previously reported protocol[24] : MES buffer (pH 6) at 25 °C in the presence of 0 mM and 165 mM NaCl.

The bulk activity was also obtained using a conventional method[25] and compared in the presence/absence of 10 v/v% PEG.

6.2.8 Characterization of ATP-PDDA coacervates

Zeta potential measurements (ZetaSizer Nano ZSP, Malvern) were conducted on bulk solutions of HRP, GOx, Dextranase, RITC-HRP, FITC-GOx, and RITC- Dextranase at a final concentration of 0.1 mg/ml, respectively. For coacervate resuspension, 0.15 µL of the pure ATP-PDDA coacervates or the enzyme-laden coacervates was resuspended in 1 mL MES buffer solutions (pH 6).

6.2.9 pH and ionic strength influence on ATP-PDDA coacervates in DEX-PEG ATPS

50 μL of DEX solution (10 w/w%, pH 7, DI-water) was placed in each well within a plastic 24-well plate and 0.5 μL of the coacervates was dispensed into the DEX droplet. 500 μL of PEG solution (10 w/w%, pH 7, DI-water) or PEG-NaCl solution (10 w/w%, 250 mM NaCl, pH 7, DI-water) was added to the DEX solution for pH and ionic strength, respectively. 50 μL of 1M HCl was added to the PEG solution (final pH 1).

6.2.10 Enzyme modifications and partition coefficient determination

FITC-GOx and RITC-HRP and RITC-dextranase were modified using an extant protocol.[26] Briefly, enzyme solutions (3 mL, 4 mg/ml, 100 mM Na_2CO_3, pH 8) mixed with 60 μL of a 2 mg/ml solution of FITC or RITC in DMSO were incubated overnight at 4 °C. The resulting FITC-GOx, RITC-HRP, and RITC-dextranase were dialysed against 3 L of Na_2CO_3 (10 mM, pH 8).

Partition coefficient was determined by UV-Vis spectroscopy measurement (Shimazu). Detailed procedure was reported elsewhere.[23] Briefly, UV-Vis spectra of 10 mM PDDA solutions containing RITC-HRP, FITC-GOx, and RITC-Dextranase at a final concentration of 0.1 mg/ml were collected. 10 mM ATP-PDDA solutions containing each enzyme at a final concentration of 0.1 mg/ml were centrifuged and UV-Vis spectra of each supernatant were collected. Based on extinction coefficient of FITC and RITC, the total mass of RITC-HRP, FITC, GOx, and RITC-Dextranase in stock solution and supernatant was calculated from the spectra. The partition coefficient, *K*, is given by Equation 1:

$$K_{coacervate/supernatant} = C_c/C_s \qquad \ldots(1)$$

Where C_c and C_s are the concentration of solute in coacervate-phase and supernatant-phase, respectively. Conservation of mass applies to Equation 2:

$$C_0V_0 = C_cV_c + C_sV_s \qquad \ldots(2)$$

The initial concentration: C_0 and volume: V_0 are known. The coacervate-phase volume: V_c the supernatant-phase volume: V_s are approximately 0.5 (v/v)% and 99.5 (v/v)% of V_0, respectively, in a 10 mM ATP-PDDA system. Since C_s can be obtained by the UV/Vis absorbance spectra, $K_{c/s}$ can be determined accordingly.

6.3 Results and Discussion

6.3.1 Characterization of ATP-PDDA complex coacervates

We used ATP-PDDA complex coacervates at a final concentration of 10 mM in this work. We confirmed that ATP^{4-} : $PDDA^{+}$ ratio was 1 : 4.2 based on UV-Vis spectroscopy measurement (Figure 6.6) and the surface charge potential was +17 mV based on zeta potential measurements (Table 6.1). The data were consistent with previously published values.[23] The ATP-PDDA coacervates isolated in resuspension showed more resistance to wetting a substrate compared to the ATP-PDDA bulk phase (Figure 6.7), as previously reported.[27] We assume that the resuspending process washes out dissolved salts or impurities and increased interfacial stability of the coacervate. Since the partitioning of DEX and PEG within an ATPS is based upon the relative affinity of these compounds for water[28]; we assumed that ATP-PDDA coacervates, when re-suspended within an ATPS, can co-exist in either phase without dissolving into either. We assume that the resuspending process may alter the phase diagram of ATP-PDDA coacervates and facilitate phase separation against the water-based solutions.

6.3.2 Patterning of ATP-PDDA coacervates in DEX-PEG ATPS

Single ATP-PDDA coacervate droplets loaded with rhodamine-B were dispensed by manual pipetting into a 10% DEX – 10% PEG system. ATP-PDDA, DEX, and PEG phases showed distinct boundaries (Figure 6.1A-B). To demonstrate multi-compartmentalization utilizing multiple ATP-PDDA coacervates in the DEX-PEG system, we prepared ATP-PDDA coacervates containing different food colorings and performed multi-printing of the individual coacervate droplets into the PEG-DEX system. We note that food coloring are composed of a combination of dyes such as brilliant blue, allura red, tartazine and each food coloring shows different partitioning behavior. Since these dyes didn't ostensibly diffuse out, we used them as a visual proxy to locate ATP-PDDA coacervates (Figure 1C). The ATP-PDDA coacervates retained their shape without mixing and sequestered the food colorings in the DEX – PEG system for at least 48 hours (Figure 6.8A-C).

6.3.3 Ionic strength-driven degradation of ATP-PDDA coacervates in PEG-DEX ATPS

Complex coacervation is a charge-dependent phenomenon and is consequently susceptible to changes in pH and ionic strength. In contrast, DEX-PEG ATPS is hydrophobicity-based and more resistant to such changes (Figure 6.9). We exploited this property and increased ionic strength to redistribute encapsulated substances upon coacervate degradation while maintaining the DEX-PEG boundary. After addition of a PEG-NaCl solution, the ATP-PDDA coacervates gradually expanded over a 5 min period (Figure 6.2A-B) and completely dissociated in 15 min (Figure 6.2C). The food colorings were completely mixed while the DEX phase in the PEG-NaCl phase remained intact for at least 1200 min (Figure 6.2D). The results reveal that compartmentalized substances in the ATP-PDDA coacervates can be released at physiological ionic strengths. The ionic strength-driven redistribution of compartmentalized biomolecules is a more mild and versatile approach compared to pH change.

6.3.4 Two-enzyme cascade reaction in ATP-PDDA – DEX – PEG system

ATP-PDDA – DEX – PEG system is a membrane-free platform where small molecules like nutrients can diffuse across the boundaries while macromolecules can be spatially sequestered. To articulate this advantage, we demonstrated a cascade reaction commonly adopted in protocell studies.[29] ATP-PDDA coacervate droplets containing amplex red with or without (+/-) HRP was dispensed into a DEX phase +/- GOx overlaid by a PEG phase +/- β-glucose. Fluorescent signal from the ATP-PDDA coacervate was confirmed only when all essential components for the reaction were present in the system (Figure 6.3A-D). We infer that glucose added in the PEG phase diffuses into the DEX phase, where encapsulated GOx was able to catalyze its oxidation, yielding hydrogen peroxide. This hydrogen peroxide then diffuses into the ATP-PDDA coacervate phase where it initiates the HRP-catalyzed oxidation of compartmentalized amplex red – yielding a fluorescent signal.

6.3.5 Compartmentalization of GOx in ATP-PDDA – DEX – PEG system

Since the relative partition coefficients and mobility of these products (glucose and hydrogen peroxide) across the coacervate-DEX-PEG phases are practically difficult to measure, we prepared FITC-GOx and RITC-HRP and observed fluorescent signal localization in the system (Figure 6.10). FITC-GOx homogeneously distributed at the beginning while the dispensed coacervate droplet immediately attracted FITC-GOx at the droplet interface at t = 0 and encapsulated most of FITC-GOx in the droplet interior at t = 24 hrs (Figure 6.10A-C and E-G). Meanwhile FITC-GOx pre-loaded in the coaervate droplet remained compartmentalized at t = 24 hrs (Figure 6.10D and H). We observed no cascade signal if GOx were pre-encapsulated in a coacervate droplet separate from the HRP and substrate, indicating strong molecular partitioning of the coacervate and requirement for proximity between enzymes and substrates. These data are supported by the partition coefficients in the coacervate-rich phase over the coacervate-deficient phase (Table 6.1). The zeta-potential data also indicate that GOx and HRP in suspension is negatively charged, which can assist in its encapsulation within the coacervate phase without diffusing out to other phases. These results provide strong evidence that our system spatially compartmentalizes the enzymes while it allows nutrient diffusion across compartment boundaries.

6.3.6 Spatiotemporal enzymatic cascade reactions using ATP-PDDA – DEX – PEG system

Multi-compartmentalization can also perform multiple reactions in defined spatial locations. In a static system, where movement of reactants is dependent upon diffusion, such compartmentalization also provides a considerable degree of temporal control. To demonstrate this, we prepared three different substrates of HRP (ABTS, DAB, and oPD) as well as controls and performed the same cascade reaction in our system. In the presence of glucose, colorimetric signals were observed while, in the absence of glucose, no such signal was detected (Figure 6.4A and B). No visible change was detected on the control coacervates. Interestingly, when we isolated HRP and DAB individually, no colorimetric change was observed after an hour of incubation (Figure 6.4C and D). In order to activate HRP substrates, HRP and its substrates should be in close proximity due to radical formation. In contrast, when we manually overlaid the droplets, the droplets spontaneously coalesced and turned red, indicating the reaction completion in the coalesced droplet (Figure 6.4D). These results were also reproduced using HRP and ABTS (data not shown). The spatial control of components is necessary for membrane-bound constructs to perform enzyme-mediated cascade reactions.[29, 30] The results illustrate that our system allows flexible spatial manipulation of the coacervates and initiate enzymatic reactions by coacervate coalescence at the desired time point.

6.3.7 DEX degradation assay by compartmentalized or released dextranase

Finally, to assess the compartmentalization influence on enzymatic performance, we prepared RITC-labeled dextranase and compared time-lapse DEX degradation when dextranase sequestered in ATP-PDDA coacervates was either retained or released. Note that we measured dextranase activity using the reported method[24] and confirmed in advance that the dextranase activity remained same regardless of ionic strength change ($K_m = 2 \times 10^{-5}$ M). RITC-dextranase confined in the ATP-PDDA coacervate showed faster degradation (Figure 6.5A, D, and G) compared with released RITC-dextranase (Figure 6.5B, E, and G). Negligible DEX degradation was observed in the absence of dextranase (Figure 6.5C, F, and G). Additionally, we note that the coacervate size was almost constant in the absence of the salts over 24 hours and the DEX degradation was repeatable when new DEX molecules were supplied after complete degradation. We suggest that dextranase confined in the ATP-PDDA coacervate continuously came to in contact with DEX molecules during degradation assay and could constantly degrade DEX. In contrast, dextranase released from the ATP-PDDA coacervate diffused into DEX and PEG phase and had less chance to meet DEX molecules, resulting in slower degradation. The DEX degradation showed different behavior depending on the distribution and location of dextranase. Our data illustrate distinct spatiotemporal dextranase-mediated DEX degradation through multi-compartmentalization.

6.4 Conclusions

We create and validate stable membrane-free multi-compartments by combining ATP-PDDA coacervation and DEX-PEG ATPS. The ATP-PDDA coacervates resuspended in the DEX-PEG system can either coexist or degrade depending on the ionic strength. The multiple ATP-PDDA coacervates can retain compartmentalized substances in DEX-PEG system and release the contents upon degradation. Moreover, the ATP-PDDA coacervates can process spatiotemporal cascade reactions through membrane-free boundaries and initiate the reactions by coacervate coalescence. Finally, the compartmentalization of dextranase isolated from the crowding microenvironment allows stable DEX-degradation process. These characteristics, similar to the living cell system, provide a unique platform that can potentially perform multi-step bioreactions within a single vessel that currently require multiple reaction vessels. Since our system should be open to other complex coacervation and ATPSs, the formulation of the system is tunable. For example, one can use poly(acrilic acid) – PDDA system with negatively charged surfaces[31] together with ATP-PDDA system with positively charged surfaces in other ATPSs in order to tailor the desired molecular partitioning for the specific reactions. Moreover, our system can be miniaturized by ATPS-related microtechniques such as micropattering[32] and droplet microfluidics[33]. Micropatterning of coacervates composed of heterogeneous species in various ATPSs can expand to multi-compartmentalized reactors for various spatiotemporal reactions.

Table 6.1. Zeta-potential and partition coefficient values

Sample	Zeta-potential (mv)	Partition coefficient (coacervate / supernatant)
ATP/PDDA	17.3	
HRP	-7.7	
GOx	-4.6	
Dextranase	-6.1	
RITC-HRP	-1.7	4.5×10^3
FITC-GOx	-1.5	1.3×10^2
RITC-Dextranase	-1.6	2.6×10^2

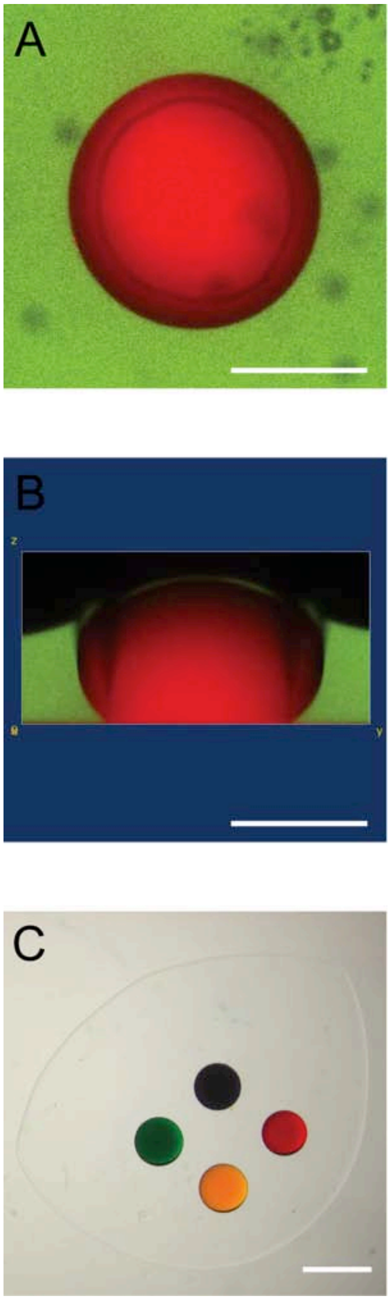

Figure 6.1. Pattering of ATP-PDDA coacervates in a 10% DEX – 10% PEG system. A) transverse cross-section image and B) reconstructed 3D image of a rhodamine B-laden ATP-PDDA droplet (red) resuspended in a DEX droplet (green) in PEG phase. Red: rhodamine B and green: FITC-DEX. C) optical image of ATP-PDDA coacervates encapsulating food colorings (blue, red, yellow, and green). Scale bar (A-B) 500 µm and (C) 1 mm.

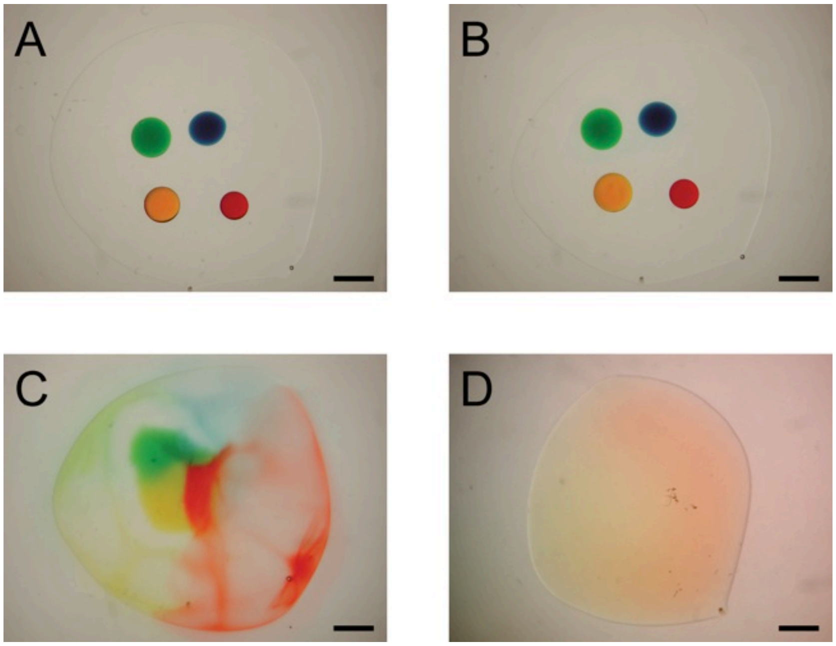

Figure 6.2. Ionic strength-driven degradation of ATP-PDDA coacervates encapsulating food colorings in a DEX – PEG system. Time-lapse images of the ATP-PDDA coacervates in DEX-PEG-NaCl phase at A) t = 0 min, B) 5 min, C) 15 min, and D) 1200 min. Scale bar 1 mm.

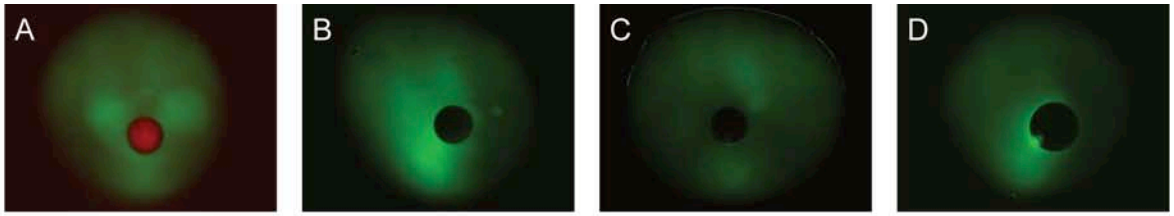

Gluc	+	-	+	+
GOx	+	+	-	+
HRP	+	+	+	-

Figure 6.3. GOx-HRP-mediated cascade reaction occurring across ATP-PDDA, DEX, and PEG phases. A) β-glucose, GOx, and HRP present, B) GOx and HRP present, C) β-glucose and HRP present, and D) β-glucose and GOx present. Green: FITC-DEX, Red: catalyzed product. Scale bar 1 mm.

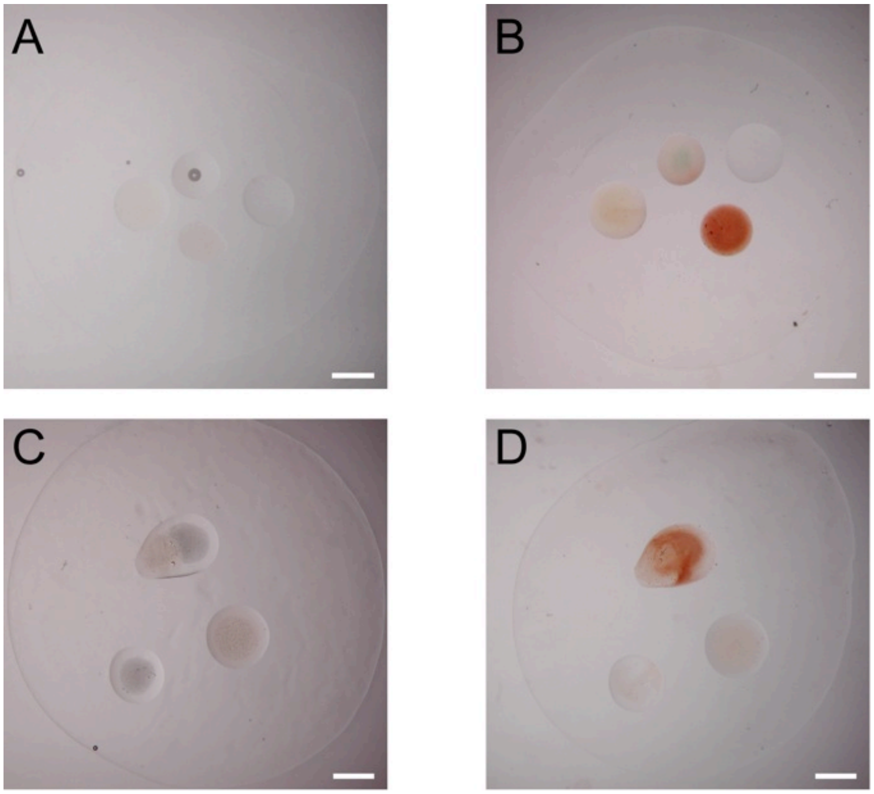

Figure 6.4. GOx-HRP-mediated cascade reaction upon isolation and coalescence of coacervates. GOx-suspended DEX phase was submerged by the PEG phase. HRP-ABTS-laden coacervate (top), blank coacervate (right), HRP-DAB-laden coacervate (bottom), and HRP-oPD-laden coacervate (left) were dispensed A) in the presence and B) in the absence of β-glucose at t = 1 hr. DAB-laden coacervate and HRP-laden coacervate were either isolated (bottom) or merged (top) in the presence of β-glucose in the PEG phase and incubated at (C) t = 0 and (D) t = 1 hr. Scale bar 1 mm.

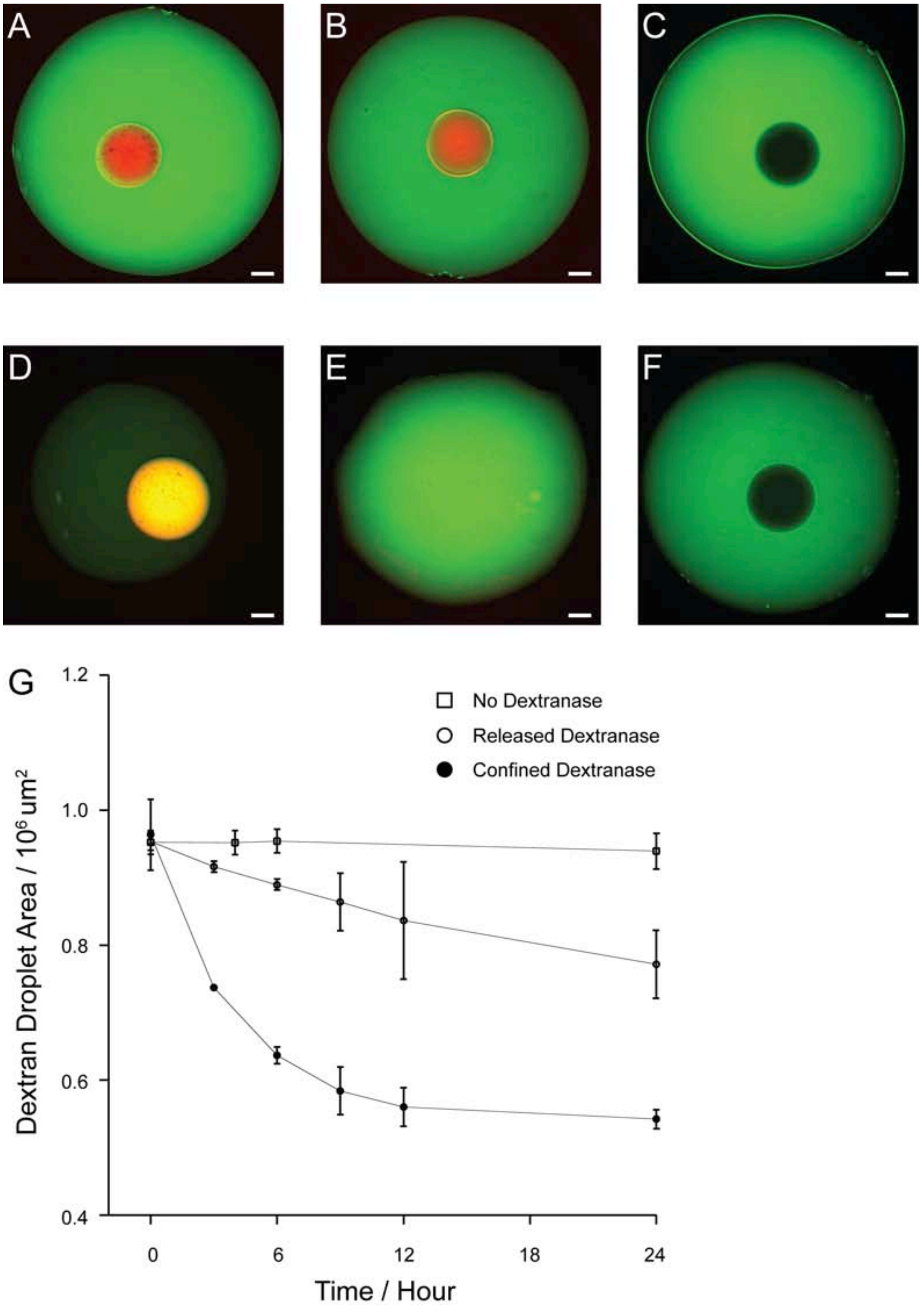

Figure 6.5. Dextranase-mediated DEX degradation assay. Dextranase compartmentalized in the ATP-PDDA coacervate in the DEX-PEG system was either retained (A) t = 0 and D) t = 24 hrs) or released (B) t = 0 and E) t = 24 hrs). The ATP-PDDA in the absence of dextranase was incubated (C) t = 0 and F) t = 24hrs). G) The area of DEX phase was analyzed over 24 hrs. Green: FITC-DEX and red: RITC-dextranase. Scale bar 100 µm.

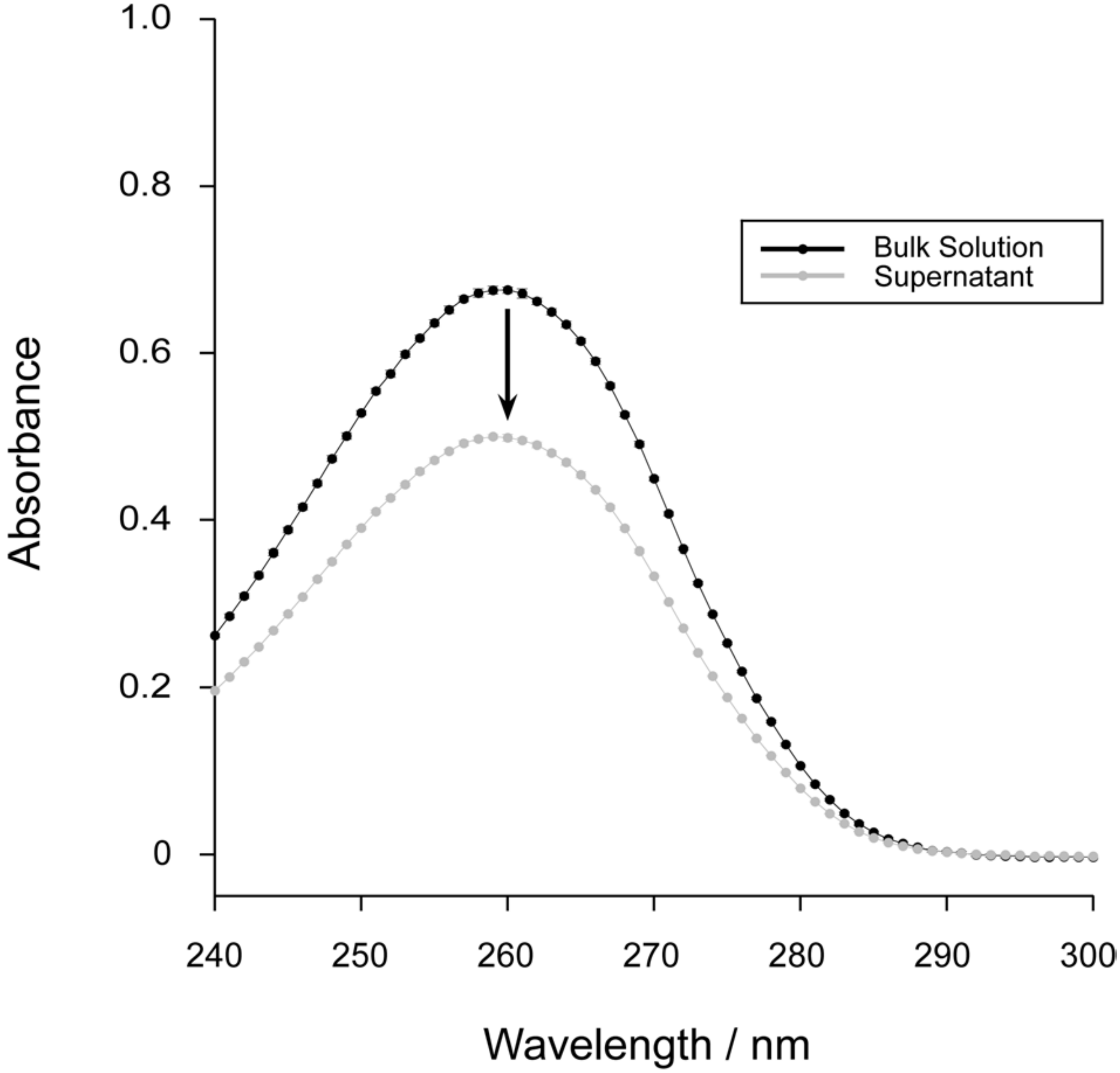

Figure 6.6. UV/VIS spectra of ATP-PDDA coacervate suspension before and after spin down.

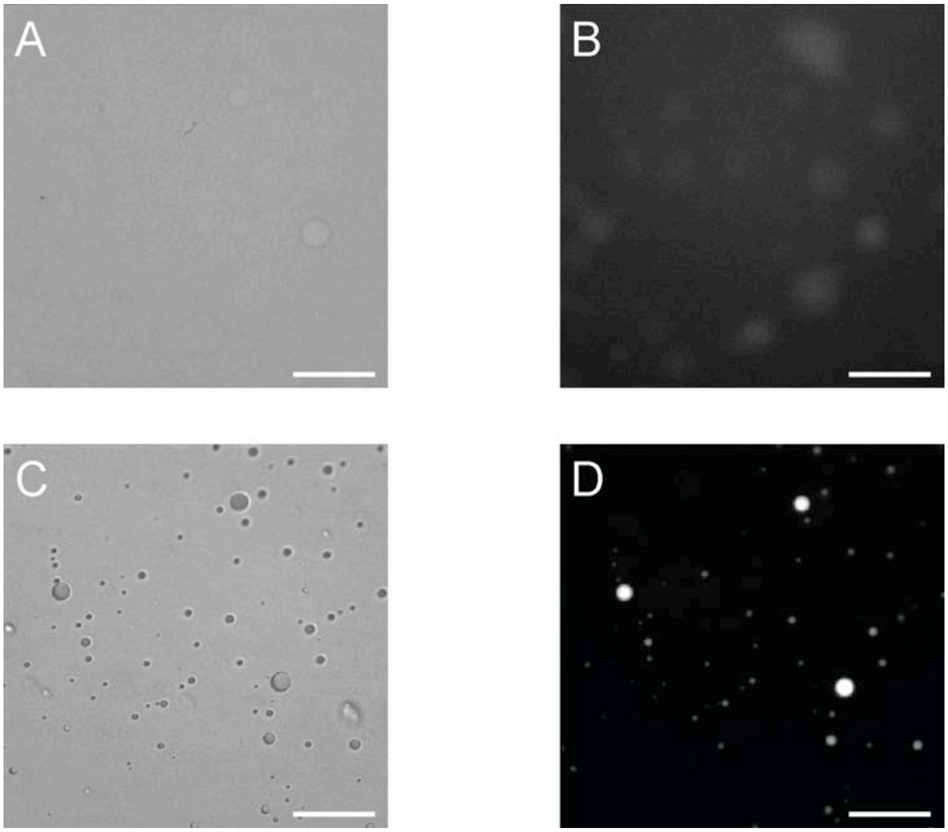

Figure 6.7. Wetting behavior of ATP-PDDA coacervates prepared with 1mM FITC. (A) brightfield and (B) fluorescent images of ATP-PDDA coacervate suspension on a glass slide. (C) brightfield and (D) fluorescent images of ATP-PDDA resuspension on a glass slide. Scale bar 50 μm.

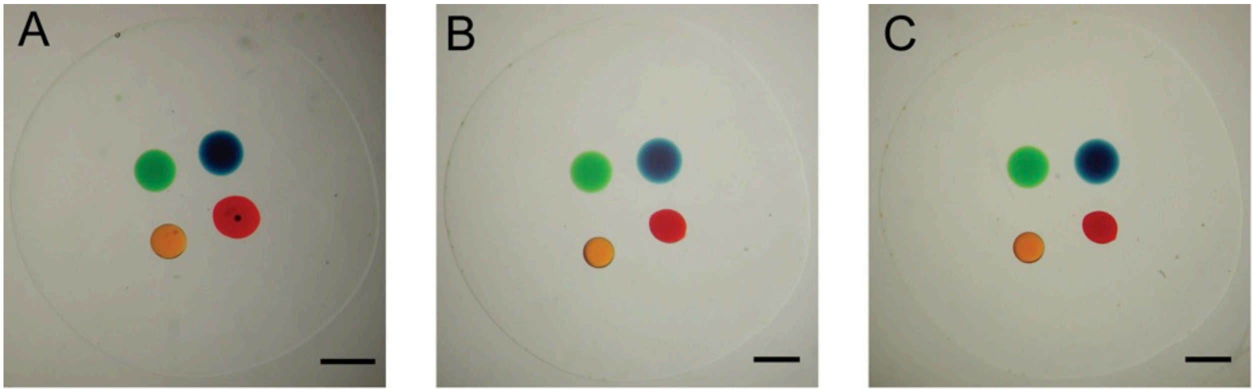

Figure 6.8. Patterning of multiple ATP-PDDA coacervates containing food colorings in a DEX-PEG system. Time-lapse images of the ATP-PDDA coacervates at A) t = 0, B) 24 hrs, and C) 48 hrs. Scale bar 1 mm.

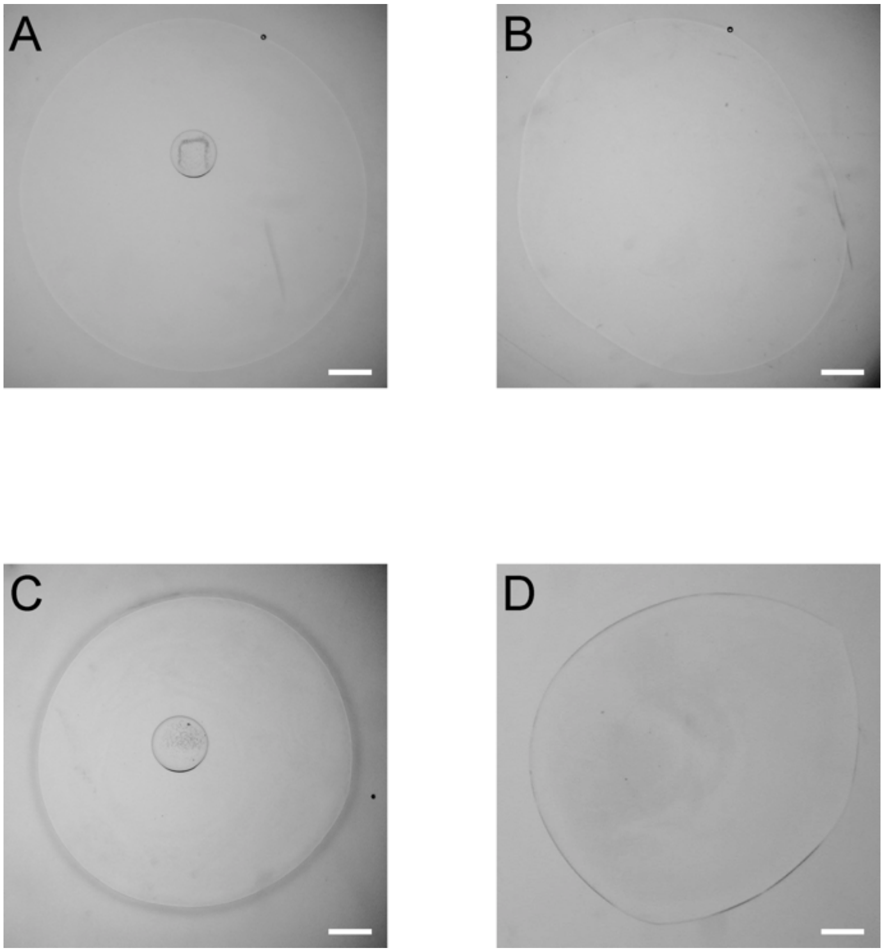

Figure 6.9. pH and ionic strength sensitivity of ATP-PDDA coacervates in DEX-PEG ATPS. Single ATP-PDDA coacervate in a 10% DEX - 10% PEG system at (A) pH 7 and (B) pH 1, and PEG-250 mM NaCl addition at (C) t = 0 and (D) t = 10 min. Scale bar 1 mm.

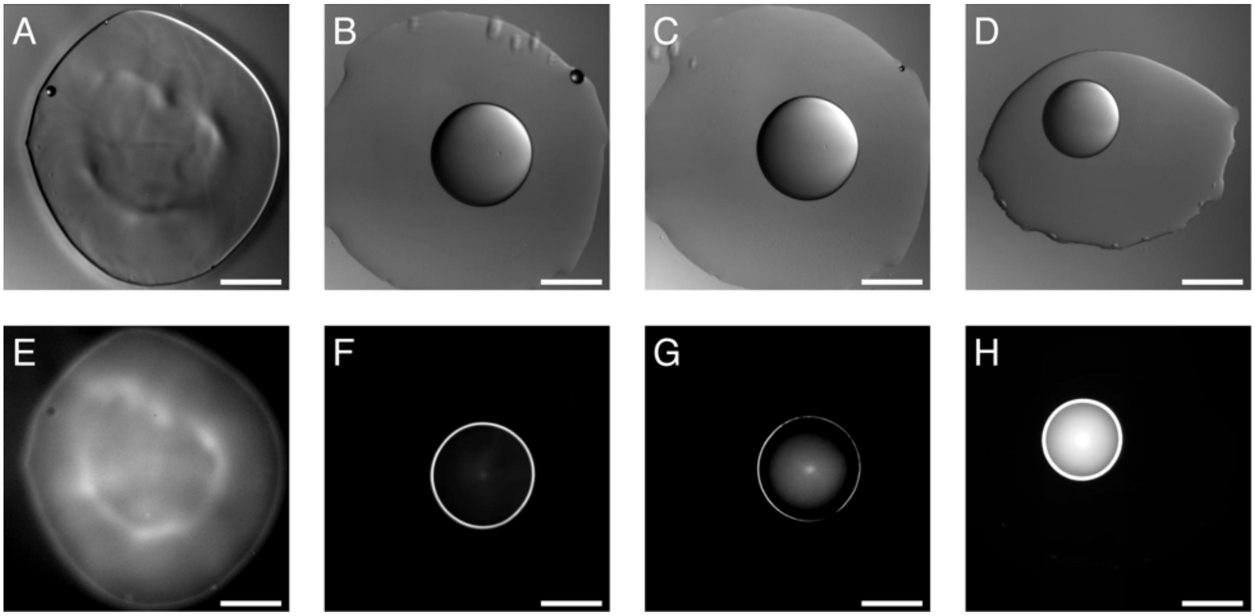

Figure 6.10. Time-lapse GOx partitioning into ATP-PDDA coacervates. Brightfield images of FITC-GOx dispensed in the DEX phase (A) in the absence of the coacervate at t = 0 and in the presence of the coacervate at (B) t = 0 and (C) t = 24 hrs. (D) FITC-GOx pre-loaded in the coacervate at t = 24 hrs. (E-H) fluorescent images of (A-D). Scale bar 500 μm.

6.5 References

1. Oparin, A. I.; Morgulis, S., *The Origin of Life*. 2nd ed.; Dover Publications Inc.: 2003.

2. Monnard, P.-A.; Walde, P., Current Ideas about Prebiological Compartmentalization. *Life* **2015,** *5*, 1239-1263.

3. Walde, P.; Ichikawa, S., Enzymes Inside Lipid Vesicles: Preparation, Reactivity and Applications. *Biomol. Eng* **2001,** *18*, 143-177.

4. Kurihara, K.; Okura, Y.; Matsuo, M.; Toyota, T.; Suzuki, K.; Sugawara, T., A Recursive Vesicle-Based Model Protocell with A Primitive Model Cell Cycle. *Nat. Commun.* **2015,** *6*, 8352-1-7.

5. Kurihara, K.; Tamura, M.; Shohda, K.-i.; Toyota, T.; Suzuki, K.; Sugawara, T., Self-Reproduction of Supramolecular Giant Vesicles Combined with The Amplification of Encapsulated DNA. *Nat. Chem.* **2011,** *3*, 775-781.

6. Hanczyc, M. M.; Fujikawa, S. M.; Szostak, J. W., Experimental Models of Primitive Cellular Compartments: Encapsulation, Growth, and Division. *Science* **2003,** *302*, 618-622.

7. Ichihashi, N.; Usui, K.; Kazuta, Y.; Sunami, T.; Matsuura, T.; Yomo, T., Darwinian Evolution in A Translation-Coupled RNA Replication System within A Cell-Like Compartment. *Nat. Commun.* **2013,** *4*, 2494-1-7.

8. Aumiller Jr, W. M.; Davis, B. W.; Keating, C. D., Phase Separation As A possible Means of Nuclear Compartmentalization. *Int. Rev. Cell Mol. Biol.* **2013**, 109-149.

9. Li, Z.; Zhang, Y.; Su, Y.; Ouyang, P.; Ge, J.; Liu, Z., Spatial Co-Localization of Multi-Enzymes by Inorganic Nanocrystal–Protein Complexes. *Chem. Commun.* **2014,** *50*, 12465-12468.

10. Evreinova, T.; Karnaukhov, W.; Mamontova, T.; Ivanizki, G., The Interaction of Biological Macromolecules in Coacervate Systems. *J. Colloid Interface Sci.* **1971,** *36*, 18-23.

11. Kerfeld, C. A.; Sawaya, M. R.; Tanaka, S.; Nguyen, C. V.; Phillips, M.; Beeby, M.; Yeates, T. O., Protein Structures Forming The Shell of Primitive Bacterial Organelles. *Science* **2005,** *309*, 936-938.

12. Chen, A. H.; Silver, P. A., Designing Biological Compartmentalization. *Trends Cell Biol.* **2012,** *22*, 662-670.

13. Brangwynne, C. P., Phase Transitions and Size Scaling of Membrane-Less Organelles. *J. Cell Biol.* **2013,** *203*, 875-881.

14. Peters, R. J.; Marguet, M.; Marais, S.; Fraaije, M. W.; van Hest, J.; Lecommandoux, S., Cascade Reactions in Multicompartmentalized Polymersomes. *Angew. Chem.* **2014,** *126*, 150-154.

15. Paleos, C. M.; Tsiourvas, D.; Sideratou, Z., Preparation of Multicompartment Lipid-Based Systems Based on Vesicle Interactions. *Langmuir* **2011,** *28*, 2337-2346.

16. Marguet, M.; Bonduelle, C.; Lecommandoux, S., Multicompartmentalized Polymeric Systems: Towards Biomimetic Cellular Structure and Function. *Chem. Soc. Rev.* **2013,** *42*, 512-529.

17. Elani, Y.; Law, R. V.; Ces, O., Vesicle-Based Artificial Cells as Chemical Microreactors with Spatially Segregated Reaction Pathways. *Nat. Commun.* **2014,** *5*, 5305-1-5.

18. Chang, T. M. S., Therapeutic Applications of Polymeric Artificial Cells. *Nat. Rev. Drug Discov.* **2005,** *4*, 221-235.

19. Zhang, Y.; Ruder, W. C.; LeDuc, P. R., Artificial Cells: Building Bioinspired Systems Using Small-Scale Biology. *Trends Biotechnol.* **2008,** *26*, 14-20.

20. Keating, C. D., Aqueous Phase Separation as A Possible Route to Compartmentalization of Biological Molecules. *Acc. Chem. Res.* **2012,** *45*, 2114-2124.

21. Cacace, D. N.; Keating, C. D., Biocatalyzed Mineralization in An Aqueous Two-Phase System: Effect of Background Polymers and Enzyme Partitioning. *J. Mater. Chem. B* **2013,** *1*, 1794-1803.

22. Koga, S.; Williams, D. S.; Perriman, A. W.; Mann, S., Peptide–Nucleotide Microdroplets as A Step towards A Membrane-Free Protocell Model. *Nat. Chem.* **2011,** *3*, 720-724.

23. Williams, D. S.; Koga, S.; Hak, C. R. C.; Majrekar, A.; Patil, A. J.; Perriman, A. W.; Mann, S., Polymer/Nucleotide Droplets as Bio-Inspired Functional Micro-Compartments. *Soft Matter* **2012,** *8*, 6004-6014.

24. Lai, D.; Frampton, J. P.; Tsuei, M.; Kao, A.; Takayama, S., Label-Free Direct Visual Analysis of Hydrolytic Enzyme Activity Using Aqueous Two-Phase System Droplet Phase Transitions. *Anal. Chem.* **2014,** *86*, 4052-4057.

25. Miller, G. L., Use of Dinitrosalicylic Acid Reagent for Determination of Reducing Sugar. *Anal. Chem.* **1959,** *31*, 426-428.

26. Williams, D. S.; Patil, A. J.; Mann, S., Spontaneous Structuration in Coacervate ‐ Based Protocells by Polyoxometalate ‐ Mediated Membrane Assembly. *Small* **2014,** *10*, 1830-1840.

27. Armstrong, J. P.; Olof, S. N.; Jakimowicz, M. D.; Hollander, A. P.; Mann, S.; Davis, S. A.; Miles, M. J.; Patil, A. J.; Perriman, A. W., Cell Paintballing Using Optically Targeted Coacervate Microdroplets. *Chem. Sci.* **2015,** *6*, 6106-6111.

28. Albertsson, P.-Å., *Partition of Cell Particles and Macromolecules*. 3rd ed.; Wiley New York etc.: 1986.

29. Huang, X.; Li, M.; Mann, S., Membrane-Mediated Cascade Reactions By Enzyme–Polymer Proteinosomes. *Chem. Commun.* **2014,** *50*, 6278-6280.

30. Vriezema, D. M.; Garcia, P. M.; Sancho Oltra, N.; Hatzakis, N. S.; Kuiper, S. M.; Nolte, R. J.; Rowan, A. E.; van Hest, J., Positional Assembly of Enzymes in Polymersome Nanoreactors for Cascade Reactions. *Angew. Chem.* **2007,** *119*, 7522-7526.

31. Fothergill, J.; Li, M.; Davis, S. A.; Cunningham, J. A.; Mann, S., Nanoparticle-Based Membrane Assembly and Silicification in Coacervate Microdroplets as a Route to Complex Colloidosomes. *Langmuir* **2014,** *30*, 14591-14596.

32. Kojima, T.; Takayama, S., Patchy Surfaces Stabilize Dextran–Polyethylene Glycol Aqueous Two-Phase System Liquid Patterns. *Langmuir* **2013,** *29*, 5508-5514.

33. Teh, S.-Y.; Lin, R.; Hung, L.-H.; Lee, A. P., Droplet Microfluidics. *Lab Chip* **2008,** *8*, 198-220.

Chapter 7

Conclusions and Future Directions

7.1 Conclusions

Development of functional materials and reliable disease diagnostics are both critical for human welfare and rely on chemical and biological reactions. Such reactions need to be controlled in space and time because spatial control determines reaction speed and scale while temporal control regulates the reaction process. Since conventional reaction platforms often fail to possess such spatiotemporal properties, novel platforms are greatly desired. Microreactors, especially when performing multi-step reactions, require only a small quantity of sample and short time of reaction assessment and has great advantages over the larger counterparts when materials and duration of operation are limited. As such, microreactor platforms may be particularly appealing to the pharmaceutical and biomedical industries where the reduction in time and cost for fast evaluation and implementation of new production protocols is beneficial. In this thesis, a series of unique microreactors that enable microcompartmentalization using macromolecules and liquid-liquid interfaces were developed and demonstrated. The microreactors demonstrated based on all-aqueous compartmentalization using liquid-liquid interfaces enable rapid and selective mass exchange and diffusion with small quantity of reagents, provide robust and reliable reaction platforms, and open new doors to explore functional material processes and biological assays that conventional approaches using multiple reaction vessels fail to achieve. In this chapter, conclusions of each chapter topic and future directions are described to aim for further material and biomedical applications.

7.1.1 Micropatterning system: micro-scale DEX-PEG ATPS patterning

Deterministic ATPS patterning on a cell monolayer was previously demonstrated and envisioned for use as a scaffold for ATPSs microreactor arrays on a non-cellular surface. However, the underlying mechanism of generating stable ATPSs patterns on such surface was elusive. We exploited the principle of surface modification at an air-water interface where introduced surface heterogeneity wets the defined surface region and therefore modified PDMS surfaces with various ATPS-related polymers in order to make surface energy gap in a DEX-PEG interface.

The key to successfully patterning DEX-PEG ATPS on the PDMS surfaces was to introduce a sufficient surface energy gap in the defined region. Moreover, arbitrary ATPS patterns were achieved by patchy modification with optimal patch-to-patch distance.

Surface modification has the great potential to confine ATPS solutions containing biologic materials at the desired location and make ATPS microarrays on various surfaces for bioassays. We later find that this system is also applicable to PEG-Salt ATPSs and expect that it would be versatile to other ATPSs based on the universal principle of surface modification.

Since each ATPS has different molecular partitioning ability, future study may involve multiplex micropatterning of ATPSs to confine different biomolecules under the same solution and perform multiplexed reaction assays.

7.1.2 Micropatterning system: micro-scale hydrogel patterning

The manner of chemogradient formation in the microenvironment affects overall cell migration that can lead to tumor growth and metastasis. We took advantage of the surface patterning principles and developed a technique for cell-laden hydrogel micropatterning. A cell-repellent surface was adopted together with micropatterned hydrogels where cells can only move through the gel matrix without attaching the substrate surface. Two hydrogels containing CXCL12-secreting cells and CXCR4-expressing cells, respectively, were micropatterned at the designed distance and overlaid by other hydrogels. Migration of breast cancer cells was observed when an optimal combination of gel type and isoform was utilized at an optimal gel-to-gel distance. The simulation showed that the chemogradients of CXCL12-isoforms spatiotemporally form in the 3D embedded gel matrix under the appropriate condition. Additional work completed by our group using oxygen beads revealed that the micropatterned hydrogels were hypoxic and oxygen gradient also formed within the microenvironment.

Micropatterned hydrogels in this system can serve as a unique bioassay platform to assess migratory behavior among the patterned cell populations. We later confirm that this system also allows angiogenesis of endotherial cells from bone marrow where the distance control between the patterned cell populations is critical. It indicates that this patterning format is beneficial to the biological assays that require delicate spatial controls. Future research may involve multiplexed hydrogel micropatterning for complex chemogradients formation, cell migration and angiogenesis of different endothelial cell populations.

7.1.3 Oil dehydration system: micro-scale ATPS binodal determination

Determination of ATPS binodals requires a large amount of samples that restricts exploration of biological ATPSs. We created a novel system using water-oil interfaces that enables microscale determination of ATPS binodals. A water microdroplet was dehydrated at an FC40 - soybean oil interface. Dilute phase-forming polymers suspended in a droplet were concentrated upon dehydration and phase separated at the binodal point. Based on optical images of the droplet, binodal concentrations were calculated and confirmed to be consistent with the binodals obtained by a conventional method.

A unique shrinking microenvironment can precisely estimate phase diagrams of conventional and biological ATPSs with a small quantity of samples and serve as a useful tool to explore emerging ATPSs composed of biomolecules. We later observed that this system is applicable to DNA-Histone H1 system with microgram quantity, implying the system is compatible with hydrophobicity-based and charge-based ATPSs. Future direction may validate DNA-, RNA-, and protein-based ATPSs using the platform where limited amount of samples are expected.

7.1.4 Oil dehydration system: unique self-assembly of CdTe dendrites

The superstructures of semiconductive nanoparticles with large surface coverage via self-assembly provide a variety of attractive applications such as solar cell materials with highly efficient light-energy conversion. Droplet dehydration was exploited and served as a platform for self-assembly of CdTe nanoparticles. The NPs assembled in the microdroplet evolved to dendric structures as shrinking proceeded while the NPs in other static conditions formed arborized structures. The simulation showed that the shrinking microenvironment created a concentration gradient of the NPs inside the microdroplet that resulted in the unique dendric evolution. The dendric structures showed large surface area and fractal dimension and illustrated distinct chemical and optical properties in contrast to the counterpart.

A droplet dehydration format enables unique evolution of CdTe nanoparticle assembles and sheds light on particle-assembly microenvironment. We believe that this shrinking platform is applicable to other nanoparticles and feasible to construct unique superstructures that conventional bulk conditions fail to produce. The next step is to develop a method to manipulate the intact superstructures in a robust and highthroughput format for their practical use.

7.1.5 Multi-compartmentalization: novel liquid-liquid microcompartments

Living cells are comprised of multiple membrane-bound or membrane-free compartments that enable the isolation and spatiotemporal regulation of biological processes. While some work has been done to study membrane-bound compartments *ex vivo*; surprisingly little has been done to study membrane-free multi-compartmentalization. A combined system of DEX-PEG ATPS and ATP-PDDA complex coacervation was developed to create membrane-free multi-compartments where ATP-PDDA coacervates, DEX phase, and PEG phase serve as analogues of organelles, cytosol, and extracellular environment, respectively. ATP-PDDA coacervates could compartmentalize various molecules and release the substances upon ionic strength change. Multiplex two-enzyme cascade reactions were performed in the system and spatiotemporal reactions were regulated by ATP-PDDA coacervate location and coalescence. DEX degradation assay using dextranase revealed distinct reaction kinetics of compartmentalized dextranase compared dextranase in suspension.

Our system supports the performance and study of complex reaction processes across multiple micro-scale compartments. Adopted ATPSs are hydrophobic-based and charge-based, not limited to DEX-PEG and ATP-PDDA systems, respectively. Based on the type of biomolecules and reaction processes, the formulation of ATPSs can be modified and implemented in the presented format. One potential future study is to express proteins in one compartment, modify the protein in another compartment, and perform subsequent delivery to extra environment by tuning ATPS formulations. Such system resembling the living cell system enables *in situ* production of therapeutic proteins and represents a significant improvement over conventional microreactors.

7.2 Future Directions

Even though the reactors described in this thesis represent unique platforms that are not simply scaled-down from conventional reactors, where reactor sizes are approximately 100 μm – 1 mm and where operation of the micro-reactor requires manual reagent handling, the presented systems can be further improved in both scale and functionality.

7.2.1 Droplet microfluidics as a reaction platform

Droplet microfluidics is a direct and attractive approach to generate robust microreactors. T-junction, flow focusing, and co-flowing geometries in a microfluidic device are commonly adopted to pinch off microdroplets from a fluid stream in an oil-water system. The microdroplets enable rapid and highthroughput bioassays such as single cell analysis, disease detection, and PCR reaction in the individual droplets and process statistically sufficient amount of data in a short time (1000 - 10000 droplets per second).

Moreover, droplet microfluidics has another prominent application: *in situ* microscale hydrogel generation. Briefly, photo-crosslinkable polymer such as PEG-diacrylate is either incorporated in the reagent solution or co-flowed with another polymer solution in a microchannel, and crosslinked by *in situ* UV-exposure. The latter case, known as flow lithography, has been exploited to create complex 3D shape microgels in a highthroughput manner. The generated microgels enable encoding and decoding information in the complex architectures. This platform is particularly useful for fabricating cell culture scaffolds or diagnostic platforms.

7.2.2 Molecular crowding in microenvironments

Molecular crowding is another phenomenon to consider in a microreactor where macromolecules are present. Macromolecules confined in the microenvironment are known to introduce volume exclusion that can significantly alter the reaction kinetics of biological reactions relative to bulk conditions. This phenomenon, named molecular crowding, can be seen in the interiors of living cells where macromolecular species at the total concentration more than 100 mg/mL are packed into tens of micrometer sized compartments occupying 20-30% of the total cell volume. The crowding environment is known to enhance or deteriorate enzymatic activities depending on the concentration and molecular weight of the crowding agents. The ability to interrogate the effect of molecular crowding would be a non-trivial improvement over conventional bulk systems for the modeling of sub-cellular biological reactions *in vitro*.

Microreactor platforms can provide a suitable opportunity to investigate molecular crowding. Macromolecular ATPS and droplet microfluidic platforms, individually or in combination, can be used to create such crowding within a given micro-environment. The biological processes modeled in such a platform would provide novel insights to assess molecular crowding. Our system described herein can be reconstituted in the automated and miniaturized microdroplet system. Potential research direction is to combine those techniques and phenomena to create novel microreactors for pharmaceutical and biomedical applications.